Investigation of the Processing History during Additive Friction Stir Deposition using In-process Monitoring Techniques

David Garcia

Dissertation submitted to the faculty of the Virginia Polytechnic Institute and State University in partial fulfillment of the requirements for the degree of

Doctor of Philosophy
In
Materials Science and Engineering

Hang Z. Yu, Chair
Yunhui Zhu, Co-chair
William T. Reynolds
Carlos T.A. Suchicital

December 10th, 2020
Blacksburg VA

Keywords: metal additive manufacturing, friction stir process, i*n situ* monitoring, thermomechanical processing

An Investigation of the Processing History during Additive Friction Stir Deposition using In-process Monitoring Techniques

David Garcia

ABSTRACT

Additive friction stir deposition (AFSD) is an emerging solid-state metal additive manufacturing technology that uses deformation bonding to create near-net shape 3D components. As a developing technology, a deeper understanding of the processing science is necessary to establish the process-structure relationships and enable improved control of the as-printed microstructure and material properties. AFSD provides a unique opportunity to explore the friction stir fundamentals via direct observation of the material during processing. This work explores the relationship between the processing parameters (e.g., tool rotation rate Ω, tool velocity V, and material feed rate F) and the thermomechanical history of the material by process monitoring of i) the temperature evolution, ii) the force evolution, and iii) the interfacial contact state between the tool and deposited material. Empirical trends are established for the peak temperature with respect to the processing conditions for Cu and Al-Mg-Si, but a key difference is noted in the form of the power law relationship: Ω/V for Cu and Ω^2/V for Al-Mg-Si. Similarly, the normal force F_z for both materials correlates to V and inversely with Ω. For Cu both parameters show comparable influence on the normal force, whereas Ω is more impactful than V for Al-Mg-Si. On the other hand, the torque M_z trends for Al-Mg-Si are consistent with the normal force trends, however for Cu there is no direct correlation between the processing parameters and the torque. These distinct relationships and thermomechanical histories are directly linked to the contact states observed during deformation monitoring of the two material systems. In Cu, the interfacial contact between the material and tool head is characterized by a full slipping condition ($\delta = 1$). In this case, interfacial friction is the dominant heat generation mechanism and compression is the primary deformation mechanism. In Al-Mg-Si, the interfacial contact is characterized by a partial slipping/sticking condition ($0 < \delta < 1$), so both interfacial friction and plastic energy dissipation are important mechanisms for heat generation and material deformation. Finally, an investigation into the contact evolution at different processing parameters shows that the fraction of sticking is critically dependent on the processing parameters which has many implications on the thermomechanical processing history.

An Investigation of the Processing History during Additive Friction Stir Deposition using In-process Monitoring Techniques

David Garcia

GENERAL AUDIENCE ABSTRACT

Additive manufacturing or three-dimensional (3D) printing technologies have been lauded for their ability to fabricate complex geometries and multi-material parts with reduced material waste. Of particular interest is the use of metal additive manufacturing for repair and fabrication of industrial and structural components. This work focuses on characterizing the thermomechanical processing history for a developing technology Additive Friction Stir Deposition (AFSD). AFSD is solid-state additive manufacturing technology that uses frictional heat and mechanical mixing to fabricate 3D metal components. From a fundamental materials science perspective, it is imperative to understand the processing history of a material to be able to predict the performance and properties of a manufactured part. Through the use of infrared imaging, thermocouples, force sensors, and video monitoring this work is able to establish quantitative relationships between the equipment processing parameters and the processing history for Cu and Al. This work shows that there is a fundamental difference in how these two materials are processed during AFSD. In the future, these quantitative relationships can be used to validate modeling efforts and improve manufacturing quality of parts produced via friction stir techniques.

Acknowledgements

I would like to begin by thanking my advisor Dr. Hang Z. Yu who provided invaluable mentorship and technical guidance throughout my academic career. He has always been encouraging and demanding, but always respectful of professional development. I would also like to thank my committee co-chair Dr. Yunhui Zhu for lending her expertise in data analysis and quantification. I truly appreciate the consistent push towards self-improvement. Additionally, I would like to thank my committee members Dr. William T. Reynolds and Dr. Carlos T.A. Suchicital for all of the time, support, and guidance they provided for this work. A special thanks goes to Dr. Zhenyu J. Kong. While not directly related to my thesis work, he provided me with a unique opportunity to apply my skills and knowledge in an interdisciplinary fashion as a co-member of his research group in the department of Industrial and Systems Engineering.

I would also like to thank the members of Dr. Hang Yu's research group who have become more than just colleagues over the past few years. You helped to support my scientific, social, and cultural endeavors in ways I could never have imagined.

Finally, I would like to thank my life-long friends and family for their constant love and support. Especially, my parents who have who have always strived to give me the best life possible.

Attributions

Several colleagues assisted in the data curation and data analysis associated work. These acknowledgements and attributions are detailed below:

Dr. Hang Z. Yu: Professor in the department of Materials Science and Engineering at Virginia Tech (VT). Dr. Yu is the dissertation advisor and committee chair. He is responsible for primary conceptualization of the research goals, providing advice and revisions for the all research content in this work, and resource acquisition.

Dr. Yunhui Zhu: Professor in the Bradley Department of Electrical and Computer Engineering at Virginia Tech (VT). Dr. Zhu is a co-chair for this dissertation and assisted in writing and revisions for the research content of this dissertation.

Dr. Zhenyu J. Kong: Professor in the Grado Department of Industrial and Systems Engineering at Virginia Tech (VT). Dr. Kong assisted in conceptualization of the thermal history study in Chapter 3 and provided equipment for characterization.

Mr. W. Douglas Hartley: A PhD candidate working with Dr. Hang Z. Yu that assisted in thermocouple device set-up, manufacturing equipment operation, and data curation for the thermal history study in Chapter 3 of this work.

Mr. Hunter A. Rauch: A PhD candidate working with Dr. Hang Z. Yu who assisted in data curation and formal analysis for the thermal history study in Chapter 3 of this work.

Mr. R. Joey Griffiths: A PhD candidate working with Dr. Hang Z. Yu that assisted in data curation for the thermal history study in Chapter 3 of this work. He also provided the EBSD imaging in Chapter 4 of this work.

Mr. Rongxuan (Raphael) Wang: A PhD candidate working with Dr. Zhenyu J. Kong and assisted with equipment calibration for the infrared imaging and data curation for the thermal history study in Chapter 3 of this work.

Mr. Greg D. Hahn: A PhD candidate working with Dr. Hang Z. Yu. He assisted in sample preparation for the EBSD imaging in Chapter 4 and in data curation for the contact state study in Chapter 5 of this work.

Table of Contents

List of Figures

List of Tables

Chapter 1

Introduction

1.1 Motivation

Additive manufacturing (AM), sometimes referred to as three-dimensional (3D) printing, free-form fabrication, or rapid prototyping, refers to a class of emerging manufacturing techniques with the ability to perform site-specific deposition or bonding in a layer-by-layer fashion to fabricate bulk parts [1]. The most salient benefits of these additive techniques lie in the ability to create complex geometries [2, 3], multi-material parts [4, 5], or near-net shape parts that reduce material waste [6]. The key tenant of materials science and engineering lies in the understanding the process-structure-property relationship [7] which has yet to be fully understood for these still-developing AM techniques [8]. How a component is manufactured determines the microstructure and morphology of the part, which in turn will determine the final part properties and effectiveness of the component during its service life. AM techniques typically have non-equilibrium processing conditions due to their periodic nature and are especially sensitive to the specific part geometry [9]. Critically, inadequate conditions may lead to delamination between layers, warpage, internal porosity, or high residual stresses. In order to minimize the presence of defects and design the as-manufactured properties of a

component, it is necessary to have a comprehensive understanding of the relationship between equipment processing variables, the materials processing conditions, and the resultant microstructure (i.e. the process-structure-property relationship).

1.2 Research Goals

The goal of this work is to understand the relationship between the equipment processing conditions and the thermomechanical processing history of materials processed by Additive Friction Stir Deposition. Understanding of this relationship will provide key physical insights into the process fundamentals via direct characterization of the thermomechanical processing history. This is achieved by *in situ* monitoring of 1) the thermal history, 2) the force evolution, and 3) the contact state between the tool and deposited material. Monitoring of these three components will enable an understanding of thermomechanical properties of the material under working conditions that ultimately determine the deformation behavior and material flow. In particular, this work compares the behavior of two materials during deposition: Aluminum Alloy 6061 (Al-Mg-Si alloy) and Cu-110 (commercially pure Cu). These materials are of interest because they have distinct thermomechanical properties, unique strain accommodation mechanisms, and they are typically difficult to process using other metal additive manufacturing methods. Furthermore, the knowledge obtained in this work can be directly applied to friction stir welding and processing techniques. Ultimately, the results of this work will enable improvement to welding and additive manufacturing part quality while enabling a deeper understanding of the Friction Stir physical principles.

1.3 Dissertation Organization

Chapter 1 addresses the research goals and motivation of this dissertation. Chapter 2 provides background information on additive manufacturing processes and the fundamental physical principles that govern the AFSD process. Chapter 3 presents a method for *in situ* monitoring of the thermal history of AFSD and applies the technique for a comprehensive analysis of the thermal history characteristics. Chapter 4 investigates the force evolution during AFSD at several equipment processing conditions and provides a brief investigation into the process-structure relationship for Al-Mg-Si. Chapter 5 provides a method for quantifying the contact state at the tool-material interface and explores the influence of different tool geometries on the force evolution during AFSD. Chapter 6 summarizes the major conclusions of this work and provides discussion on future directions.

References

[1] Ngo, T.D., Kashani, A., Imbalzano, G., Nguyen, K.T.Q., Hui, D., Additive manufacturing (3D printing): A review of materials, methods, applications and challenges, Composites Part B: Engineering 143 (2018) 172-196.

[2] Chu, C., Graf, G., Rosen, D.W., Design for Additive Manufacturing of Cellular Structures, Computer-Aided Design and Applications 5(5) (2008) 686-696.

[3] Zheng, X., Smith, W., Jackson, J., Moran, B., Cui, H., Chen, D., Ye, J., Fang, N., Rodriguez, N., Weisgraber, T., Spadaccini, C.M., Multiscale metallic metamaterials, Nature Materials 15(10) (2016) 1100-1106.

[4] Chen, D., Zheng, X., Multi-material Additive Manufacturing of Metamaterials with Giant, Tailorable Negative Poisson's Ratios, Scientific Reports 8(1) (2018) 9139.

[5] Garcia, D., Jones, M.E., Zhu, Y., Yu, H.Z., Mesoscale design of heterogeneous material systems in multi-material additive manufacturing, Journal of Materials Research 33(1) (2018) 58-67.

[6] Huang, S.H., Liu, P., Mokasdar, A., Hou, L., Additive manufacturing and its societal impact: a literature review, The International Journal of Advanced Manufacturing Technology 67(5) (2013) 1191-1203.

[7] Callister, W.D., Rethwisch, D.G., Materials Science and Engineering: An Introduction, Wiley2018.

[8] Tofail, S.A.M., Koumoulos, E.P., Bandyopadhyay, A., Bose, S., O'Donoghue, L., Charitidis, C., Additive manufacturing: scientific and technological challenges, market uptake and opportunities, Materials Today 21(1) (2018) 22-37.

[9] Jia, Q., Gu, D., Selective laser melting additive manufacturing of Inconel 718 superalloy parts: Densification, microstructure and properties, Journal of Alloys and Compounds 585 (2014) 713-721.

Chapter 2

Background

2.1 Additive Manufacturing

Additive manufacturing defines a class of emerging technologies used to fabricate components in a layer-by-layer fashion. This contrasts with traditional fabrication methods that involve casting or subtraction of material through a milling or cutting procedure to achieve the desired geometry. Seven methods of additive manufacturing have been generally defined, with the use of different techniques primarily dependent on the type of material being processed: metal, polymer, or ceramic. A description of each AM technique is provided below, and a summary of the key advantages and disadvantages is shown in Table 2.1 [1, 2]:

Binder Jetting – A liquid binder or adhesive is selectively placed over a thin layer of stationary powder to trace out the desired geometry. Once the geometry for a single layer is complete, a new layer of powder is added and the geometry for the second layer is traced by the adhesive material. This repeats in a layer by layer fashion to create a bulk component [3]. The powder bed provides a support structure for subsequent layers; thus, it is possible to create free-form geometries at will. There are few limitations on material powder, but the final part will generally have poor structural properties [4]. Burn-out of the adhesive

and post-processing to improve properties is often performed as a required step for structural components.

Directed Energy Deposition – A high power laser is used to melt powder or wire feedstock onto the surface of an existing substrate or part [5]. The small spot size of the laser allows for fine control of the geometry tolerance, while the actual deposition process itself remains quick and viable for large scale fabrication. Directed energy deposition is often performed under an inert atmosphere which is the primary limitation for scalability. The local-scale deposition provides opportunities for local variation in composition or microstructure by varying the powder or wire feedstock [6]. However, this process has some limitations with alloy vaporization during processing and high thermal stresses associated with the sharp thermal gradients during melting and solidification [7].

Material Extrusion – Material extrusion or fused deposition modeling (FDM) is the most consumer friendly and commercially available AM technique [8]. Material extrusion involves heating of a thermoplastic filament until it resembles a viscous liquid or a soft amorphous solid. It is pushed through a narrow nozzle onto previously deposited material where it fuses during cooling. Here, the resolution of printing is limited by the size of the nozzle. While extrusion is cheap and has very rapid build rates, it is limited in its applicability due to the limited range of thermoplastics. Additionally, extrusion results in highly anisotropic parts and weak interfaces in the build direction [9].

Material Jetting/Ink jetting – Jetting techniques are similar to extrusion in that material is continuously fed through a narrow nozzle while tracing out a desired geometry. The key difference for jetting processes is that a liquid suspension is used as the medium and they rely on liquid evaporation for setting instead of thermoplastic solidification. These liquid suspensions can carry many types of materials [10, 11], but are limited in their layer-to-layer adhesion. For large volume prints, the ink may begin to set in the nozzle which provides additional challenges in scalability [1].

Powder Bed Fusion – A focused beam of energy (either electron or laser) is directed at a bed of metal or ceramic powder and causes local melting or sintering of material. The beam traces out the desired geometry on the powder bed. Then a second layer of powder is overlaid, and the second layer geometry is carried out. The key limitations of powder bed fusion techniques lie in size of the powder bed and the transient thermodynamics and kinetics during solidification that make microstructure control challenging [12].

Sheet Lamination – There are three types of sheet lamination processes: 1) adhesive bonding, 2) thermal bonding and 3) deformation bonding sheet lamination [13]. Adhesive sheet lamination is similar to binder jetting, but with solid sheet feedstock instead of a powder bed. Thermal bonding can be through melting or diffusion bonding of dissimilar materials which creates a natural gradient of the bonded materials. Deformation bonding such as friction stir additive manufacturing (FSAM) or ultrasonic additive manufacturing (UAM) relies on interface deformation to enable mechanical mixing and

joining. Here, the primary limitation is the need for post-process machining to achieve the desired geometry and the lack of site-specific microstructure control.

Stereolithography – A photocuring resin is selectively exposed to UV light to create the desired net shape in a layer-by-layer fashion. Similar to ink jetting, ceramic particles may be dispersed within the resin to allow fabrication of polymer-ceramic composites [14]. Stereolithography has a very fine resolution and surface finish but is a very slow process. Furthermore, it is very limited in the material diversity and requires post-process cleaning and curing. Ceramic parts often require a burn out phase for the polymer binder and leave behind substantial porosity [2].

Table 2.1: A summary of the advantages and disadvantages for different additive manufacturing methods

Method	Materials	Advantages	Disadvantages
Binder Jetting	• Ceramics • Metals • Polymers • Composites	• Rapid build rates • Low cost • Wide range of materials	• High porosity • Post-processing
Directed Energy Deposition	• Metals • Composites	• Site-specific control of composition and microstructure • High strength parts	• Large thermal gradients • Requires support structures
Extrusion	• Polymers • Composites	• Rapid build rates • Low cost • High scalability	• Anisotropic Properties • Requires support structures • Limited to thermoplastics
Material Jetting	• Metals • Polymers • Composites	• Multi-material parts • High precision • Rapid build rates	• Poor out-of-plane properties • Material workability during large prints
Powder Bed Fusion	• Metals • Ceramics • Composites	• High quality builds • Local microstructure control	• Large thermal gradients • Limited build volume • Requires specific powder properties
Sheet Lamination	• Metals • Polymers • Composites	• Rapid build rates • Low cost	• Limited resolution • Poor out-of-plane properties
Stereolithography	• Ceramics • Polymers • Composites	• Good surface finish • Very fine details	• Slow build rates • Limited material selection

From the list of existing additive manufacturing technologies, those used for metal additive manufacturing of structural components include: directed energy deposition (DED), powder bed fusion (PBF), and sheet lamination. DED and PBF rely on focused energy beams to create local melting and solidification. While these techniques offer a lot of freedom in terms of local composition and microstructure control, the large thermal gradients [15] associated with melting and solidification introduce high residual stresses [16], internal porosity [17], and poor homogeneity of microstructure in bulk parts [12]. UAM and FSAM stand out as the two applicable sheet lamination AM techniques that can produce high strength metal components. The primary limitation of these sheet lamination techniques is in their ability for free-form fabrication and microstructure control. The minimum feature size for sheet lamination processes without any additional subtractive/milling procedures is a direct result of the foil/sheet size. For UAM, the microstructure of the sheets is largely unperturbed [18], so there is no room for in-process control of microstructure. For FSAM there can be large variations in the microstructure from those areas in contact with the tool to those far away that retain the base microstructure [19].

Additive friction stir deposition (AFSD) is a novel additive manufacturing technique with the ability to fabricate metal or composite components [20]. It does not fit directly into any of the existing additive manufacturing categories, rather it lies somewhere between an extrusion process and a sheet lamination process. Notably, AFSD retains the site-specific nature of deposition from the beam-based additive manufacturing technologies, while staying in a solid-state processing regime. In turn, this enables isotropic mechanical properties, site-specific control of microstructure, local variation of composition, and low residual stress. In AFSD a solid rod feedstock is continuously fed through a rotating tool. Thermal softening of the feedstock is achieved by frictional heating between the feed material and the substrate/tool surface. Softening of the feed material and substrate in turn enables co-deformation and mixing to produce a single, bonded part. Figure 2.1 shows an example part fabricated via AFSD. The AFSD process relies on the friction stir principles which have been studied in depth for Friction Stir Welding (FSW) and will be discussed in more detail in Section 1.3.

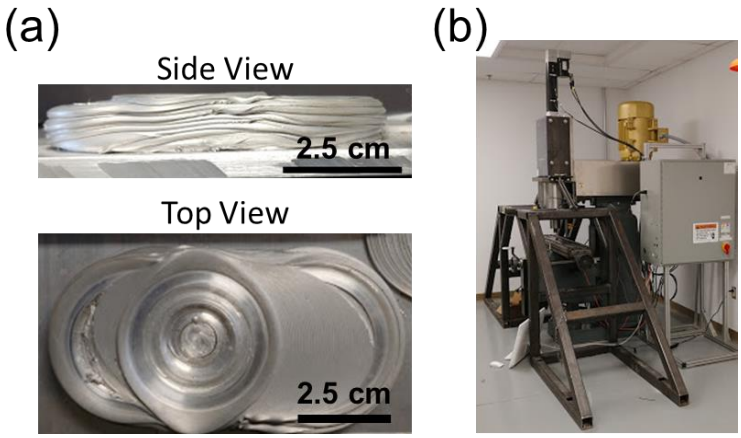

Figure 2.1. A figure showing (a) the side view and top view of an AFSD deposit and (b) the MELD – R2 system used for all experiments in this work.

2.2. Fundamental Physical Principles of Friction Stir

Additive Friction Stir Deposition (AFSD) is a friction stir technique similar to the more established methods of Friction Stir Welding (FSW) and Friction Stir Processing (FSP). From an application perspective, AFSD is intended for fabrication of bulk components whereas FSW and FSP are used for bonding and surface treatment, respectively. Fundamentally, these processes share the same defining scientific principles which include: 1) Frictional Heat Generation through dynamic contact and 2) Continuous Plastic Deformation [21, 22]. This is accomplished by bringing a rotating tool into contact with a stationary substrate or joint. Here, the tool contact interface acts as a heat generation source whereby interfacial heat generation depends on the stick-slip ratio. This contact region also initiates bulk deformation which additionally contributes to heat generation. Surface features on the tool may vary significantly based on processing intentions and have significant impact on the heat generation and material flow. The most common type of feature is a pin or protrusion (Fig. 2.2) that facilitates continuous plastic deformation in the processing zone.

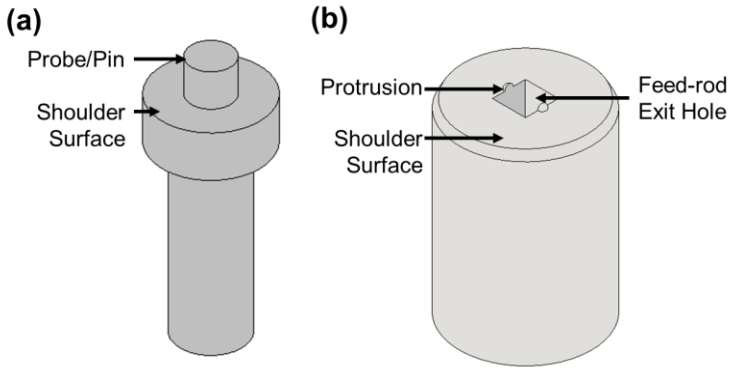

Figure 2.2. A schematic showing the key differences in tool geometry for (a) friction stir welding and (b) additive friction stir deposition

Heat Generation

Many models for the heat generation in FSW exist in literature varying from analytical thermal models, to finite element (FE) models, and computational fluid dynamic models each with their own advantages and disadvantages. The most complete description of heat generation involves three different heat sources, the most basic of which is Coulomb friction $\tau = \mu P$, where shear, τ, is related to the dynamic/static friction coefficient, μ, and applied normal force, *P* [23]. Also present at the tool material interface is the constant shear model, which defines plastic deformation at the interface proportional a sticking constant, δ, as a $\tau = \delta\sigma_y$ and the material yield stress, σ_y The final major heat generation mechanism is a result of the continuous plastic deformation with the thermomechanically affected zone. At large strains and strain rates, such as those typically associated with FSW/P the conversion factor, β, of deformation energy to heat energy is assumed to be 1 [24]. It is unclear how much of the heat input is generated by each independent mechanism, however most literature agrees that the interfacial combination of coulomb friction and constant shear dominates over the plastic deformation [25].

Material Flow

Material flow occurs in the bulk of the processing zone and generally consists of three distinct flow patterns [26]. The first flow pattern is induced by the interaction of the shoulder and the material that causes material to flow radially along the tool surface. The vertical sides of the pin contribute to the second method of material flow which is generally observed to be from top to bottom of the pin. Finally, the bottom surface of the pin is noted for surging material away from the tool center and upwards towards the shoulder. The degree of material flow in all of these cases is proportional to the sticking coefficient δ at

these different radial positions and linear velocities. Critically, the materials properties and the nature of this material flow will depend on the thermal cycling since the heat generation will lead to additional softening and conversely the plastic deformation will generate additional heat and softening. Modeling of material flow during FSW is often performed through computational fluid dynamics (CFD) modeling methods and treat the processing zone as a non-Newtonian viscous fluid [27, 28].

Distinct Processing Zones

In general, FSW literature describes the formation of 4 distinct areas with distinct thermomechanical processing histories and microstructure evolution. The Stir Zone or Nugget Zone is described by the highest temperatures and strain rates of the processed region. Typically, this area makes up the zone directly adjacent to the tool shoulder and pin. A partial sticking-slipping condition with the nearby material generates a very steep shear stress gradient between this area and the stationary substrate. The stir zone is also the area with the greatest degree of grain refinement and is typically dominated by dynamic recovery or dynamic recrystallization. Moving further away radially from the tool pin the thermomechanically affected zone can be observed (TMAZ). Here, the stress gradient is still present, however not as intensive as in the stir zone. Here, the dynamic restoration mechanisms are still present, but static restoration mechanisms also become prevalent. Deformation in this region is often associated with a shear texture. The heat affected zone (HAZ) has no mechanical interaction with the tool or deforming material. This area is heated by conduction from the tool to the substrate and may experience grain growth and static restoration mechanisms depending on the starting microstructure of the substrate. The not-affected zone (NAZ) is defined by areas far from the welding procedure that see

no microstructural change. The microstructural evolution of these distinct zones is a compelling reason to investigate the thermomechanical processing history. For AFSD, all of these zones are expected to be present to different extents based on the tool geometry and processing conditions. However, a key distinction is the orientation is in the vertical direction rather than the horizontal direction. Generally, it is observed that the currently processed layer and an area extending into the previous layer or substrate see massive grain refinement compared to the base material. This is analogous to the stir zone of FSW.

AFSD is unique in that the tool head has a hollow channel through which feed-material can be extruded. Initially, the solid feed-rod rapidly rotates with the tool head and is continuously pushed out of the hollow channel by a uniaxial actuator. When the rotating feed-rod contacts the stationary substrate, the interaction at the material-substrate interface generates frictional heat. In turn, this leads to thermal softening of the feed-rod and yielding under the compressive normal force. This initial macroscopic shape change also changes the expected thermomechanical processing history and may have a significant influence on the microstructural development. The combined compressive forces from the feeding apparatus and the shearing forces from the rotating tool head cause the feed-rod and substrate to plasticize and mix. This rapid plastic deformation results in additional volumetric heat generation. In-plane motion of the substrate relative to the tool leads to deposition of a single track of material with good interfacial bonding. Here, the key equipment process variables can be defined as the tool rotation rate Ω, the tool in-plane velocity V, and the material feed rate F. The combination of these process variables is expected to determine the stress, strain rate, and total heat input experienced by the material during processing.

References

[1] Ngo, T.D., Kashani, A., Imbalzano, G., Nguyen, K.T.Q., Hui, D., Additive manufacturing (3D printing): A review of materials, methods, applications and challenges, Composites Part B: Engineering 143 (2018) 172-196.

[2] Tofail, S.A.M., Koumoulos, E.P., Bandyopadhyay, A., Bose, S., O'Donoghue, L., Charitidis, C., Additive manufacturing: scientific and technological challenges, market uptake and opportunities, Materials Today 21(1) (2018) 22-37.

[3] Gibson, I., Rosen, D., Stucker, B., Binder Jetting, in: I. Gibson, D. Rosen, B. Stucker (Eds.), Additive Manufacturing Technologies: 3D Printing, Rapid Prototyping, and Direct Digital Manufacturing, Springer New York, New York, NY, 2015, pp. 205-218.

[4] Tang, Y., Zhou, Y., Hoff, T., Garon, M., Zhao, Y.F., Elastic modulus of 316 stainless steel lattice structure fabricated via binder jetting process, Materials Science and Technology 32(7) (2016) 648-656.

[5] Gibson, I., Rosen, D., Stucker, B., Directed Energy Deposition Processes, Additive Manufacturing Technologies: 3D Printing, Rapid Prototyping, and Direct Digital Manufacturing, Springer New York, New York, NY, 2015, pp. 245-268.

[6] Pegues, J.W., Melia, M.A., Puckett, R., Whetten, S.R., Argibay, N., Kustas, A.B., Exploring additive manufacturing as a high-throughput screening tool for multiphase high entropy alloys, Additive Manufacturing (2020) 101598.

[7] Lu, X., Lin, X., Chiumenti, M., Cervera, M., Hu, Y., Ji, X., Ma, L., Yang, H., Huang, W., Residual stress and distortion of rectangular and S-shaped Ti-6Al-4V parts by Directed Energy Deposition: Modelling and experimental calibration, Additive Manufacturing 26 (2019) 166-179.

[8] Huang, S.H., Liu, P., Mokasdar, A., Hou, L., Additive manufacturing and its societal impact: a literature review, The International Journal of Advanced Manufacturing Technology 67(5) (2013) 1191-1203.

[9] Ahn, S.H., Montero, M., Odell, D., Roundy, S., Wright Paul, K., Anisotropic material properties of fused deposition modeling ABS, Rapid Prototyping Journal 8(4) (2002) 248-257.

[10] Sui, Y., Zorman, C.A., Review—Inkjet Printing of Metal Structures for Electrochemical Sensor Applications, Journal of The Electrochemical Society 167(3) (2020) 037571.

[11] Derby, B., Additive Manufacture of Ceramics Components by Inkjet Printing, Engineering 1(1) (2015) 113-123.

[12] Sames, W.J., List, F.A., Pannala, S., Dehoff, R.R., Babu, S.S., The metallurgy and processing science of metal additive manufacturing, International Materials Reviews 61(5) (2016) 315-360.

[13] Gibson, I., Rosen, D.W., Stucker, B., Sheet Lamination Processes, in: I. Gibson, D.W. Rosen, B. Stucker (Eds.), Additive Manufacturing Technologies: Rapid Prototyping to Direct Digital Manufacturing, Springer US, Boston, MA, 2010, pp. 223-252.

[14] Halloran, J.W., Ceramic Stereolithography: Additive Manufacturing for Ceramics by Photopolymerization, Annual Review of Materials Research 46(1) (2016) 19-40.

[15] Lee, Y.S., Kirka, M.M., Dinwiddie, R.B., Raghavan, N., Turner, J., Dehoff, R.R., Babu, S.S., Role of scan strategies on thermal gradient and solidification rate in electron beam powder bed fusion, Additive Manufacturing 22 (2018) 516-527.

[16] Li, C., Liu, Z.Y., Fang, X.Y., Guo, Y.B., Residual Stress in Metal Additive Manufacturing, Procedia CIRP 71 (2018) 348-353.

[17] Bayat, M., Thanki, A., Mohanty, S., Witvrouw, A., Yang, S., Thorborg, J., Tiedje, N.S., Hattel, J.H., Keyhole-induced porosities in Laser-based Powder Bed Fusion (L-PBF) of Ti6Al4V: High-fidelity modelling and experimental validation, Additive Manufacturing 30 (2019) 100835.

[18] Friel, R.J., Harris, R.A., Ultrasonic Additive Manufacturing – A Hybrid Production Process for Novel Functional Products, Procedia CIRP 6 (2013) 35-40.

[19] Palanivel, S., Sidhar, H., Mishra, R.S., Friction Stir Additive Manufacturing: Route to High Structural Performance, JOM 67(3) (2015) 616-621.

[20] Schultz, J.P., Creehan, K.D., Friction stir fabrication, Aeroprobe Corporation, 2014.

[21] Mishra, R.S., De, P.S., Kumar, N., Friction Stir Welding and Processing: Science and Engineering, Springer International Publishing2014.

[22] Mishra, R.S., Ma, Z.Y., Friction stir welding and processing, Materials Science and Engineering: R: Reports 50(1) (2005) 1-78.

[23] Bhushan, B., Ko, P., Introduction to Tribology, Applied Mechanics Reviews 56 (2003) B6.

[24] Rosakis, P., Rosakis, A.J., Ravichandran, G., Hodowany, J., A thermodynamic internal variable model for the partition of plastic work into heat and stored energy in metals, Journal of the Mechanics and Physics of Solids 48(3) (2000) 581-607.

[25] Colegrove, P.A., 3 Dimensional Flow and Thermal Modelling of the Friction Stir Welding Process, University of Adelaide, Department of Mechanical Engineering2001.

[26] Tozaki, Y., Uematsu, Y., Tokaji, K., Effect of tool geometry on microstructure and static strength in friction stir spot welded aluminium alloys, International Journal of Machine Tools and Manufacture 47(15) (2007) 2230-2236.

[27] Hamza, E., A review of using Computational Fluid Dynamic in simulating of Friction Stir Welding and Parametric studies, 2016.

[28] Neto, D.M., Neto, P., Numerical modeling of friction stir welding process: a literature review, The International Journal of Advanced Manufacturing Technology 65(1) (2013) 115-126.

Chapter 3

In Situ Investigation into Temperature Evolution and Heat Generation during Additive Friction Stir Deposition: A Comparative Study of Cu and Al-Mg-Si

3.0. Abstract

Additive friction stir deposition is an emerging solid-state additive manufacturing technology that enables site-specific build-up of high-quality metals with fine, equiaxed microstructures and excellent mechanical properties. By incorporating proper machining, it has the potential to produce large-scale, complex 3D geometries. Still early in its development, a thorough understanding of the thermal process fundamentals, including temperature evolution and heat generation mechanisms, has not been established. This work aims to bridge this gap through *in situ* monitoring of the thermal field and material flow behavior using complementary infrared imaging, thermocouple measurement, and optical imaging. Two materials challenging to print via beam-based additive technologies, Cu and Al-Mg-Si, are investigated. During additive friction stir deposition of both materials, similar trends of thermal features (e.g., the trends of peak temperature T_{Peak},

exposure time, and cooling rate) are observed with respect to the processing conditions (e.g., the tool rotation rate Ω and in-plane velocity V). However, there is a salient, quantitative difference between Cu and Al-Mg-Si; T_{Peak} exhibits a power law relationship with Ω/V in Cu but with Ω^2/V in Al-Mg-Si. This difference is directly correlated to the distinct interfacial contact states that are observed through *in situ* material flow characterization. In Cu, the interfacial contact between the material and tool head is characterized by a full slipping condition, so interfacial friction is the dominant heat generation mechanism. In Al-Mg-Si, the interfacial contact is characterized by a partial slipping/sticking condition, so both interfacial friction and plastic energy dissipation contribute significantly to the heat generation.

3.1. Introduction

While most metal additive manufacturing technologies to date have been based on selective melting and rapid solidification of powders or wires (i.e. beam-based additive technologies) [1-3], a series of *solid-state* metal additive manufacturing technologies have recently emerged that provide a low-energy pathway to achieving net-shaping or near-net-shaping with reduced heat input, thermal gradient, and residual stresses [4-6]. These solid-state technologies exploit deformation bonding to enable material adhesion via friction stir [7], ultrasonic vibration [8], or cold gas spraying [9]. The most recognized examples include additive friction stir deposition (AFSD) [10], friction stir additive manufacturing (FSAM) [11], ultrasonic additive manufacturing (UAM) [12], and cold spray [13]. By integrating the friction stir principle [14, 15] with a robust material feeding mechanism [16], AFSD stands out as a free-form process allowing for site-specific deposition with

good quality and properties in the as-printed state. With incorporation of proper machining processes, it has the potential for creating complex 3D geometries on a large-scale. FSAM and UAM are hybrid sheet-lamination technologies that require additional subtractive processes for shaping newly bonded layers. Cold spray also enables site-specific deposition but generally requires post-processing to improve mechanical properties. With the unique benefits, AFSD has drawn great attention in the fields of multi-material additive manufacturing [17-20], selective-area coating and cladding [21], and additive repair [22].

In AFSD, a solid-state feed-rod is delivered through a hollow tool head as shown in Fig. 3.1(a). The tool head and feed-rod assembly rapidly rotate at a rotation rate, Ω, of $\sim 10^2$–10^3 revolutions per minute (RPM). When the rotating feed-rod contacts the stationary substrate, the dynamic interaction at the material-substrate interface generates frictional heat, which in turn leads to thermal softening of the feed-rod. The combined compressive forces from the feeding apparatus and the shearing forces from the rotating tool head cause the feed-rod to plasticize and mix with the surface of the substrate. Rapid plastic deformation results in additional volumetric heat generation [23]. Furthermore, the tool surface features, such as protrusions, can generate additional frictional heat and enhance the material flow and mixing between the deposit and substrate. With co-deformation and mixing of the deposited material and substrate surface layers, in-plane motion of the substrate relative to the tool head leads to deposition of a single track of material with good interfacial bonding. During deposition, the material undergoes severe plastic deformation at elevated temperatures and high strain rates [24]. The accompanied continuous or discontinuous dynamic recrystallization gives rise to refined, equiaxed grains and excellent mechanical properties [6, 10, 21] in the as-printed state. This is a salient advantage as

compared to conventional beam-based metal additive manufacturing processes, wherein the melting and solidification will result in cast-type microstructures featuring columnar and dendritic grains [25-28]. While these features can be avoided by controlling solidification via the introduction of nanoparticles [29] or very precise manipulation of transient thermal gradients [30], the associated efforts are time-consuming and expensive.

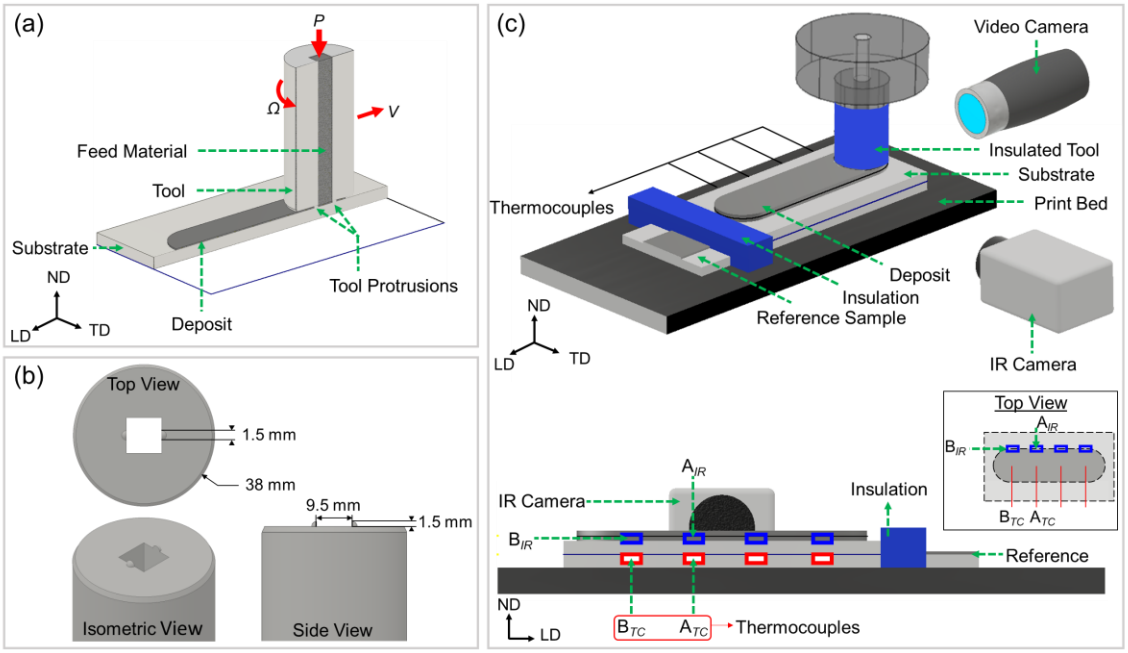

Fig. 3.1. An illustration of (a) the AFSD process, (b) the tool head including surface features and dimensions, and (c) the monitoring set-up. A_{TC} and B_{TC} are two locations in the substrate with the temperature measured by the thermocouples, whereas A_{IR} and B_{IR} are two locations in the first-layer of the deposited material with the temperature measured by the IR camera. A_{IR} and B_{IR} are directly above A_{TC} and B_{TC}. ND, TD, and LD refer to the normal direction, transverse direction, and longitudinal direction, respectively.

As in any metal additive manufacturing technology, the temperature evolution during AFSD controls the print quality, the microstructure, and the properties of the as-printed material. To investigate temperature evolution in AFSD, the distinctive consideration of material flow is necessary. On one hand, the material flow determines the volumetric energy produced from plastic deformation [31] and contributes to heat transfer via convective heat flow [32]. On the other hand, the material flow is influenced by the temperature distribution inside the deposited material, because the constitutive material properties —such as dynamic viscosity and flow stress — are strongly temperature dependent [33]. Therefore, as a friction stir-derived technology, the heat flow and material flow are fully coupled in AFSD.

AFSD research is at an early stage with a critical need for understanding the process fundamentals, especially the important thermal aspects. This necessitates direct experimental characterization of the temperature evolution and material flow during AFSD. For direct measurement of temperature evolution in the deposited material, AFSD shares many of the challenges as in friction stir welding (FSW) and friction stir processing (FSP) [34-36]. For example, thermocouples are challenging to embed within the processing zone because the large amounts of plastic deformation would likely destroy any physical sensors [37, 38]. In addition, the tool in FSW, FSP, and AFSD obscures the stir zone or deposition zone, making it challenging to monitor the temperature evolution by top-view characterization (i.e., along the normal-direction). However, an important difference in AFSD is that the deposited material lies on top of the substrate, whereas in FSW or FSP the stir zone is internal to the workpiece material. Consequently, AFSD allows for direct measurement of the temperature evolution in the deposited material using non-contact

methods from the side view, which can be implemented using infrared cameras or pyrometers [39, 40]. For the same reason, the visualization of material flow is challenging in FSW and FSP; however, the surface of material flow can be directly monitored in AFSD from the side view.

The aim of this work is to gain physical insights into the process fundamentals of additive friction stir deposition via direct characterization of the temperature evolution, material flow, and heat generation mechanisms using in situ monitoring approaches. Infrared (IR) thermal imaging technology is employed to monitor the temperature evolution in the deposited material from the side view and embedded thermocouples in the substrate plate directly below the deposited material offer complementary thermal measurements. Meanwhile, the material flow is monitored from the leading side of the deposit to provide valuable insights into the heat generation mechanisms. This work investigates deposition of two specific material systems, Cu and Al-Mg-Si, which are challenging to print using beam-based additive technologies due to the high thermal conductivity, high reflectivity, or susceptibility to hot cracking [41, 42]. AFSD is a promising additive technology for Cu and Al-Mg-Si, because these materials are known to be well processed using the friction stir principle [32]. Cu and Al-Mg-Si differ in their thermomechanical responses; during forging Al-alloys undergo plastic flow more readily than Cu and Al-alloys are recognized for easier forgeability [43]. A comparative study of these two materials allows us to explore the linkage between the thermomechanical properties of material and the consequential heat generation and thermal characteristics in AFSD.

3.2. Experimental procedures

3.2.1. Material deposition

All AFSD experiments were performed using a MELD R2 system (MELD Manufacturing Corporation, Christiansburg VA, USA) and a 38 mm-wide steel tool head. The tool surface had two protrusions with rounded surfaces and a height of 1.5 mm located immediately surrounding the feed-rod exit hole (see Fig. 3.1(b)). The build geometry of each experiment was a stack of two deposited layers with single-layer thickness of approximately 0.8 mm and a nominal length of 70.2 mm. Two different material systems were studied: (1) Cu (commercially pure), and (2) a commercially available Al-Mg-Si alloy, AA 6061. In both cases, the substrate and the deposited material had the same composition. Substrate plates were 6.35 mm × 76.2 mm × 127 mm. Raw feed material was in the form of square rod with a side length of 9.5 mm. Depositions were systematically performed at various AFSD processing conditions. The selected tool rotation rates included 300 RPM, 600 RPM, and 900 RPM, and the selected in-plane tool velocities included 1.00 mm/s, 2.00 mm/s, and 3.00 mm/s. The ratio between the material feed rate to the tool in-plane velocity was used to control the volumetric deposition rate and kept constant throughout all experiments at a value of 1:3.

3.2.2. Thermal measurement

In this work, thermographic measurements were performed using a Micro-Epsilon TIM 400 infrared (IR) camera, which was mounted onto the bed of the AFSD system and shared the same reference frame as the print geometry. Temperature calibration of the IR camera was performed using AFSD-printed Cu and Al-Mg-Si samples, which were heated using a Fisher Scientific Hot-Plate under ambient conditions. By matching the IR outputs with the readings from a pre-calibrated thermocouple, the emittance for a given material (Cu or Al-Mg-Si) was calibrated [30, 44]. This procedure was repeated at 50 K increments. Additional modifications were made to the typical AFSD setup, where the rotating tool and the spindle were covered with fiberglass insulation to prevent undesirable radiative interference (e.g., reflections). During AFSD, a piece of Cu or Al-Mg-Si kept at known elevated temperatures was placed in the camera field of view to serve as a temperature reference. The IR camera had a capture rate of 80 Hz with 382 × 288 pixels in the field of view. The IR camera was positioned perpendicular to the side of the deposit at 11 cm. The pixel size provided sufficient resolution to distinctly measure the temperature of each layer while still providing a large field of view to capture the entire length of the deposit.

In addition to IR thermal measurement, a thermocouple array (K-type) was employed to continuously measure local temperatures in the substrate directly beneath the deposited material. Shallow grooves for thermocouple leads were cut into a second substrate plate, which was clamped underneath the primary substrate. Each groove was filled with a conductive thermal paste to improve the contact conditions and response time. Thermocouple data-logging was accomplished using Adafruit thermocouple amplifiers and an Arduino Nano microcontroller.

3.2.3. Monitoring of material flow

Optical video recording of the material flow was performed on the leading edge of the deposit using a Dino-Lite Edge AM4115ZT Microscope. The camera had a spatial resolution of 1280 × 1024 pixels with a pixel size of 0.03 mm × 0.03 mm at the given field of view. The optical camera was positioned perpendicular to the leading edge of the deposit at a distance of 8 cm. A high-temperature black primer was speckled onto the surface of the deposit during AFSD, in order to track the motion of the material relative to the tool head. The black speckles provided contrast on the surface of the deposited material and were individually tracked to monitor the motion of the deposited material. Comparison of the velocity of the speckles to the tool head rotation provided valuable insights into the stick-slip phenomena in each material system. Fig. 3.1(c) schematically shows how the infrared thermal imaging, thermocouple measurement, and optical video recording are incorporated into the present AFSD system.

3.3. In situ characterization of temperature evolution during AFSD of Cu and Al-Mg-Si

3.3.1. Qualitative overview of thermal field evolution in AFSD

AFSD is composed of three distinct processing phases (1) plunge, (2) in-plane motion, and (3) out-of-plane layer transition. In the plunge phase, the rotating feed-rod is slowly pushed downward through the center of the tool head by the feeding apparatus so that it makes contact with the stationary substrate. Initially, heat is generated by Coulomb friction at the feed-rod and substrate interface until the material has substantially softened and begins to plasticize. During plasticization, the majority of the plastic work is converted to

heat, resulting in an additional volumetric heat generation mechanism. The continuously plasticizing material extrudes radially until the space beneath the rotating tool is saturated. The in-plane motion phase then begins, where the substrate is set in motion relative to the rotating tool; as a result, material is continuously deposited onto the substrate. Once the desired geometry has been traced by the in-plane motion and a layer is complete, the out-of-plane layer transition phase begins, in which the print bed lowers in the out-of-plane direction by the desired layer thickness.

An overview of the measured thermal field evolution during these phases is shown in Figs. 3.2 (a)-(f), which consist of several representative snapshots from a thermal video for a two-layer Cu deposition. The complete thermal video is available in the Supplemental Information. Time step t = 0 s corresponds to the thermal profile of the plunge phase. The in-plane motion phase is seen at t = 25 s where the print bed translates relative to the rotating tool. The track behind the tool head remains at an elevated temperature as it cools down through boundary heat losses (conduction, convection, and radiation). At t = 35 s, the layer transition begins. At t = 55 s, the second layer is being deposited, where the relative motion between the print bed and the tool is in the opposite direction to the first layer of deposition. At t = 75 s, the desired two-layer geometry is complete, and the print bed is lowered as the feed-rod detaches from the deposit. The final thermal image shows a bowl-shaped high temperature zone surrounding the end of deposition, which corresponds to the expected temperature distribution resulting from a moving heat source [45].

Based on the temperature measurement at a given spot, typical temperature evolution history (i.e., *T-t* plot) of the deposited material is shown in Fig. 3.2 (g), showing two distinct peaks. The first peak corresponds to the deposition of new material at Spot A_{IR} (see Fig.

3.1(b) for the location), T_{Peak}. This is an intrinsic thermal characteristic depending on the AFSD processing parameters and tool-material interactions. The heating portion in the first peak is not physically meaningful because no material is initially present in the field of view. The measured 'heating rate' mostly reflects the IR camera response time rather than the temperature increase rate in the deposited material. The second peak corresponds to deposition of the second layer directly above Spot A_{IR}, clearly showing a strong reheating effect between layers in AFSD. The value of the second temperature peak depends on the print geometry, tool path, and the transition time between deposition of the first and second layer, so it is not an intrinsic thermal characteristic in AFSD. Note that the flat curve seen at ~450 K results from the limits of the measurable temperature range by the IR camera.

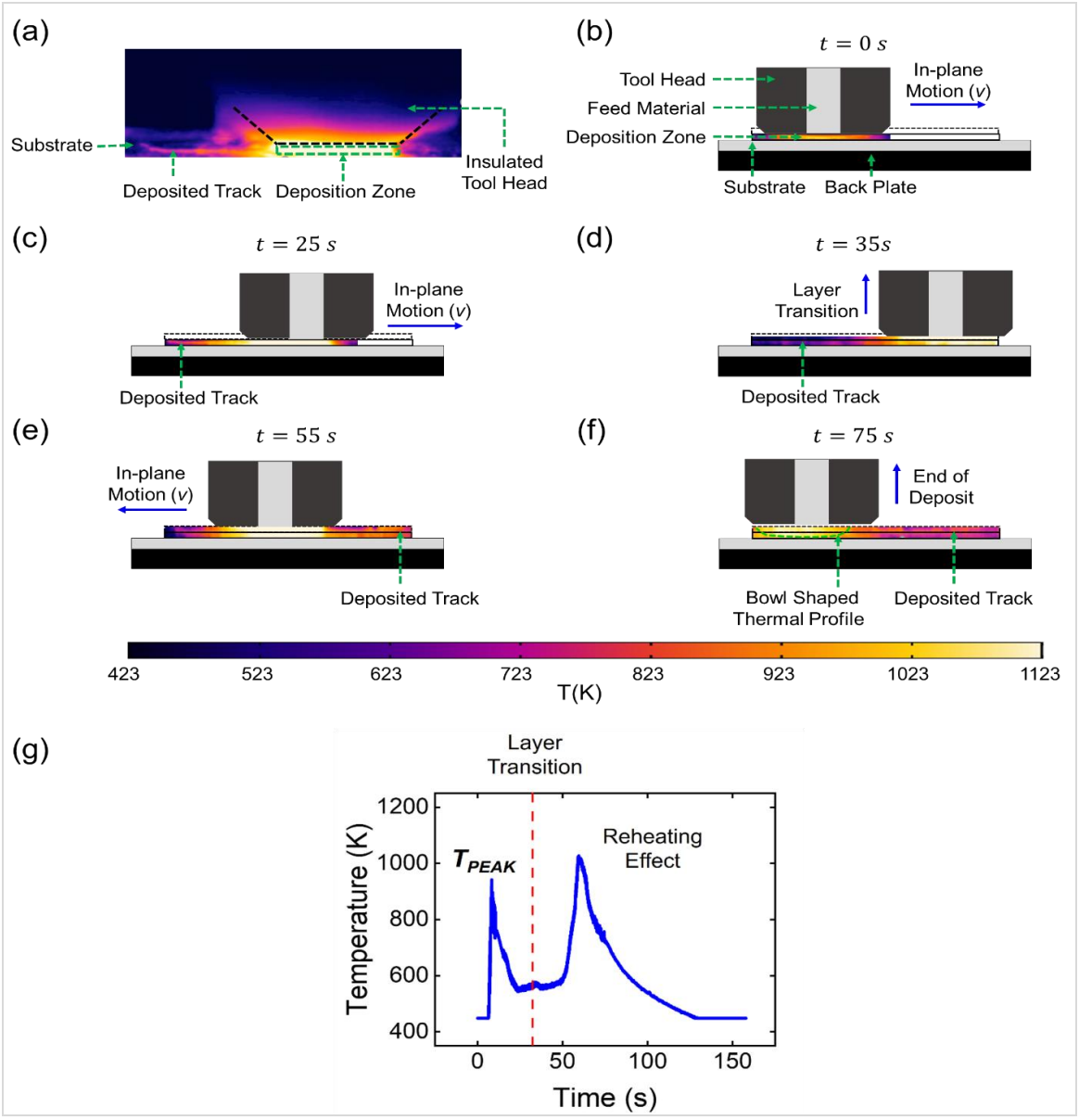

Figure 3.2. An overview of the thermal profile for Cu deposited at 600 RPM and 1 mm/s in-plane velocity. (a) A representative thermal image of the entire field of view during AFSD. (b)-(f) The different time steps show the measured temperature field directly beneath the tool head, cooling of the deposited material at the far-from-the-tool position, and a bowl-shaped heat profile associated with a moving heat source. (g) A plot of the temperature history measured for a single spot of the deposit that demonstrates a temperature peak due to deposition and a substantial reheating effect.

3.3.2. Dependence of peak temperature on AFSD processing conditions

The temperature field evolution has been systematically investigated for various AFSD processing conditions. For all successful Cu depositions without apparent defects in this work, the peak temperature T_{Peak} lies in the range of 49% to 79% of the melting temperature T_M. For all successful Al depositions, T_{Peak} lies in the range of 76% to 92% of T_M. This is consistent with the fact that the yield strength of Cu drops more rapidly than structural Al alloys as temperature increases [46, 47], so Cu can be friction stirred at a lower homologous temperature [48].

The trend of the peak temperature T_{PEAK} with respect to the AFSD processing parameters, such as the tool head rotation rate Ω and in-plane velocity V, is studied for both Cu and Al-Mg-Si. As plotted in Fig. 3.3, T_{Peak} shows a strong dependence on AFSD processing conditions, with Cu and Al-Mg-Si exhibiting similar trends. For a given tool rotation rate Ω, it is observed that T_{Peak} decreases with increasing the tool in-plane velocity V. For a given V, T_{Peak} increases with increasing Ω. This trend is similar to that observed in FSW literature [49-52], which can be explained as follows: an increase of the tool rotation rate Ω is expected to increase the heat generation rate resulting from friction at the material-tool head interface, which leads to a positive correlation between T_{Peak} and Ω. With a higher in-plane velocity V, the material feed rate is higher, and more material is deposited for a given period of time, so the heat input is lower per unit material volume. This leads to a negative correlation between T_{Peak} and V.

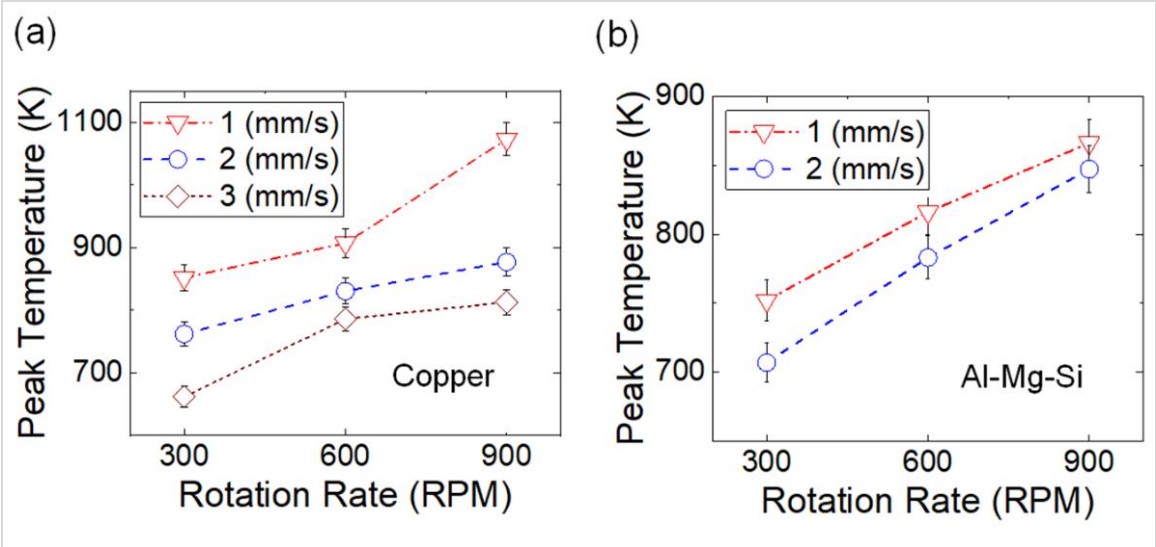

Figure 3.3. Plots showing the peak temperature measured during deposition of the first layer at various processing conditions for (a) Cu and (b) Al-Mg-Si. In general, processing conditions with lower traverse rate and higher rotation rate produce higher peak temperatures. Error bars signify expected measurement error from the IR camera.

Quantitatively, it is found that the peak temperature in AFSD is well described by power law relationships with the processing parameters. Arbegast has proposed an empirical power law equation of the peak temperature in FSW of Al alloys [53]: $T_{Peak}/T_M = K(\Omega^2/V)^a$, where K and a are fitting constants and Ω^2/V is a pseudo-heat index described by the key processing parameters. Using this type of relationship, the fitting results of the measured AFSD peak temperature are shown in Fig. 3.4 (a) and Fig. 3.4(b) for Cu and Al-Mg-Si, respectively. The peak temperature in Al-Mg-Si is well predicted by the heat index of Ω^2/V with an R-squared value of 0.98 in the ln-ln plot. For Cu, the fitting is relatively poor with an R-squared value of 0.81. Fig. 3.4 (c) and Fig. 3.4(d) plot the fitting results of peak temperature using a pseudo-heat index of Ω/V instead, i.e., $T_{Peak}/T_M = K(\Omega/V)^a$, showing a good fit of the Cu peak temperature with an R-squared

value of 0.95 in the ln-ln plot. In contrast, the Al-Mg-Si peak temperature does not fit well with an R-squared value of 0.87. Therefore, the peak temperature in Cu forms a power law equation with Ω/V, whereas the peak temperature in Al-Mg-Si forms a power law equation with Ω^2/V.

Based on the fitting results in Fig. 3.4, the peak temperature of Cu and Al-Mg-Si during AFSD is best described by Equations 1 and 2, respectively:

$$\frac{T_{Peak}}{T_M} = K_{Cu}\left(\frac{\Omega}{V}\right)^{0.2}, \text{ for Cu.} \quad (1)$$

$$\frac{T_{Peak}}{T_M} = K_{Al}\left(\frac{\Omega^2}{V}\right)^{0.07}, \text{ for Al-Mg-Si.} \quad (2)$$

Here, K_{Cu} and K_{Al} are fitting constants. In Arbegast's empirical fitting, the power a is found to be in the range of 0.04 to 0.06 for FSW of Al alloys. To compare, Equation (2) shows a comparable power value of 0.07 in AFSD of Al-Mg-Si, suggesting similar heat generation mechanisms in AFSD and FSW of Al alloys. For Cu, however, the peak temperature exhibits a power law relationship with Ω/V rather than Ω^2/V, suggesting differences in the heat generation mechanisms. This finding correlates to the distinct interfacial contact states and material flow behaviors between Cu and Al-Mg-Si, which will be elaborated in Sections 3.4 and 3.5. Note that the goal of fitting here is to show the different temperature evolution behavior between Cu and Al-Mg-Si; the latter is much more consistent with the Arbegast model than the former. The intent is not to determine the exact fitting constants in the power laws, which may be challenging to achieve based on the limited data points in Fig. 3.4.

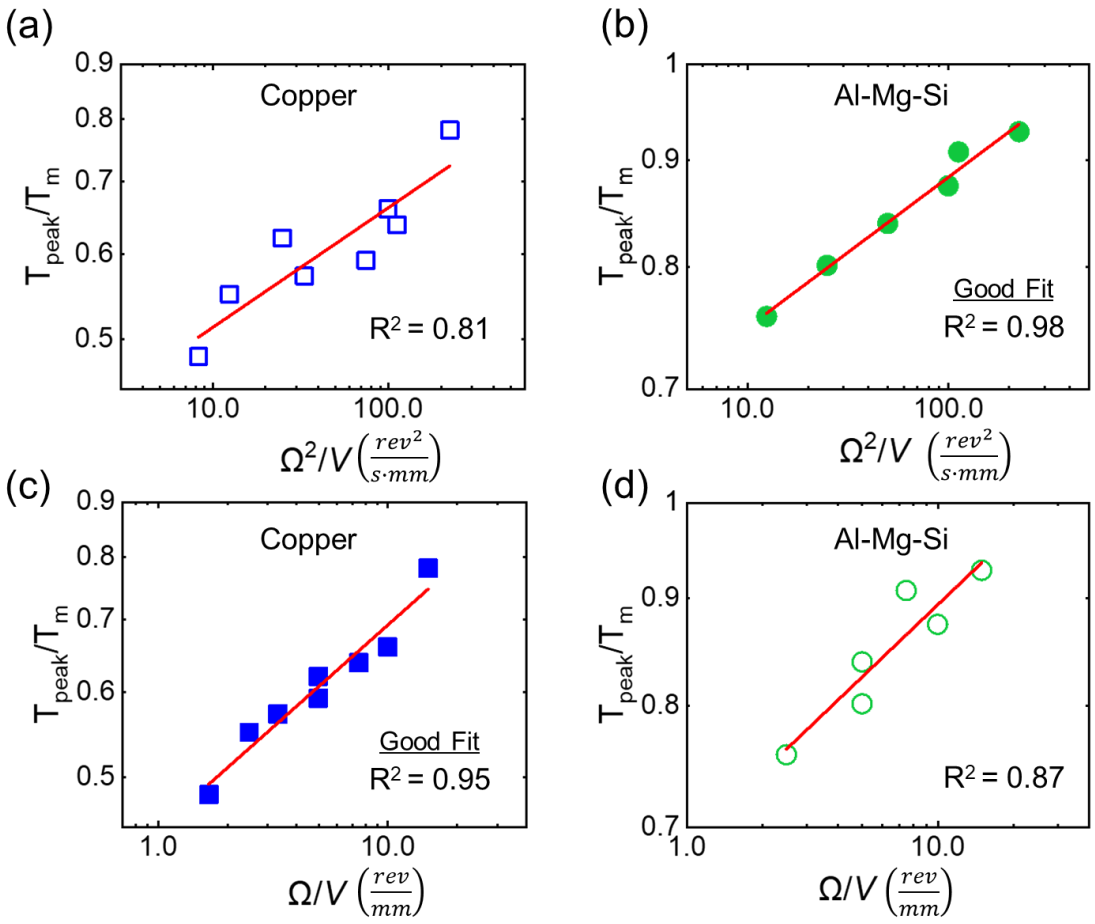

Figure 3.4. Fitting of a power law relationship to the homologous peak temperature and the processing parameters with a relationship of (a, b) Ω^2/V and (c, d) Ω/V. Here, revolutions/second (rev/s) is used for the unit of Ω and millimeter/second (mm/s) is used as the unit for V. The peak temperature for Cu shows a better fitting with Ω/V, whereas Al-Mg-Si has a better fitting with Ω^2/V.

3.3.3. Trends of exposure time, heating rate, and cooling rate

In additional to peak temperature, other important thermal characteristics include the exposure time, heating rate, and cooling rate, which can be conveniently extracted from the *T-t* plot (e.g., see Fig. 3.2 (g)). The goal here is to understand how these thermal characteristics change with respect to the AFSD processing parameters. The exposure time and heating rate estimates are based on the second peak in the T-t plot, because the heating portion of the first peak only reflects the response time of IR camera as explained in section 3.3.1. As such, this essentially measures the reheating effect arising from the deposition of a new layer. The cooling rate estimate is based on both the first and the second peak in the *T-t* plot, which are found to have the same trend with respect to the AFSD processing parameters.

The exposure time is the length of time that the deposited material experiences high temperatures, which is experimentally determined by finding the full width at half maximum of the peak temperature in the *T-t* plot. Figs. 3.5 (a) and (b) clearly show that the exposure time decreases with an increase of V. This trend can be explained by considering the positive correlation between the exposure time and the time of material interaction with the tool head. The latter can be roughly estimated as the ratio between the deposition radius and the tool in-plane velocity and will decrease with an increase of V. As a result, the exposure time also decreases with an increase of V as seen in Figs. 3.5 (a) and (b). The exposure time increases with the tool head rotation rate Ω as concluded from the same plots. This trend is expected because a higher rotation rate Ω leads to a higher peak temperature (when the in-plane velocity remains constant). It generally takes more time to cool down from a higher peak temperature, so the exposure time is longer.

The instantaneous heating and cooling rates are time dependent. From an engineering perspective, the average heating and cooling rates are defined by the linear regions of the second peak in the *T*-*t* plot. This is associated with a wide temperature range with respect to T_{Peak}. In this work, the lower bound of the temperature range is set to be 30 % above the lowest measurable temperature of the IR camera (~600 K for Cu and ~500 K for Al-Mg-Si). With this setting, the interference from the first temperature peak can be avoided and good linear fitting can be achieved in the *T*-*t* plot. The slope of the linear fitting (in absolute value) is used as the heating or cooling rate. Figs. 3.5 (c) and (d) plot the heating rate under various AFSD processing conditions, which is generally in the range of 20 – 80 K/s. At a high in-plane velocity V, the heat source quickly approaches a given point and results in a rapid transition from the idle temperature to the peak temperature. Thus, the heating rate shows a positive correlation with the tool velocity *V*. Figs. 3.5 (e) and (f) plot the trends of the cooling rate, which is measured to be in the range of 5 – 25 K/s. For both Cu and Al-Mg-Si, lower cooling rates are found to occur at higher Ω and lower *V*, which corresponds to conditions with higher peak temperature and more total heat input. This trend can be explained as follows. Under conditions of high Ω and low *V*, the heat input is large, and significant preheating occurs in the substrate material ahead of the moving tool head. As a result, the local temperature gradient ∇T is reduced across the newly deposited material and the substrate below, leading to a lower cooling rate—as long as the thermal conduction into the substrate is a major cooling mechanism. This has been confirmed in the Appendix, in which the substrate temperature evolution is used to evaluate the contribution of different cooling mechanisms during AFSD of Cu and Al-Mg-Si, including thermal conduction, air convection, and radiation.

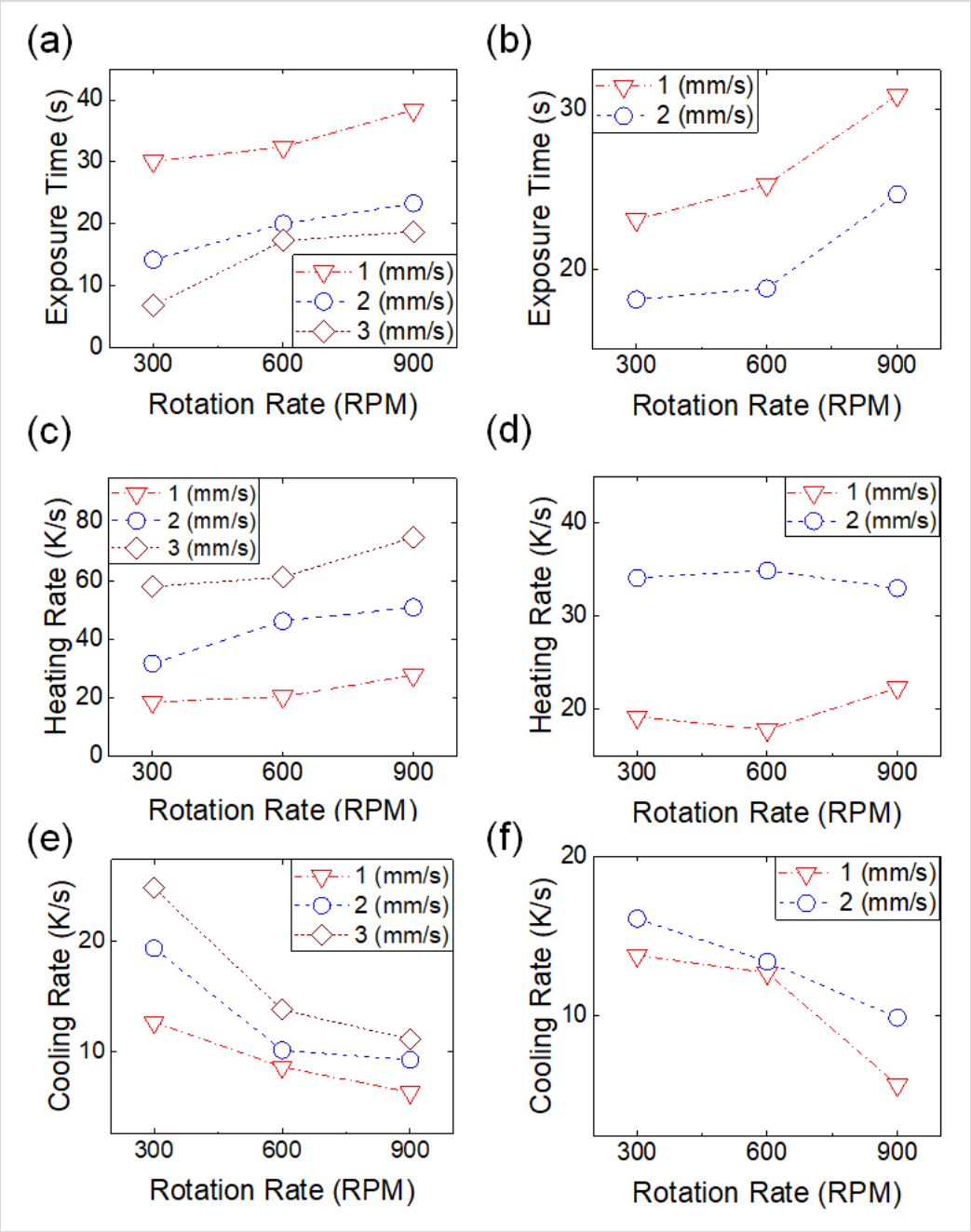

Figure 3.5. Plots of (a, b) the exposure time, (c, d) the heating rate, and (e, f) the cooling rate as a function of the AFSD processing parameters. The left column corresponds to the data of Cu and the right column corresponds to Al-Mg-Si. Generally, the exposure time increases with increasing Ω and decreasing V, the heating rate increases with increasing V, and the cooling rate increases with decreasing Ω and increasing V.

3.4. In situ characterization of material flow during AFSD of Cu and Al-Mg-Si

From the *in situ* thermal characterization results in Section 3.3, it is concluded that the key thermal characteristics, such as exposure time, heating rate, and cooling rate, exhibit similar trends with respect to the AFSD processing parameters in Cu and Al-Mg-Si. These trends can be explained by linking the heat generation and thermal transfer processes to the tool head rotation rate and in-plane velocity in a qualitative manner. However, there is a salient, quantitative difference between Cu and Al-Mg-Si (as shown in Section 3.3.2): the peak temperature exhibits a different power law relationship with the processing parameters for each material system. Such a quantitative difference in peak temperature cannot be understood without delving into the material flow behavior, because the heat flow is fully coupled with material flow in AFSD.

3.4.1. Fundamentals of material flow and interface contact in AFSD

AFSD begins with a solid feed-rod (with a radius of R_0) that is in contact with the substrate but is not in contact with the bottom surface of the tool head. A compressive force is applied to the feed material as it rotates with the tool head (Fig. 3.6 (a)). With the heat generation at the material-substrate interface, the feed material raises temperature and extrudes underneath the tool head (Fig. 3.6 (b)). This involves a macroscopic material shape change via plastic deformation [54]. The new material is constrained vertically by the substrate and tool head, so it fills space with a thickness *h* pre-defined by the gap between the tool head and the substrate. The steady-state configuration is shown in Fig. 3.6 (c). For the transverse cross-section of the deposition track, the region directly below the feed-rod is referred to as the *transition zone* (radius of R_0), where the feed material

transitions from a compression-dominated state in the solid feed-rod to a shear-dominated state below the rotating tool head. The region vertically constrained by the tool head and the substrate is referred to as the *deposition zone*, which has a radius ranging from R_0 to R. The outer radius of the transition zone in AFSD is analogous to the pin edges in FSW. However, there is no sharp interface between the transition zone and the deposition zone in AFSD like that between the pin and workpieces in FSW, because the transition zone and deposition zones are occupied by the same material.

In the steady state of AFSD, heat can be generated by the interfacial friction caused by slipping of the tool head on the deposited material. The interfacial heat generation rate Q_δ is a function of the interfacial contact stress $\tau_{contact}$ and the velocity difference between the tool head and the top surface of the deposit. The latter can be written as $\Delta v\,(r) = r\Omega - (1-\delta)r\Omega = \delta(r)r\Omega$ [24], where $\delta(r)$ is the fractional slip and $\big(1-\delta(r)\big)$ is the sticking coefficient. The linear velocity of the tool head increases along the radial direction, and it is harder for the deposited material to keep the same rotation rate as the tool head. Thus, a the sticking coefficient should decrease with an increase of r, which is illustrated in Fig. 3.6 (d). In addition to slipping, it is possible to have the sticking condition dominate at the tool-material interface, especially at small r values [55]. This corresponds to the scenario where material in the deposition zone rotates together with the tool head, rendering a volume of material with intensive flow. The material velocity gradient in this volume results in shear deformation and plastic energy dissipation, with the corresponding volumetric heat generation rate Q_V depending on the shear strain rate and the shear stress at yielding [56].

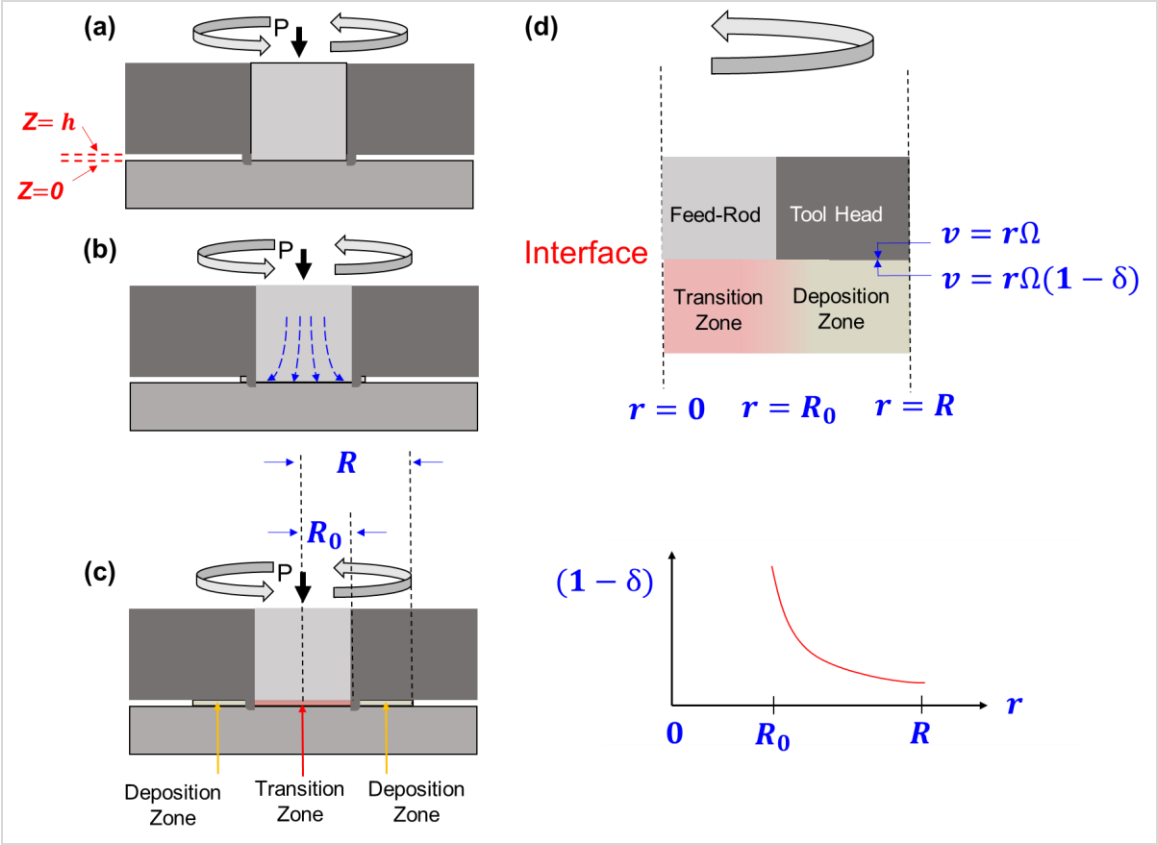

Figure 3.6. A schematic of the AFSD process: (a) The initial plunge phase, (b) material extrusion while rotating, and (c) the steady-state stage where the deposited material occupies the transition zone directly below the feed-rod and the deposition zone below the tool head. (d) An illustration of the interface region, considering the velocity of tool head and material as well as the sticking coefficient.

Overall, the heat generation in AFSD critically depends on the contact state at the tool-deposit interface and the volume of material flow. These two features are challenging to experimentally measure in FSW, because the stir zone in the workpieces is completely covered by the tool head. However, they can be explored via side-view monitoring in the AFSD configuration since the deposited material lies on top of the substrate.

3.4.2. Distinct material flow behaviors and contact states observed in Cu and Al-Mg-Si

To explore the material flow and tool-deposit contact state, monitoring of the leading edge of the deposit was performed using an optical camera and found drastically different behavior between AFSD of Cu and Al-Mg-Si. The first notable difference is the footprint of the deposition track. As illustrated in Figs. 3.7 (a) and (b), in Cu the deposited material does not significantly extend toward the leading direction. The leading edge of the Cu deposit is only slightly ahead of the leading edge of the feed-rod. In contrast, in Al-Mg-Si the deposited material extends significantly toward the leading direction. For Cu, in situ monitoring from the leading side can provide the material flow and rotation information inside the deposition zone—almost reaching the transition zone. For Al-Mg-Si, however, the monitoring can only capture the exterior surface of the deposition zone.

The second notable difference lies in the contact state of the tool-material interface in the deposition zone. Cu is found to remain effectively stationary after being extruded into the deposition zone, so the tool-material interface is characterized by a full slipping condition. In contrast, the exterior surface of Al-Mg-Si is seen to rotate with the tool head, although at a much lower rate, suggesting a partial slipping/sticking condition at the tool-material interface. Figs. 3.7 (c) and (d) show snapshots of the optical videos captured on the leading edge, wherein the flow paths of two distinct spots on the deposit surface (outlined in red) are investigated for each material system.

In Cu (Fig. 3.7 (c)), Spot M, which is below the tool head ($r \approx 1.5R_0$ but $\mathrm{r} < R$), remains effectively stationary and does not follow the motion of the tool head rotation. In other words, $\delta = 1$ and the sticking coefficient is 0. Spot N is inside the deposition zone

almost reaching the transition zone ($r \approx 1.1R_0$), and it is seen to move from the left to the far right in 0.13 seconds. Given the radius for the outer edge of motion and the time between the snapshot images, the linear velocity of Spot N measures as 90% of the tool head velocity at the same radius. In other words, for $r \approx 1.1R_0$, the sticking coefficient ($1 - \delta$) is 0.9 and $\delta = 0.1$. This observation shows that in Cu the material rotation and intensive flow are almost limited to the transition zone. At the boundary between the transition zone and deposition zone, the sticking coefficient rapidly drops from 0.9 to 0, and fractional slip rapidly increases from 0.1 to 1. In the snapshots of Al-Mg-Si shown in Fig. 3.7 (d), Speckle P and Q, which are both on the exterior surface of the deposition zone, move from left to right without observable changes in the relative distance over 1.51 seconds. The linear velocity of Spot P and Spot Q is measured as ~1% of the tool head velocity at the same radius. In other words, the sticking coefficient ($1 - \delta$) is 0.01 and $\delta = 0.99$. This observation suggests that material flow occurs throughout the entire deposit, from the transition zone to the edge of the deposition zone.

As shown in Fig. 3.6(d), a decrease of the sticking coefficient along the radial direction for *both* Cu and Al-Mg-Si. However, there is a significant difference between Cu and Al-Mg-Si based on the observation above:

- The sticking coefficient in Cu rapidly decreases to zero just outside of the transition zone, with a sharp transition of the material flow behavior across the boundary between the transition zone and deposition zone. Material rotation is almost absent in the deposition zone.

- The sticking coefficient in Al-Mg-Si shows a gradual decrease to non-zero values throughout the entire deposition zone ($R_0 < r < R$). The material rotation is observed even at the exterior surface of the deposition zone ($r = R$).

The evolution of the sticking coefficient along the radial direction observed in Cu and Al-Mg-Si is shown in Fig. 3.7 (e).

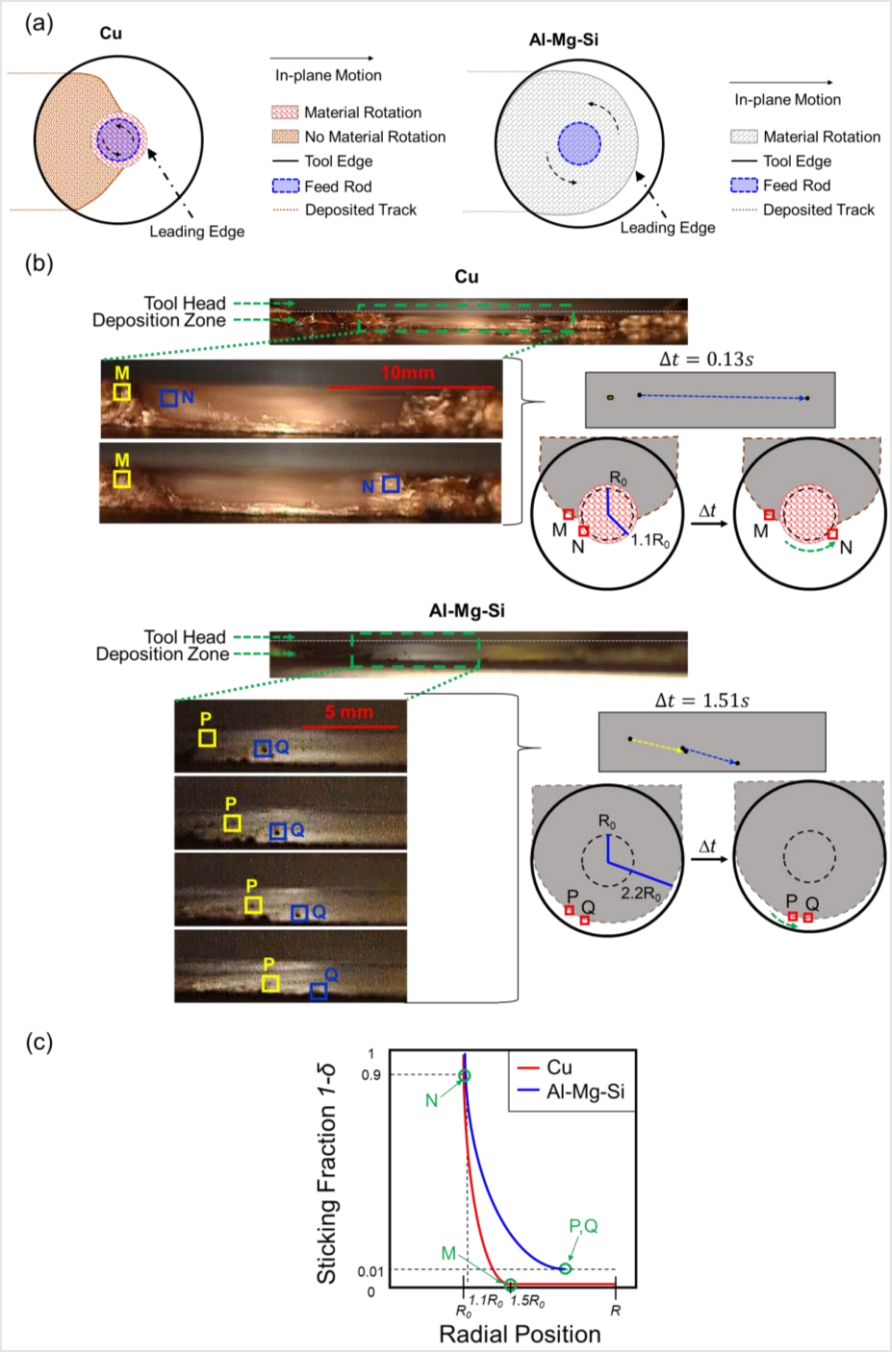

Figure 3.7. The observed material flow features with the deposition footprint of (a) Cu and (b) Al-Mg-Si compared. Video snapshots of material flow are compared for (c) Cu and (d) Al-Mg-Si at 300 RPM and 2 mm/s in-plane velocity. The Cu snapshots show two distinct regions where Point M remains stationary and Point N rotates with the tool head; the Al-Mg-Si snapshots show the rotation of the entire deposition zone. (e) A schematic showing the differences between Cu and Al-Mg-Si in the observed sticking coefficient as a function of the radial position.

Further insights into the material flow during AFSD can be gained by examining the flash forming at the edge of the deposition track, which shows visible differences between Cu and Al-Mg-Si. The top-view images in Figs. 3.8 (a) and (b) show that the Cu flash develops discrete, sharp edges but the Al-Mg-Si flash is indistinguishable from the rest of the deposit. From the video snapshots in Fig. 3.7 (also see *Supplemental Information)*, it is observed that the Cu flash begins to form as discontinuous sheets once the material enters the deposition zone. In the absence of material rotation, with more feed material extruded into the deposition zone, the previously formed discontinuous sheets are pushed outward toward the edge of the tool head. In contrast, in Al-Mg-Si the entire deposition zone ($R_0 \leq \mathrm{r} \leq R$) is observed to rotate with the tool head. As a result, the flash flows smoothly without geometric discontinuities. Such differences can be seen from the transverse cross-section images in Figs. 3.8 (c) and (d).

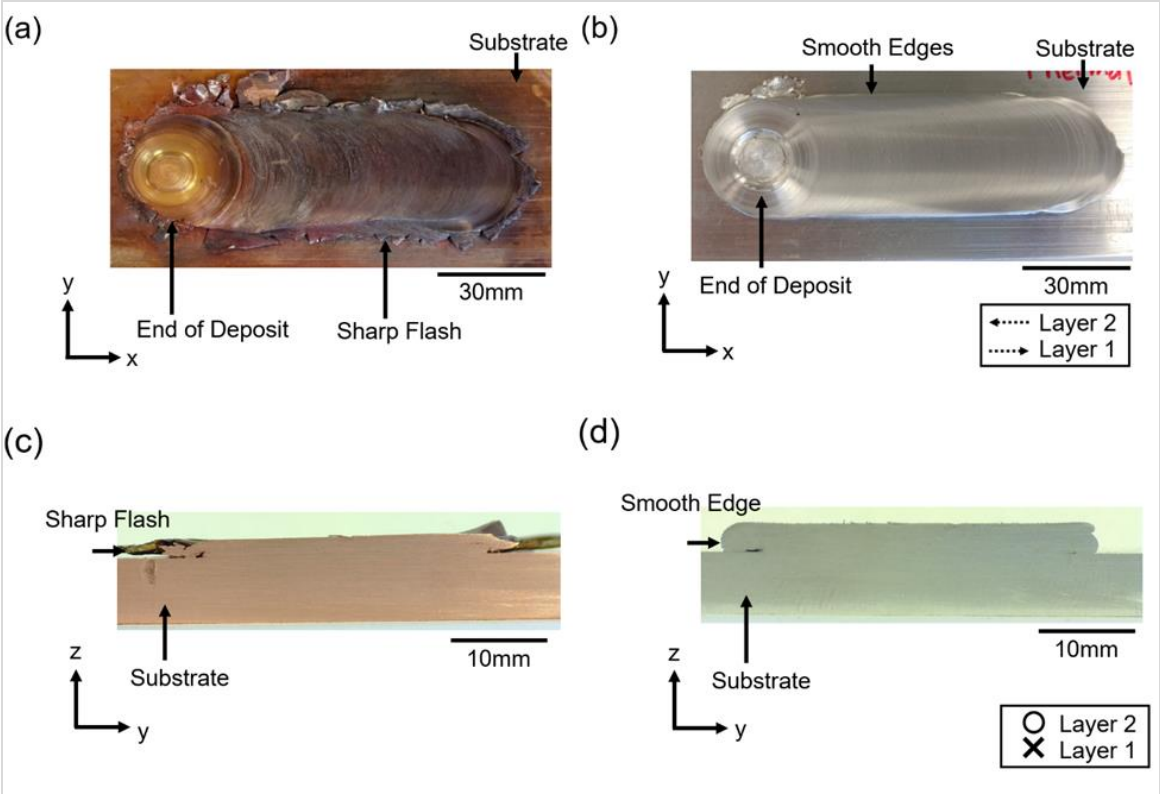

Figure 3.8. Pictures of the as-deposited tracks for (a) Cu and (b) Al-Mg-Si from a top-down view. (c) and (d) show the transverse cross-section of Cu and Al-Mg-Si, respectively. A key difference between the two material systems is seen in the shape and continuity of the flash.

3.5. Discussion

Section 3.3 discusses how the peak temperature T_{PEAK} is controlled by Ω/V during AFSD of Cu but by Ω^2/V in Al-Mg-Si. This suggests that for peak temperature control, the relative dominance of tool rotation rate Ω over in-plane velocity V is stronger in Al-Mg-Si than in Cu. Section 3.4 shows that the two materials have distinct interface contact states and material flow behaviors. This section discusses the correlation between the two aspects in Sections 3.3 and 3.4 with an attempt to link the interface contact and material flow to the heat generation mechanisms in Cu and Al-Mg-Si.

3.5.1. Heat generation mechanisms: Cu vs. Al-Mg-Si

In AFSD of Cu, the material rotation and intensive material flow are mostly observed within the transition zone ($r < R_0$) whereas the majority of the material in the deposition zone ($R_0 < r < R$) does not rotate with the tool head. As a result, the volumetric heat generation is almost limited within the transition zone. Regarding the contact state at the tool-material interface, the deposition zone in Cu is characterized by a full slipping condition as the material appears to be largely stationary. This leads to significant interfacial heat generation by friction. In AFSD of Al-Mg-Si, even the exterior surface is found to rotate, suggesting that the interaction with the tool head effectively drives the material flow in the deposition zone. Therefore, significant shear deformation could occur after Al-Mg-Si being extruded beneath the tool head, resulting in considerable volumetric heat generation. Since the deposition zone in Al-Mg-Si is found to rotate with the tool head but at a lower rotation rate (see Fig. 3.7), the contact state is characterized by a partial slipping/sticking condition [57].

Because the deposition zone of Cu is characterized by slipping at the interface and minimal material flow, interfacial friction is expected to be the dominant heat generation mechanism for the deposition zone. For Al-Mg-Si, both the interfacial friction and volumetric energy dissipation from plastic deformation are important heat generation mechanisms. The differences in the heat generation mechanisms between Cu and Al-Mg-Si are illustrated in Fig. 3.9, in which the interfacial heat generation is marked by blue arrows and the volume with significant volumetric heat generation is highlighted in red. Note that the color gradient of the figure corresponds to the differences in material flow and rotation, rather than the temperature distribution. While more intensive material flow

is expected in the transition zone, convection via material flow from the transition zone to the deposition zone could lead to higher temperatures in the deposition zone [58]. That being said, previous simulation works on FSW have predicted higher temperature in the center than the edge of the stir zone [24, 59]. Determining the temperature distribution inside the transition zone and deposition zone in AFSD is beyond the scope of this work and will require future experimental or simulation efforts.

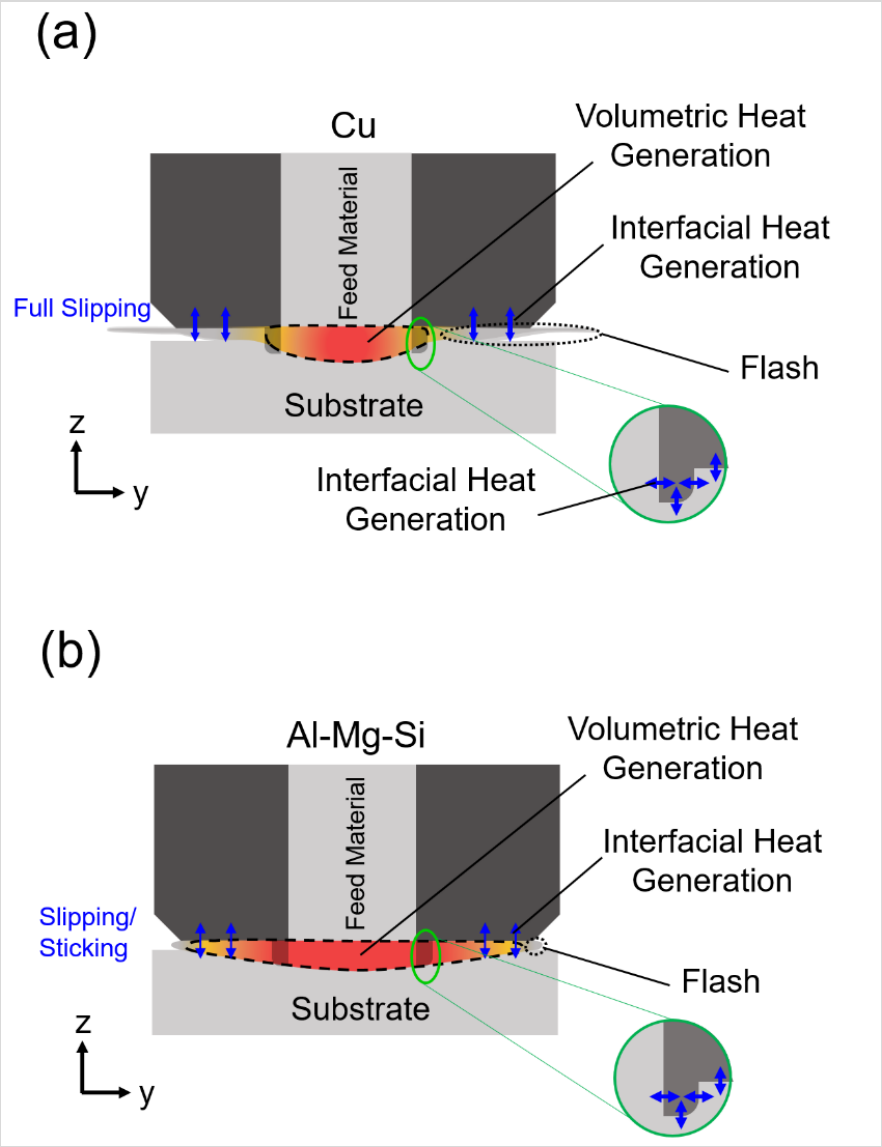

Figure 3.9. A diagram showing the heat generation mechanisms for (a) Cu and (b) Al-Mg-Si. The volumetric heat generation regions are shown in red and the interfacial friction is highlighted with blue arrows. The Cu system has the most significant volumetric heat generation directly beneath the feed-rod and the flash is large. In Al-Mg-Si, the volumetric heat generation zone is large due to substantial material flow.

In addition to the frictional heat and plastic deformation driven by the stick-slip interface at the tool bottom surface, heat is generated due to the presence of tool protrusions. In this work, the tool protrusions height is 1.5 mm and the layer thickness is 0.8 mm. As a result, a significant portion of the protrusion penetrates into the substrate. The tool protrusions interact with the deposited material as well as the substrate, resulting in (i) frictional heating at the associated interfaces and (ii) substantial material flow in the volume surrounding the protrusion path. Regarding the amount of heat generation, the surface area of the protrusions is small (~10 mm^2) compared to the bottom surface of the tool head (~1140 mm^2), so the interfacial heat generation contributed by the protrusions is expected to be small globally. However, they locally raise the temperature and drive the material flow in the surface layers of the substrate, and thus play an important role in quality control in AFSD.

3.5.2. Influences of the tool head rotation rate on the heat generation mechanisms

Generally, the interfacial heat generation rate can be written as $Q_\delta = \int \tau_{contact}\,(v_{tool} - v_{material})d\tilde{A} = \int \tau_{contact}\; r\Omega\delta d\tilde{A}$, where $\tau_{contact}$ is the interfacial shear stress and $d\tilde{A}$ is an infinitesimal interface area. The integration covers the *entire deposition zone*: $R_0 \le \mathrm{r} \le R$. In AFSD of Al-Mg-Si, the fractional slip δ and the sticking coefficient $(1-\delta)$ vary for different $\mathbf{r}$ values in the deposition zone, so $Q_\delta^{Al-Mg-Si} = \int \tau_{contact}\; r\Omega\delta(r)d\tilde{A}$. However, in AFSD of Cu, almost no material rotation is observed in the deposition zone, so δ is constant and $\delta = 1$. The heat generation equation thus reduces to $Q_\delta^{Cu} = \int \tau_{contact}\; r\Omega d\tilde{A}$. From these equations, the interfacial heat generation is expected to increase with the tool head rotation rate Ω in both Al-Mg-Si and

Cu due to the term $r\Omega$. However, there is an additional term $\delta(r)$ in $Q_{\delta}^{Al-Mg-Si}$, which also increases with the tool head rotation rate Ω. This is because an increase of Ω leads to an increase in the tool velocity, resulting in a decrease of the sticking coefficient and an increase of the fractional slip δ. Considering the appearance of Ω in both terms $r\Omega$ and $\delta(r,\Omega)$, it should have a more significant influence on the interfacial heat generation rate in Al-Mg-Si than in Cu.

The total volumetric heat generation rate can be written as $Q_V = \int \zeta\, \dot{\varepsilon}_{ij}^{p} \sigma_{ij} d\tilde{V}$. Here $\dot{\varepsilon}_{ij}^{p}$ and σ_{ij} are the components of the plastic strain rate tensor and the Cauchy stress tensor, the product of which defines the density of plastic energy dissipation [60]. ζ denotes the ratio of the heat converted from plastic deformation and ranges from 0.80 to 0.99 [61], $d\tilde{V}$ is an infinitesimal volume, and the integration covers the volume of material with intensive flow. For Cu, the total volume of intensive flow $\tilde{V}^{Flow}$ is almost the same as the volume of transition zone and is hardly influenced by the tool rotation rate. For Al-Mg-Si, $\tilde{V}^{Flow}$ is larger than the volume of transition zone, and likely increases with the tool rotation rate Ω as suggested by previous studies. In FSW of Al alloy 7020-T6, Lorrain *et al.* [62] have experimentally observed an increase of the stir zone size with the tool rotation rate increasing from 300 RPM to 600 RPM. Using the methodology of scaling, Mendez *et al.* [63] have analyzed the heat transfer and plastic deformation during FSW and predicted a positive correlation between the thickness of the shear layer (volume with intensive flow) and the tool rotation rate. With $\tilde{V}^{Flow}$ staying almost constant in Cu but increasing in Al-Mg-Si at a higher rotation rate, Ω should have a more significant influence on the volumetric heat generation rate in Al-Mg-Si than in Cu.

From these analyses, the tool head rotation rate should have more influences on the interfacial and volumetric heat generation rates in Al-Mg-Si than that in Cu for a given in-plane velocity. This is probably the origin of the different power laws of peak temperature between Cu and Al-Mg-Si, wherein the relative dominance of tool rate Ω over in-plane velocity V is found to be stronger in Al-Mg-Si than in Cu. Fundamentally, the drastically different contact states and material flow behaviors in Cu and Al-Mg-Si are related to stick-slip interactions with the tool head as well as their intrinsic thermomechanical properties. For solid materials, the sticking period between two surfaces is dependent on the kinetic friction coefficient between the interacting surfaces. Of particular importance here is the friction coefficients of the Fe-based tool and the deposited materials, Cu and Al. It is known that the kinetic friction coefficient between Cu:Fe is lower than Al:Fe [64, 65], which leads to a lack of sticking in the Cu to the rotating steel tool and a lower frictional shear stress [66]. Beyond that, Al-Mg-Si has better intrinsic forgeability with easier plastic flow than Cu [43]. Even with the same contact shear stress, more intensive material flow and rotation is expected in the deposition zone in Al-Mg-Si than in Cu.

3.6 Conclusions

In summary, this work characterized the temperature evolution and heat generation mechanisms during AFSD of Cu and Al-Mg-Si via in situ measurements of the thermal evolution and material flow. In addition to providing critical thermal data, this work has enabled quantification of the relationships between the AFSD processing conditions and key thermal characteristics, while providing physical insights into the differences in heat generation mechanisms between Cu and Al-Mg-Si. The most salient conclusions from this work include:

- T_{Peak} exhibits a power law relationship with Ω/V in Cu but with Ω^2/V in Al-Mg-Si.
- The exposure time, heating rate, and cooling rate for AFSD are approximately on the order of 10^1 s, 10^1 - 10^2 K/s, and 10^1 K/s, respectively. The exposure time increases with an increase of Ω or a decrease of V, the heating rate increases with an increase of V, and the cooling rate increases with a decrease of Ω or an increase of V.
- During AFSD of Cu, material rotation primarily occurs in the material beneath the rotating feed-rod. The interface between the tool head and deposited material is under a full slipping condition, and interfacial friction is the dominant heat generation mechanism in the deposition zone. During AFSD of Al-Mg-Si, the tool rotation causes the material in the deposition zone to rotate. The interfacial contact is under a partial slipping/sticking condition. Both interfacial friction and volumetric energy dissipation contribute to the heat generation in the deposition zone.

• The differences in the heat generation mechanisms between Cu and Al-Mg-Si, which result from the distinct material flow behaviors and interface contact states, are likely to be the origin of their different power laws of peak temperature.

3.7 Appendix 1. Substrate temperature evolution during AFSD

The IR camera provides important insight into the temperature distribution on the exterior surface of the deposited material. Complementary to that, the embedded thermocouples offer an accurate and reliable measurement of the substrate temperature directly beneath the deposited material. Fig. 2.10 shows the typical temperature evolution in Cu and Al-Mg-Si measured by thermocouples at positions A_{TC} and B_{TC}. The measured *T-t* plots are overlaid with the IR temperature measurements of the deposited material selected at spots A_{IR}, and B_{IR}, which correspond to the location directly above A_{TC} and B_{TC}, respectively. The exact locations of the measurement can be found in Fig. 2.1(b) in the main text.

The temperature evolution in the deposited material measured by IR imaging shows a sharper peak with a higher magnitude, a smaller exposure time, a higher heating rate, and a higher cooling rate compared to the temperature profile of the substrate measured by thermocouples. This is because the temperature measured by IR imaging results from the heat generation by tool-material interactions and possibly severe plastic deformation, whereas in the thermocouple data it is a result of the heat conduction from the deposited material into the substrate. Even before the arrival of the tool head at Point A_{IR}, Point A_{TC} in the substrate experiences a gradual pre-heating effect due to the material deposited (of elevated temperature) before Point A_{IR}. The preheating and gradual cooling from

conduction result in a broader temperature profile than Point A_{IR}. The temperature profiles for each spot are strongly site-specific. Locations far from the layer transition, such as Spot A_{TC} and A_{IR}, experience two distinct peaks with substantial cooling between layers, as seen in Figs. 2.10 (a) and (b). Spot B_{TC} and B_{IR} are much closer to the layer transition, so the two peaks from each layer deposition are seen to overlap (see Figs. 2.10 (c) and (d)).

The difference in the measured temperature at Spot A_{IR} and A_{TC} or Spot B_{IR} and B_{TC} allows us to roughly estimate the contribution of cooling mechanisms in AFSD. This work considers the heat flux by thermal conduction into the substrate, air convection, and radiation [43, 51, 52]. Heat flux by conduction can be estimated using Fourier's conduction law $\Phi_{conduction} = -\kappa \cdot {\Delta T}/{\Delta x}$, where κ is the thermal conductivity. ΔT is the difference in temperature between the deposited material (measured from the IR camera) and the substrate below it (measured from the embedded thermocouples), and Δx is the distance between the two measured locations. Using $\kappa = 401$ and 170 W/m·K for Cu and Al-Mg-Si respectively [66] as well as $\Delta x = 6.8 \times 10^{-3}$ m (dimension measured in our experiment), $\Phi_{conduction}$ is calculated to be on the order of 10^7 W/m^2 or above for both materials. Heat flux of convection can be estimated using Newton's law of cooling $\Phi_{convection} = -h \cdot (T - T_{environment})$. Here, h is the heat transfer coefficient of air assumed to be in the range of 10-100 W/m^2·K [65], T is the peak temperature measured by the IR camera, and $T_{environment}$ is the ambient temperature set to be 298K. With these numbers, $\Phi_{convection}$ is estimated to be ~ 10^3-10^4 W/m^2. The heat flux by radiation is $\Phi_{radiation} = \varepsilon\sigma(T^4 - T_{environment}^4)$, where the Stefan-Boltzmann constant σ= 5.67×10^{-8} W/m^2· K^4 and ε is the emissivity [66]. $\Phi_{radiation}$ is estimated to be ~ 10^4 W/m^2. Apparently, the heat flux by conduction is much more significant than that by air

convection and radiation. The total heat flow by each mechanism is a product of the heat flux and the cooling area. Considering the cooling area of each mechanism, the corresponding analysis concludes that conduction is the dominant cooling mechanism in AFSD for both Cu and Al-Mg-Si.

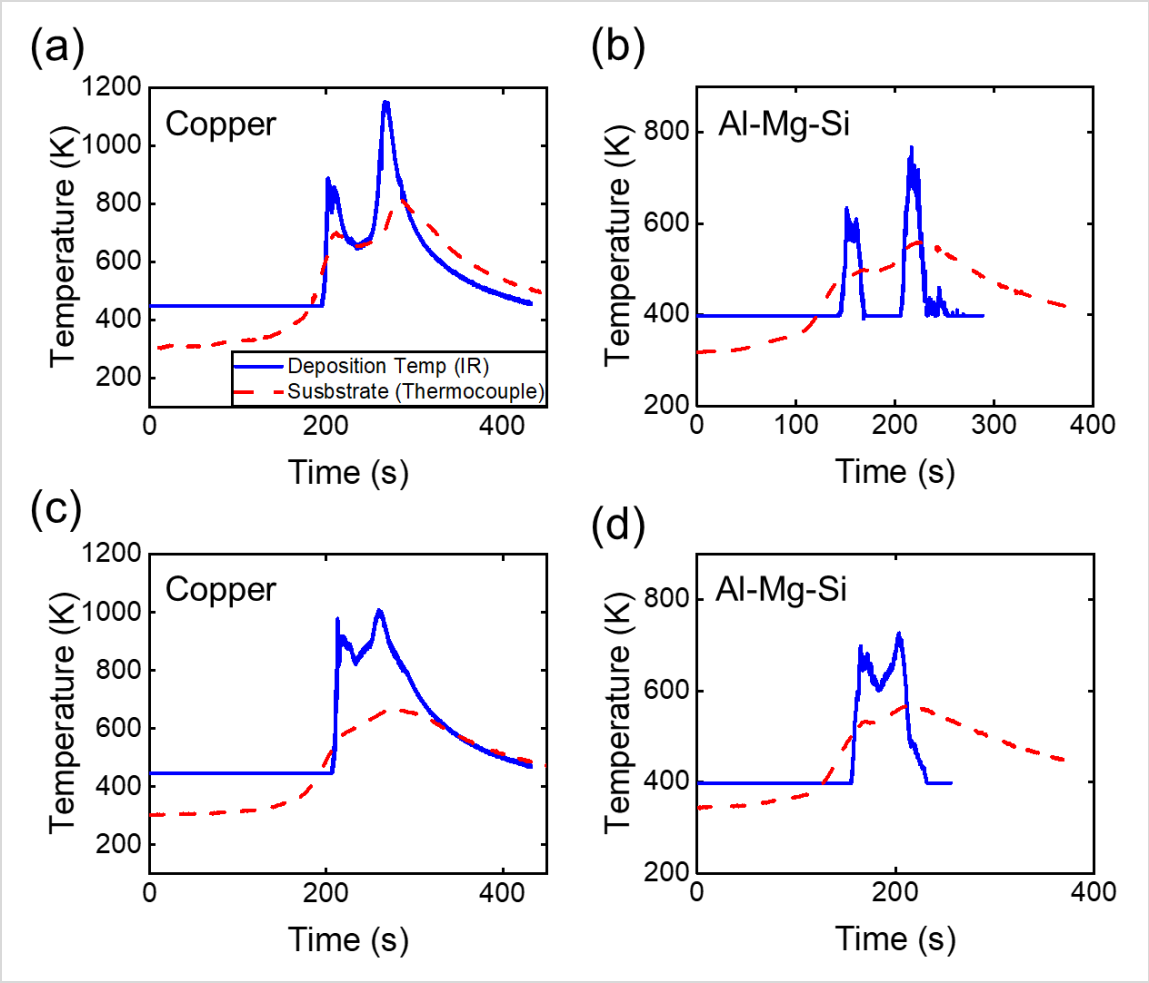

Figure 3.10. Temperature-time plots of spot A_{TC} and A_{IR} for (a) Cu at 300 RPM and 1 mm/s in-plane velocity (b) Al-Mg-Si at 300 RPM and 2 mm/s in-plane velocity. Plots (c) and (d) correspond to the temperature-time plots of B_{TC} and B_{IR} for Cu and Al-Mg-Si, respectively. In general, the temperature curve measured by the IR camera shows a narrower peak with greater magnitude than the corresponding temperature of the substrate.

3.8. Appendix 2. Non-dimensional analysis of the Arbegast relationship

The original form of the Arbegast relationship has constants K and a, where a is raising a dimensional quantity to a variable power. Thus, the units for the constant K are also variable based on the equipment and geometry used for fitting of this relationship. Here, a non-dimensional form of the Arbegast relationship is obtained by multiplying the parenthetical value by the circumference of the stir zone to determine more broadly applicable constants in the case of a heat index of Ω/V. For Cu, the dimensionless fitting constants are found as $K_{Cu} = 0.11$ and $a_{Cu} = -0.90$. For Al-Mg-Si, the dimensionless fitting constants are $K_{Al-Mg-Si} = 0.19$ and $a_{Al-Mg-Si} = -1.68$. The magnitude of the fitting parameters is scaled by this method, but this does not change the form of the relationship, thus the fitting accuracy is unaffected. This is reflected by the R-squared values that remain as 0.94 and 0.86 for Cu and Al-Mg-Si, respectively

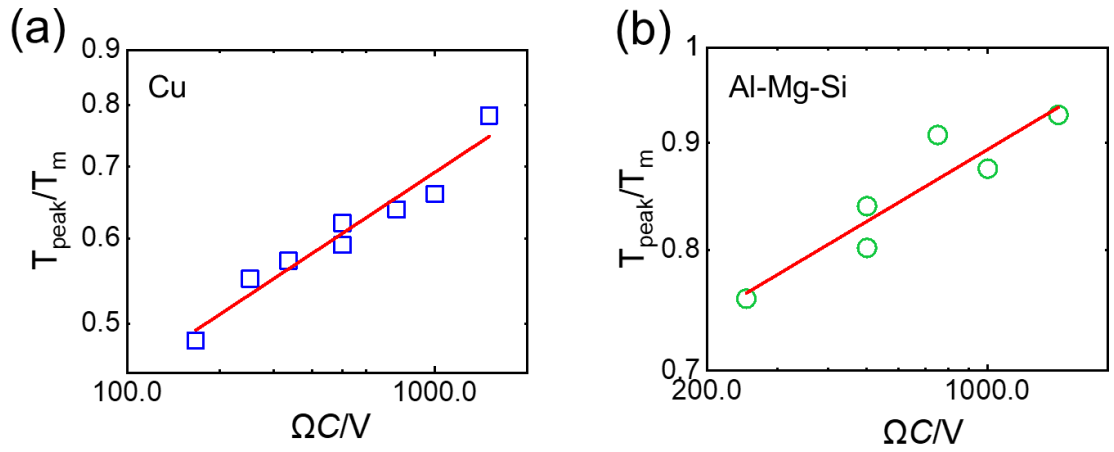

Figure 3.11. Fitting a power law relationship of the homologous peak temperature to the processing parameters with a relationship in the form of $\Omega C/V$. Units for Ω are (rev/s), C are (mm/rev), and V are (mm/s).

References

[1] Gibson, I., Rosen, D., Stucker, B., Directed Energy Deposition Processes, Additive Manufacturing Technologies: 3D Printing, Rapid Prototyping, and Direct Digital Manufacturing, Springer New York, New York, NY, 2015, pp. 245-268.

[2] Sames, W.J., List, F.A., Pannala, S., Dehoff, R.R., Babu, S.S., The metallurgy and processing science of metal additive manufacturing, International Materials Reviews 61(5) (2016) 315-360.

[3] Williams, S.W., Martina, F., Addison, A.C., Ding, J., Pardal, G., Colegrove, P., Wire + Arc Additive Manufacturing, Materials Science and Technology 32(7) (2016) 641-647.

[4] Li, W., Yang, K., Yin, S., Yang, X., Xu, Y., Lupoi, R., Solid-state additive manufacturing and repairing by cold spraying: A review, Journal of Materials Science & Technology 34(3) (2018) 440-457.

[5] Norfolk, M., Johnson, H., Solid-State Additive Manufacturing for Heat Exchangers, JOM 67(3) (2015) 655-659.

[6] Yu, H.Z., Jones, M.E., Brady, G.W., Griffiths, R.J., Garcia, D., Rauch, H.A., Cox, C.D., Hardwick, N., Non-beam-based metal additive manufacturing enabled by additive friction stir deposition, Scripta Materialia 153 (2018) 122-130.

[7] Padhy, G.K., Wu, C.S., Gao, S., Friction stir based welding and processing technologies - processes, parameters, microstructures and applications: A review, Journal of Materials Science & Technology 34(1) (2018) 1-38.

[8] Krüger, S., Wagner, G., Eifler, D., Ultrasonic Welding of Metal/Composite Joints, Advanced Engineering Materials 6 (2004) 157-159.

[9] Yin, S., Cavaliere, P., Aldwell, B., Jenkins, R., Liao, H., Li, W., Lupoi, R., Cold spray additive manufacturing and repair: Fundamentals and applications, Additive Manufacturing 21 (2018) 628-650.

[10] Rivera, O.G., Allison, P.G., Jordon, J.B., Rodriguez, O.L., Brewer, L.N., McClelland, Z., Whittington, W.R., Francis, D., Su, J., Martens, R.L., Hardwick, N., Microstructures and mechanical behavior of Inconel 625 fabricated by solid-state additive manufacturing, Materials Science and Engineering: A 694 (2017) 1-9.

[11] Khodabakhshi, F., Gerlich, A.P., Potentials and strategies of solid-state additive friction-stir manufacturing technology: A critical review, Journal of Manufacturing Processes 36 (2018) 77-92.

[12] Friel, R.J., Harris, R.A., Ultrasonic Additive Manufacturing – A Hybrid Production Process for Novel Functional Products, Procedia CIRP 6 (2013) 35-40.

[13] Sova, A., Grigoriev, S., Okunkova, A., Smurov, I., Potential of cold gas dynamic spray as additive manufacturing technology, The International Journal of Advanced Manufacturing Technology 69(9) (2013) 2269-2278.

[14] Besharati-Givi, M.K., Asadi, P., Advances in Friction-Stir Welding and Processing, Elsevier Science2014.

[15] Mishra, R.S., Ma, Z.Y., Friction stir welding and processing, Materials Science and Engineering: R: Reports 50(1) (2005) 1-78.

[16] Schultz, J.P., Creehan, K.D., Fabrication tools for exerting normal forces on feedstock, Aeroprobe Corporation, 2017.

[17] Garcia, D., Jones, M.E., Zhu, Y., Yu, H.Z., Mesoscale design of heterogeneous material systems in multi-material additive manufacturing, Journal of Materials Research 33(1) (2018) 58-67.

[18] Garcia, D., Wu, Z., Kim, J.Y., Yu, H.Z., Zhu, Y., Heterogeneous materials design in additive manufacturing: Model calibration and uncertainty-guided model selection, Additive Manufacturing 27 (2019) 61-71.

[19] Griffiths, R.J., Perry, M., Sietins, J., Zhu, Y., Hardwick, N., Cox, C.D., Rauch, H.A., Yu, H.Z., A Perspective on Solid-State Additive Manufacturing of Aluminum Matrix Composites Using MELD, Journal of Materials Engineering and Performance (2018).

[20] Yu, H.Z., Cross, S.R., Schuh, C.A., Mesostructure optimization in multi-material additive manufacturing: a theoretical perspective, Journal of Materials Science 52(8) (2017) 4288-4298.

[21] Phillips, B.J., Avery, D.Z., Liu, T., Rodriguez, O.L., Mason, C.J.T., Jordon, J.B., Brewer, L.N., Allison, P.G., Microstructure-deformation relationship of additive friction stir-deposition Al–Mg–Si, Materialia 7 (2019) 100387.

[22] Griffiths, R.J., Petersen, D.T., Garcia, D., Yu, H.Z., Additive Friction Stir-Enabled Solid-State Additive Manufacturing for the Repair of 7075 Aluminum Alloy, Applied Sciences 9 (2019) 3486.

[23] Song, M., Kovacevic, R., Numerical and experimental study of the heat transfer process in friction stir welding, Proceedings of the Institution of Mechanical Engineers, Part B: Journal of Engineering Manufacture 217(1) (2003) 73-85.

[24] Nandan, R., Roy, G.G., Lienert, T.J., Debroy, T., Three-dimensional heat and material flow during friction stir welding of mild steel, Acta Materialia 55(3) (2007) 883-895.

[25] Criales, L.E., Arısoy, Y.M., Lane, B., Moylan, S., Donmez, A., Özel, T., Laser powder bed fusion of nickel alloy 625: Experimental investigations of effects of process parameters on melt pool size and shape with spatter analysis, International Journal of Machine Tools and Manufacture 121 (2017) 22-36.

[26] Nie, P., Ojo, O.A., Li, Z., Numerical modeling of microstructure evolution during laser additive manufacturing of a nickel-based superalloy, Acta Materialia 77 (2014) 85-95.

[27] Thijs, L., Verhaeghe, F., Craeghs, T., Humbeeck, J.V., Kruth, J.-P., A study of the microstructural evolution during selective laser melting of Ti–6Al–4V, Acta Materialia 58(9) (2010) 3303-3312.

[28] Zinovieva, O., Zinoviev, A., Ploshikhin, V., Three-dimensional modeling of the microstructure evolution during metal additive manufacturing, Computational Materials Science 141 (2018) 207-220.

[29] Martin, J.H., Yahata, B.D., Hundley, J.M., Mayer, J.A., Schaedler, T.A., Pollock, T.M., 3D printing of high-strength aluminium alloys, Nature 549(7672) (2017) 365-369.

[30] Dehoff, R.R., Kirka, M.M., Sames, W.J., Bilheux, H., Tremsin, A.S., Lowe, L.E., Babu, S.S., Site specific control of crystallographic grain orientation through electron beam additive manufacturing, Materials Science and Technology 31(8) (2015) 931-938.

[31] Khandkar, M.Z.H., Khan, J., Reynolds, A.P., Prediction of temperature distribution and thermal history during friction stir welding: Input torque based model, 2003.

[32] Mishra, R.S., De, P.S., Kumar, N., Friction Stir Welding and Processing: Science and Engineering, Springer International Publishing2014.

[33] Hirsch, P.B., Warrington, D.H., The flow stress of aluminium and copper at high temperatures, The Philosophical Magazine: A Journal of Theoretical Experimental and Applied Physics 6(66) (1961) 735-768.

[34] Assidi, M., Fourment, L., Guerdoux, S., Nelson, T., Friction model for friction stir welding process simulation: Calibrations from welding experiments, International Journal of Machine Tools and Manufacture 50(2) (2010) 143-155.

[35] Swaminathan, S., Oh-Ishi, K., Zhilyaev, A.P., Fuller, C.B., London, B., Mahoney, M.W., McNelley, T.R., Peak Stir Zone Temperatures during Friction Stir Processing, Metallurgical and Materials Transactions A 41(3) (2010) 631-640.

[36] Woo, W., Feng, Z., Wang, X.L., Brown, D.W., Clausen, B., An, K., Choo, H., Hubbard, C.R., David, S.A., In situ neutron diffraction measurements of temperature and stresses during friction stir welding of 6061-T6 aluminium alloy, Science and Technology of Welding and Joining 12(4) (2007) 298-303.

[37] Fehrenbacher, A., Schmale, J.R., Zinn, M.R., Pfefferkorn, F.E., Measurement of Tool-Workpiece Interface Temperature Distribution in Friction Stir Welding, Journal of Manufacturing Science and Engineering 136(2) (2014) 021009-021009-8.

[38] Gerlich, A., Avramovic-Cingara, G., North, T.H., Stir zone microstructure and strain rate during Al 7075-T6 friction stir spot welding, Metallurgical and Materials Transactions A 37(9) (2006) 2773-2786.

[39] Everton, S.K., Hirsch, M., Stravroulakis, P., Leach, R.K., Clare, A.T., Review of in-situ process monitoring and in-situ metrology for metal additive manufacturing, Materials & Design 95 (2016) 431-445.

[40] Kriczky, D.A., Irwin, J., Reutzel, E.W., Michaleris, P., Nassar, A.R., Craig, J., 3D spatial reconstruction of thermal characteristics in directed energy deposition through optical thermal imaging, Journal of Materials Processing Technology 221 (2015) 172-186.

[41] Aboulkhair, N.T., Simonelli, M., Parry, L., Ashcroft, I., Tuck, C., Hague, R., 3D printing of Aluminium alloys: Additive Manufacturing of Aluminium alloys using selective laser melting, Progress in Materials Science 106 (2019) 100578.

[42] Frigola, P., Harrysson, O., Horn, T.J., West, H., Aman, R., Rigsbee, J.M., Ramirez, D.A., Murr, L., Medina, F., Wicker, R.B., Rodriguez, E., Fabricating Copper Components with Electron Beam Melting, Advanced Materials and Processes 172 (2014) 20-24.

[43] Verlinden, B., Driver, J., Samajdar, I., Doherty, R.D., Thermo-Mechanical Processing of Metallic Materials, Pergamon Materials Series, Pergamon2007, pp. 233-332.

[44] Holland, S.D., Reusser, R.S., Material Evaluation by Infrared Thermography, Annual Review of Materials Research 46(1) (2016) 287-303.

[45] Song, M., Kovacevic, R., Thermal modeling of friction stir welding in a moving coordinate system and its validation, International Journal of Machine Tools and Manufacture 43(6) (2003) 605-615.

[46] Miller, T.J., Zinkle, S.J., Chin, B.A., Strength and fatigue of dispersion-strengthened copper, Journal of Nuclear Materials 179-181 (1991) 263-266.

[47] Muraca, R.F., Whittick, J.S., Materials data handbook: Aluminum alloy 6061, 1972.

[48] Mironov, S., Inagaki, K., Sato, Y.S., Kokawa, H., Microstructural evolution of pure copper during friction-stir welding, Philosophical Magazine 95(4) (2015) 367-381.

[49] Aval, H.J., Serajzadeh, S., Kokabi, A.H., Theoretical and experimental investigation into friction stir welding of AA 5086, The International Journal of Advanced Manufacturing Technology 52(5) (2011) 531-544.

[50] Commin, L., Dumont, M., Masse, J.E., Barrallier, L., Friction stir welding of AZ31 magnesium alloy rolled sheets: Influence of processing parameters, Acta Materialia 57(2) (2009) 326-334.

[51] Manvatkar, V., De, A., Svensson, L.E., DebRoy, T., Cooling rates and peak temperatures during friction stir welding of a high-carbon steel, Scripta Materialia 94 (2015) 36-39.

[52] Sato, Y.S., Kokawa, H., Enomoto, M., Jogan, S., Microstructural evolution of 6063 aluminum during friction-stir welding, Metallurgical and Materials Transactions A 30(9) (1999) 2429-2437.

[53] Arbegast, W.J., Modeling friction stir joining as a metal working process, TMS Annual Meeting, San Diego, CA, 2003, pp. 313-327.

[54] Imada, K., Takayanagi, M., Plastic Deformation of High Density Polyethylene in Solid State Extrusion, International Journal of Polymeric Materials and Polymeric Biomaterials 2(2) (1973) 89-104.

[55] Chen, G., Shi, Q., Feng, Z., On the Material Behavior at Tool/Workpiece Interface During Friction Stir Welding: A CFD Based Numerical Study, in: R.S. Mishra, M.W. Mahoney, Y. Sato, Y. Hovanski (Eds.), Friction Stir Welding and Processing VIII, Springer International Publishing, Cham, 2016, pp. 251-258.

[56] Colegrove, P.A., 3 Dimensional Flow and Thermal Modelling of the Friction Stir Welding Process, University of Adelaide, Department of Mechanical Engineering2001.

[57] Schmidt, H., Hattel, J., Modelling heat flow around tool probe in friction stir welding, Science and Technology of Welding and Joining 10(2) (2005) 176-186.

[58] Liu, F.C., Nelson, T.W., Grain structure evolution, grain boundary sliding and material flow resistance in friction welding of Alloy 718, Materials Science and Engineering: A 710 (2018) 280-288.

[59] Chen, G., Feng, Z., Zhu, Y., Shi, Q., An Alternative Frictional Boundary Condition for Computational Fluid Dynamics Simulation of Friction Stir Welding, Journal of Materials Engineering and Performance 25(9) (2016) 4016-4023.

[60] Simar, A., Bréchet, Y., de Meester, B., Denquin, A., Gallais, C., Pardoen, T., Integrated modeling of friction stir welding of 6xxx series Al alloys: Process, microstructure and properties, Progress in Materials Science 57(1) (2012) 95-183.

[61] Rosakis, P., Rosakis, A.J., Ravichandran, G., Hodowany, J., A thermodynamic internal variable model for the partition of plastic work into heat and stored energy in metals, Journal of the Mechanics and Physics of Solids 48(3) (2000) 581-607.

[62] Lorrain, O., Favier, V., Zahrouni, H., Lawrjaniec, D., Understanding the material flow path of friction stir welding process using unthreaded tools, Journal of Materials Processing Technology 210(4) (2010) 603-609.

[63] Mendez, P.F., Tello, K.E., Lienert, T.J., Scaling of coupled heat transfer and plastic deformation around the pin in friction stir welding, Acta Materialia 58(18) (2010) 6012-6026.

[64] Nuruzzaman, D.M., Chowdhury, M.A., Friction Coefficient and Wear Rate of Copper and Aluminum Sliding against Mild Steel International Transaction Journal of Engineering, Management, & Applied Sciences & Technologies 4(1) (2012) 29-40.

[65] Rumble, J.R., CRC Handbook of Chemistry and Physics, 100 ed., CRC Press/Taylor & Francis, Boca Raton, FL, 2019.

[66] Cverna, F., Committee, A.S.M.I.M.P.D., ASM Ready Reference: Thermal properties of metals, ASM International2002.

Chapter 4

Investigation into the Force and Torque Evolution during Additive Friction Stir Deposition

4.0. Abstract

Additive friction stir deposition (AFSD) is a metal additive manufacturing technology that leverages the fundamental physical principles of friction stir and a material extrusion mechanism to fabricate near net-shape components. For friction stir techniques, it is well established that the forces during processing are highly indicative of the final part quality and the bonding strength. Compared to the more traditional friction stir techniques, AFSD has distinct mechanical boundary conditions: no mechanical constraints exist in the plane of deposition except for previously deposited material and the out-of-plane constraint provided by the tool is a reactionary force rather than an applied force. This work presents the first *in situ* investigation into the evolution of the compressive force F_z and torque M_z for AFSD at a variety of equipment processing parameters (tool rotation rate Ω and in-plane velocity V) for Cu and Al-Mg-Si. For both material systems, F_z is found to have a positive correlation with V and an inverse correlation with Ω. For Al-Mg-Si, similar trends are found for M_z, however the M_z in Cu systems shows no relationship to the processing

parameters. This is attributed to the tool-material contact state which takes the form of partial sticking condition for Al-Mg-Si and full slipping in the bulk of the deposition zone for Cu. Finally, the sub-grain morphology of the Al-Mg-Si system is characterized and used to predict the flow stress during processing. The flow stress shows a strong correlation to the torque M_z during processing which further suggests that the partial sticking condition leads to substantial induced shear in the deposition zone for Al-Mg-Si.

4.1 Introduction

Additive friction stir deposition (AFSD) is a solid-state metal additive manufacturing process that enables site-specific build-up of three-dimensional components through frictional heating and material extrusion [1]. Consumable rod feedstock is pushed through a non-consumable rotating tool where frictional heating leads to local softening and mixing of the feedstock and substrate materials. Movement of the tool and feed stock material enables gradual build-up of full-scale parts where complex geometries can be deposited in a layer-by-layer fashion. AFSD leads to several benefits compared to melt-based additive manufacturing and other solid-state additive processes: i) refined, equiaxed microstructure with isotropic mechanical properties [2], ii) reduced thermal gradients and low residual stresses [3], iii) achieves near-net shaping without subtractive machining [1], iv) no need for post-processing heat treatment to reduce porosity or improve mechanical properties [4, 5], and v) enables fabrication of composites and dissimilar materials [6].

AFSD shares many physical principles with established friction stir techniques such as friction stir welding (FSW) [7, 8], friction stir processing (FSP) [9, 10], and friction stir additive manufacturing (FSAM) [11], but AFSD stands out as the only site-specific

material accumulation technique. The key processing parameters for these techniques are the tool velocity V and the tool rotation rate Ω. These parameters determine the local processing conditions which includes not only the thermal history components such as heat generation rate and total heat input [3, 12] but also includes the coupled mechanical histories such as the strain and strain rates [13] experienced by the material. For AFSD, there has been preliminary investigation of how the processing conditions affect the local material flow [14], thermal history [3], local microstructure [15], and final properties [5, 16] of as-manufactured parts but there has been no investigation of the stress states at the tool-material interface as there has been for FSW. Du *et al* investigated the conditions that lead to a high frequency of voids using a Bayesian neural network and found that peak temperature and shear stress are the most influential parameters for void formation in aluminum alloys [17]. Long *et al* demonstrated a strong correlation between the tool rotation rate, welding torque, and grain size for several aluminum alloys and approximated the strain and strain rates experienced by the material [18]. Crawford *et al* found that conditions with a low Ω/V ratio led to formation of wormhole defects due to lack of plasticization and conditions with a high Ω/V ratio can lead to local distortion due to surface overheating in AA 6061 [19]. Additionally, the force and torque experienced by the tool during processing may be detrimental to the tool durability as demonstrated by Buchibabu et al [20]. It is evident from the FSW literature that an understanding of the material stress state and mechanical deformation history is key in determining the microstructure, quality, and properties of parts produced via AFSD. Furthermore, the distinct boundary conditions for AFSD, necessitate an in-depth investigation as the local

boundary conditions may lead to unique stress states compared to other friction stir processes.

Figure 4.1 shows a schematic of (a) friction stir welding and (b) additive friction stir deposition. Here, the key differences in the applied boundary forces for the the tow processes can be observed. In FSW the key forces applied are F_z the normal force applied by the tool to the surface of the material, and M_z the shear force imparted into the base material that is determined by the tool rotation rate, the sticking coefficient, and the normal force. F_x and F_y are reactionary forces that develop from material drag and the mechanical constraints as the tool moves across build plate. In AFSD the in-plane forces are generated by the same mechanisms as in FSW, but the mechanical constraints are notably different. In the traverse direction F_x has no mechanical constraint along the leading edge but is constrained by the deposited material on the trailing edge. F_y has no constraint in either direction. Furthermore, F_z is the normal force directly applied to the material being extruded into the deposition zone. The force applied by the tool shoulder F_T is a reactionary force that depends on the material flow during mixing and the spacing between the tool head and the substrate.

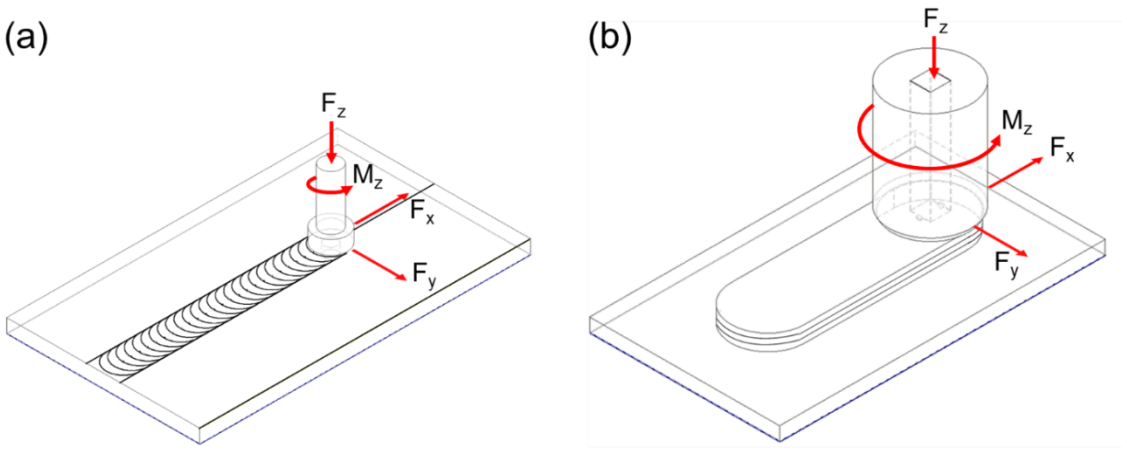

Figure 4.1. A schematic of (a) FSW and (b) AFSD showing the distinct forces during these friction stir techniques.

4.2. Experimental Method

4.2.1. Material Deposition

Deposits for this work were performed using a MELD – R2 system (MELD Manufacturing Corporation, Christiansburg VA, USA). The system was equipped with a 38 mm wide tool steel head with two surface protrusions on opposite ends of the feed-rod exit hole. The two surface features were semi-circular in shape and had a height of 1.5 mm. Each experiment consisted of a stack of two deposited layers with single-layer thickness of ~1.65 mm and a nominal length of ~70 mm. Layers were printed continuously, such that the traverse directions for each layer were in opposite directions and the end of layer one corresponds to the start of layer two. Two different material systems were studied in this experiment: 1) Cu-110 (commercially pure), and 2) a commercially available Al-Mg-Si alloy (i.e., AA 6061). The feed-rod material was square rod with a side length of 9.5 mm. The substrate was machined from rolled plate into 6.35 ×76.2 × 127 mm sections. The substrate and the deposited material had the same composition for each respective material

system. Deposits were performed at systematically varied processing conditions that included variations in rotation rate and in-plane velocity. Material feed rate can also be varied, however the ratio between the material feed rate and the tool in-plane velocity can have significant effects on surface quality; it was kept constant at a value of 1:3 which is typical of high-quality deposits using the given tool geometry. Tool rotation rates Ω were distributed across the viable processing range at 300 RPM, 600 RPM, and 900 RPM, and the selected in-plane tool velocities V include 1.00 mm/s, 2.00 mm/s, and 3.00 mm/s.

4.2.2. Force and Torque Measurement

In-line measurement of the normal force and the torque are built in to the MELD – R2 system. During deposition, the compressive force imposed onto the feed-rod material from the linear feed apparatus was measured by a strain-based load cell. The torque at the tool head is indirectly measured by an ABB ACS-880 spindle drive. The current applied to the motor is measured and then converted into a torque value based on the motor characteristics and the gear ratio of 1.775 between the motor and tool. The measured torque to freely run the tool head was measured at 10 RPM increments up to 990 RPM and subtracted out from all torque measurements.

4.2.3. Microstructure Characterization

Samples were prepared for microstructure characterization via standard mechanical grinding and polishing using sand paper of 240, 320, 400, 600, and 1000 grit followed by a 1-micron diamond suspension and colloidal silica. Microstructure imaging was performed using a Helios Nanolab 600 DualBeam SEM (FEI company, Waltham, MA, USA) equipped with a Hikari EBSD detector. EBSD scan data analysis and alignment were performed using TSL OIM Analysis. The images generated from the scan data included inverse pole figure (IPF) maps and kernel average misorientation (KAM) maps. Grain size was determined using the size average method. A similar approach was applied to the KAM maps in accordance with ASTM E112 to determine the average sub-grain size of the material post deformation.

4.3. Results

4.3.1. General Phases of AFSD

Several distinct phases of deposition can be described based on the input operating conditions and the associated stress state of the tool and material. Fig. 4.2 shows the typical force vs. time plots during deposition of Al-Mg-Si and Cu. Prior to deposition, the feed-rod and tool head rotate together at a rapid rate. There is contact at the feed material-substrate interface, but no applied normal force other than gravity. Once the tool and feed material are up to speed, the tool is moved to the appropriate layer height such that the surface protrusions are plunged into the substrate surface (*I*), but no force is applied to the feed-rod. A baseline torque is measured due to the interaction of the tool protrusions with the substrate surface. This is the tool plunge phase and is analogous to the plunge of FSW,

but at a reduced scale given the small size of the tool protrusions (~1 mm) compared to the pin (~5 mm diameter). The next stage (*II*) is the feed-material plunge phase which is described by elastic deformation of the feed-rod under uniaxial compression where the input stress can be approximated by the change in the beam length $F_Z \sim \Delta L$. Here, heat is generated by a slipping dominated contact state at the feed-rod substrate interface where the generated heat is directly proportional to F_Z. Frictional heating softens the feed-rod and substrate at the contact interface until both materials begin to yield (*III*). As soon as the feed material begins to yield and enter the deposition zone underneath the tool shoulder, a combination of yielding at elevated temperatures and shearing at the tool-material interface lead to a drop-off in F_Z. The torque gradually rises as material fills the space beneath the tool surface and the interaction volume increases. At this point, the in-plane motion phase is initiated (*IV*). The start of the in-plane motion phase requires an increase in the material feed rate to reach the 1:3 material feed rate to in-plane velocity ratio. After a few moments, F_Z reaches a relatively stable value denoted as the steady-state force (*V*) with only minor oscillations in magnitude. Once a layer is finished, the layer transition (*VI*) creates a large drop in F_Z and M_Z as the tool assembly is moved away from the substrate by the desired layer height. A gradual return to steady-state conditions occurs and a second layer of material is deposited. At the end of deposition, the tool raises, and the feed material breaks from the deposit, resulting in a final drop of the measured compressive force and torque.

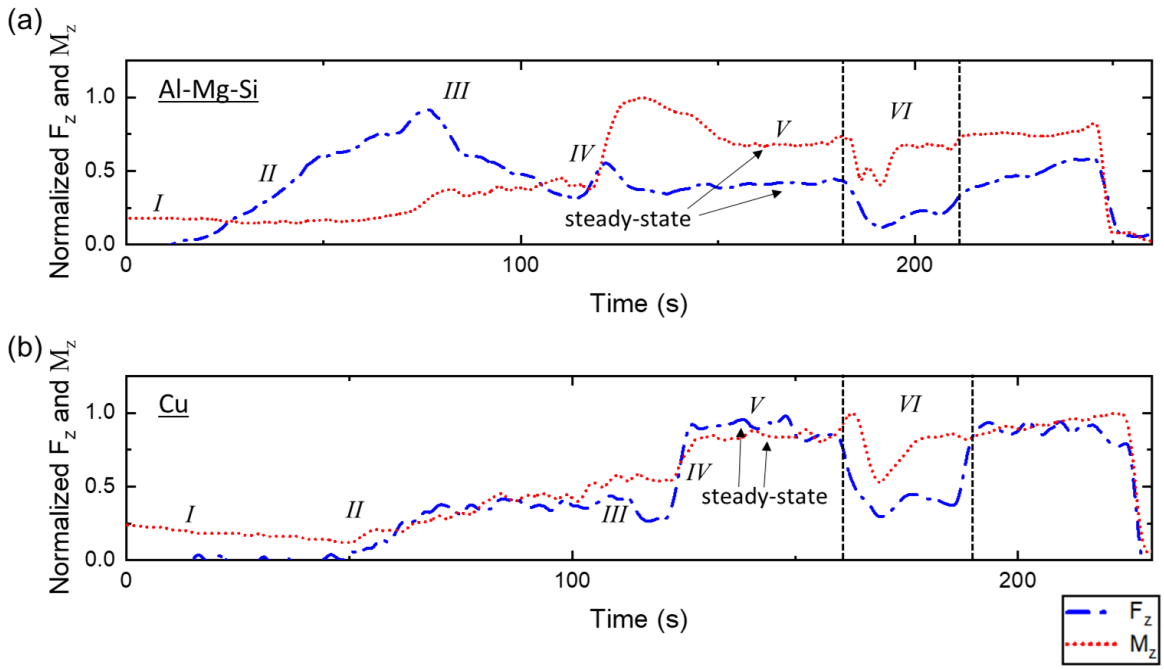

Figure 4.2. A Schematic showing representative plots of the normal force and torque for (a) Al-Mg-Si and (b) Cu. Roman numerals correspond different stages of operation for AFSD including the tool plunge, the material plunge, the material feed, steady state traverse and layer transition phases.

It is noted that the peak force observed during the plunge phase (*III*) for Al-Mg-Si is higher than the steady-state force (*V*) required during deposition. In Cu, the opposite trend is observed – the steady-state force (*V*) is higher than the peak plunge force (*III*). The key difference between these two phases with regards to the operating conditions is that the in-plane motion phase (*IV*) requires an increase in the material feed rate compared to the initial plunge phase (*II*). There are several factors that may contribute to this phenomenon. Cu has been observed to have a very low sticking coefficient in the bulk of the deposition zone during AFSD, so the stress-state is more akin to a forging or extrusion process. The deformation during all stages is primarily driven by the normal force applied to the feed material as opposed to shearing at the tool-material interface. For Cu, the yield stress at low temperatures is generally lower than Al-Mg-Si which leads to small peak in

the plunge force. The increase in material feed-rate may lead to strain hardening of the Cu feed-material thus a higher required force for steady-state deposition. In Al-Mg-Si the increase in feed-rate also increases the strain rate and a small peak in force is observed, however, the interaction volume and thus the heat generation via plastic deformation under the tool may increase to offset this change in the compression state. The torque trends for both materials are fairly similar between both Cu and Al-Mg-Si with the onset of torque rise for Cu occurring at a relatively low F_z due to the lower yield strength.

4.3.2. Trends in Steady-state Force and Torque Evolution

Figs. 3.3 (a) and (b) show the measured steady-state compressive stress at various processing conditions. Note that the normal stress applied in AFSD is the force directly to the feed material and not applied by the tool head. For both Cu and Al-Mg-Si, the steady-state compressive force decreases with an increase of Ω or a decrease of V. This suggests an inverse correlation with the expected peak temperature trends. The yield strength of both material systems decreases at higher temperatures. A higher Ω at a constant V corresponds to a higher heat generation rate for a constant exposure time leading to increased thermal softening. A decrease of V at a constant Ω, provides more time for frictional heat generation thus increasing the total amount of input energy.

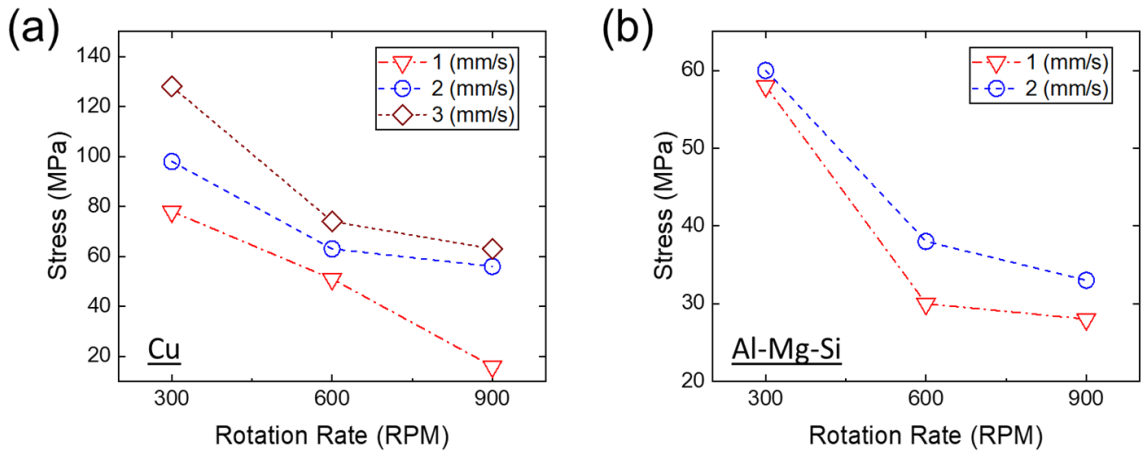

Figure 4.3. A plot of the compressive stress applied to the feed-rod for (a) Cu and (b) Al-Mg-Si at various processing conditions.

Fig. 4.4. (a) and (b) shows the measured steady-state torque at various processing conditions. For Al-Mg-Si, the steady-state torque decreases with an increase of Ω or a decrease of V. Similar to the compressive stress, this trend is consistent with the previously described temperature trends as the flow stress is expected to decrease at higher temperatures. In Cu however, there is little influence of the equipment processing variables on the shear stress during deposition. This is attributed to the pure slipping condition observed in the majority of the processing zone. Although the material is still expected to soften at elevated temperatures, there is little interaction between the tool surface and the deposited material. Therefore, the torque is primarily dependent on the interaction between the tool surface protrusions, the substrate, and a small volume of material that makes up the transition zone.

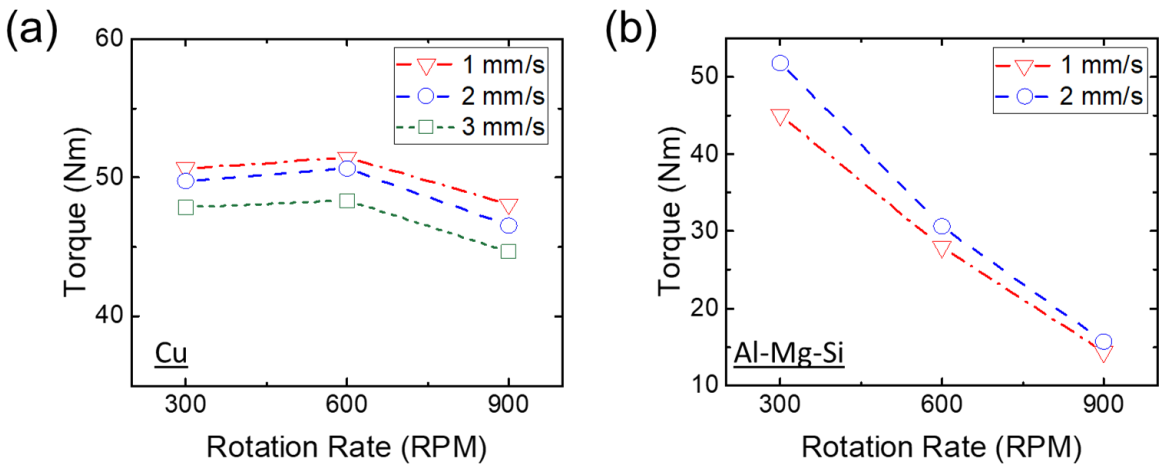

Figure 4.4. A plot of the torque input by the tool at different equipment processing parameters for (a) Cu and (b) Al-Mg-Si

Trends for the force and torque variation with respect to the processing conditions were quantitatively analyzed by an empirical fitting of $Y = A(X_1)^p(X_2)^q$, where Y corresponds to the output process parameter (normal force or torque), X_1 and X_2 are the input process parameters, A, p, and q are fitting constants [21]. Fitting was performed using the MATLAB Curve Fitting Toolbox. Units for each variable are F_z(N), M_z(Nm), Ω(RPM), and V(m/min). Eq. 1 – 4 show the fitting coefficients for F_z and M_z for Al-Mg-Si and Cu. R-squared values are 0.948, 0.938, 0.965, and 0.601 for Eq. 1 – 4, respectively.

$$F_z(Al\text{-}Mg\text{-}Si) = 303300\ (\Omega)^{-0.65}\ (V)^{0.15} \quad (1)$$

$$F_z(Cu) = 1437000\ (\Omega)^{-0.72}\ (V)^{0.49} \quad (2)$$

$$M_z(Al\text{-}Mg\text{-}Si) = 13630\ (\Omega)^{-0.92}\ (V)^{0.18} \quad (3)$$

$$M_z(Cu) = 58.52\ (\Omega)^{-0.05}\ (V)^{-0.05} \quad (4)$$

For both material systems, F_z has a positive correlation to the in-plane velocity, V, and an inverse correlation to the tool rotation rate, Ω. An increase in V leads to reduced total heat input and tool interaction time. In turn, this reduces the expected peak temperature and subsequent thermal softening if the feed material. For Al-Mg-Si, similar trends are found where M_z is positively correlated to the in-plane velocity, V, and inversely correlated with the tool rotation rate, Ω. For M_z in Cu the fitting coefficients suggest an inverse correlation to both V and Ω, but the fitting is very poor given an R-squared value of 0.601. Furthermore, the value of the coefficients is an order of magnitude smaller than any of the other fitting coefficients, suggesting that neither processing parameter has a significant influence on the measured torque at the tool-material interface. This stems from the differences in the stick-slip behavior observed for Cu and Al-Mg-Si during AFSD and will be described Section 4.4.

4.3.4. Energy Efficiency of AFSD Process

Solid-state processes generally have increased power efficiency and lower energy requirements than melting based techniques. The energy efficiency of the AFSD process is estimated by comparing the input energy based on measured rotational power [12], Q_ω, to the energy input based on the measured temperature change [22], $Q_{\Delta T}$. The rotational power is described by $P_\omega = \tau\omega$ where τ is the applied torque in N·m and ω is the tool angular rotation speed in rad/s. This is then converted to an energy input based on the approximated interaction time of the deposit with the tool head, $t = \frac{D}{V}$ where t is the interaction time, D is the tool diameter, and V is the in-plane velocity. The product of $P_\omega t$ gives the total rotational energy input Q_ω. The energy input into the system can also be

approximated using the heat energy equation $Q_{\Delta T} = mC\Delta T$ where m is mass of the deposit, C is the heat capacity of the material, and ΔT is the difference between the peak measured temperature and room temperature. Material and geometric constants used for calculation of these values can be found in Table 4.1. The ratio of the heat energy to the rotational energy provides the efficiency of the AFSD process for these two material systems and can be seen in Fig. 4.5. The average power efficiencies are 30% and 36% for Cu and Al-Mg-Si, respectively.

Table 4.1: Parameters used for efficiency calculation

Parameter	Value	Units
Tool Diameter	0.038	m
Stir Height	0.00762	m
Heat Capacity – Al [23]	900	J/kg°C
Density – Al [23]	2700	kg/m^3
Heat Capacity – Cu [23]	385	J/kg°C
Density – Cu [23]	8950	kg/m^3

Qualitatively, the Cu system has a consistent trend amongst all processing conditions which corresponds to a consistent power efficiency. Al-Mg-Si shows much more scatter, particularly with respect to the heat energy. A key limitation of this efficiency calculation is that the heat energy calculations assume a constant volume for the stir zone and also ignore the presence of any local thermal gradients. Generally, it is expected that the size of the stir zone increases with increasing Ω and decreasing V [24]. Additionally, the rotational energy Q_ω for Al-Mg-Si has competing variables with an increase in the tool

rotation rate. An increase in ω leads to a direct increase in Q_ω, but also a decrease in the required torque τ since there is increased thermal softening. In the case of Cu, τ is relatively constant amongst the processing conditions whereas ω still provides a proportional increase in the rotational energy. Ultimately this relates back to the stick-slip condition at the tool interface which is defined by partial sticking for Al-Mg-Si and full slipping for Cu [3].

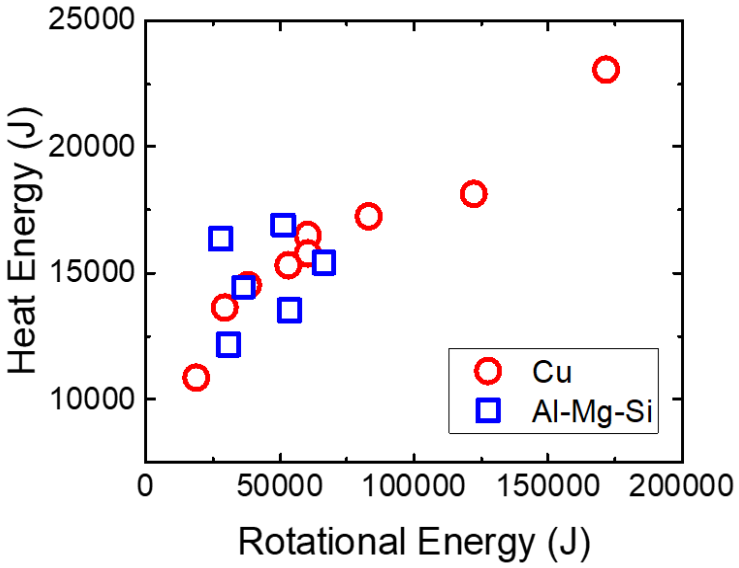

Figure 4.5. A plot comparing the rotational energy calculated from experimental torque measurements and the heat energy expected from the measured peak temperature.

4.3.5. Microstructure Characterization for Al-Mg-Si

The final microstructure of the material can be telling of the deformation and temperature experienced during a thermomechanical process. EBSD imaging was performed on the Al-Mg-Si samples and the inverse pole figure (IPF) maps are shown in Fig. 4.6. The grain size trends and grain boundary misorientation trends coincide previously established trends [25]. In general, an increase in grain size is observed with increasing Ω. Decreasing the tool travel velocity has an inverse effect on the temperature which can have a substantial effect on the precipitate structure thus the strains and strain rates during processing. Furthermore, this is indicative of different degrees of continuous dynamic recrystallization which has been observed to take place in AFSD.

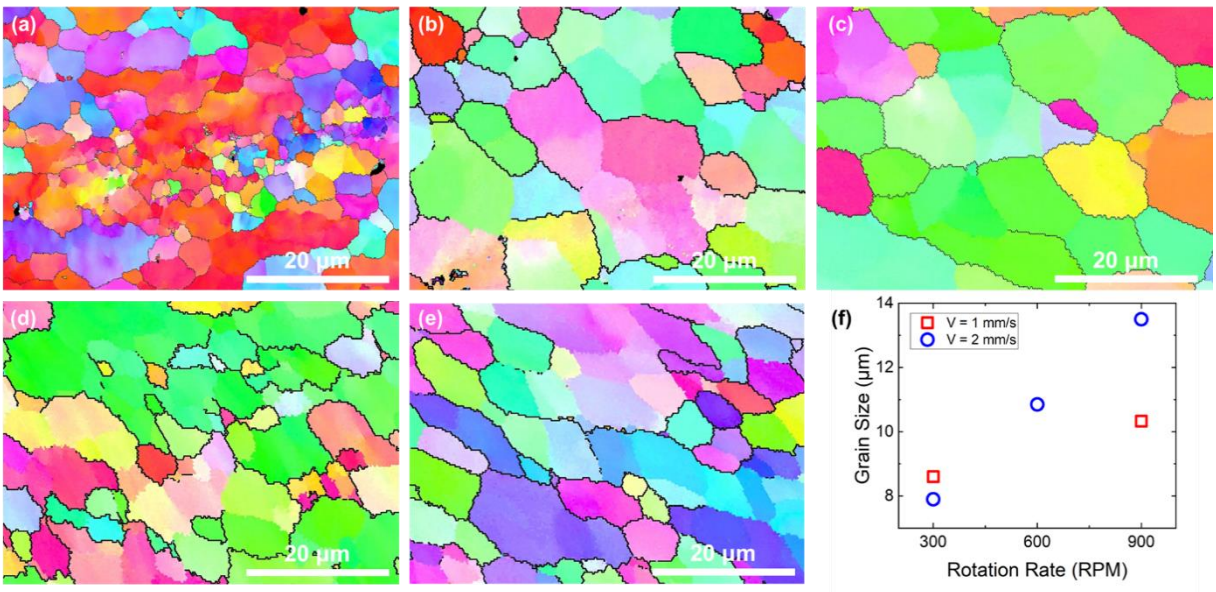

Figure 4.6. Inverse Pole Figure Maps of samples manufactured at (a) 300RPM and 2 mm/s in-plane velocity, (b) 600RPM and 2 mm/s in-plane velocity, (c) 900RPM and 2 mm/s in-plane velocity, (d) 300RPM and 1 mm/s in-plane velocity, (e) 900RPM and 1mm/s in-plane velocity, and (f) a plot of the grain size vs the processing parameters.

4.4. Discussion

4.4.1 Force Evolution at different Processing Temperatures

Figure 4.7 shows the (a) steady-state stress applied to the feed material and (b) the torque applied at the tool plotted along with the corresponding peak temperatures measured during deposition. The normal stress trend for both materials correlates well with thermal softening whereby the yield strength required to plasticize the material decreases at elevated temperatures. For Al-Mg-Si, the torque follows a similar trend with high temperature leading to reduced torque. Similar to the normal stress, the flow stress is expected to decrease with increasing temperature. For Cu, the torque does not follow any clear trend, which matches the empirical fitting that showed no dependence on processing parameters.

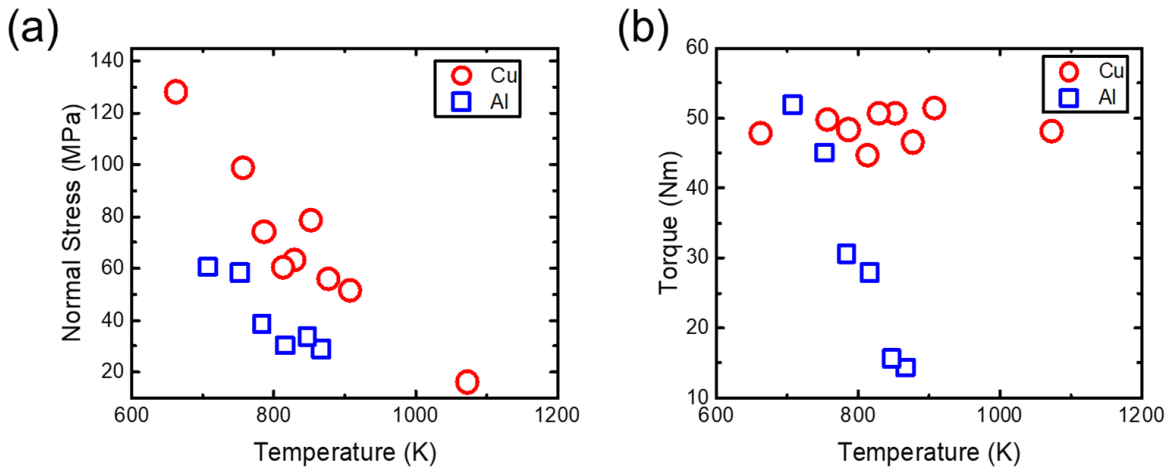

Figure 4.7. Plots of the (a) normal compressive stress and (b) the torque at the corresponding processing temperature for Cu and Al-Mg-Si

The key difference between the two material systems is the distinct contact states observed in the deposition zone, which critically depend on the slipping coefficient δ and sticking coefficient $(1-\delta)$. Fig. 4.8 shows the key differences ascertained from optical monitoring of the material flow. For Cu, there is a very high sticking fraction $\delta \ll 1$ in a small volume that surrounds the original feed-rod diameter. The bulk of the deposition zone is in a full slipping condition, $\delta = 1$. For Al-Mg-Si the bulk of the deposition zone is observed to be in a partial-sticking condition $0 < \delta < 1$. The measured torque at the tool interface should take the form of $M_z = \int \overrightarrow{r_A} \times (\overrightarrow{\tau_t} dA)$ where r_A is the position vector of the area with respect to the tool and τ_t is the contact shear stress. This torque is commonly represented by an empirical combination of the Tresca and the Coulomb friction $\tau_t = \left[(1-\delta)\tau_{flow} + \delta\mu_f P\right]$ where τ_{flow} is the shear flow stress at a given position, μ_f is the dynamic friction coefficient between the tool and working material, and P is the normal force applied by the material [26]. For the case of Cu, $\delta = 1$ in the bulk of the deposition zone so the torque at the interface simplifies to $\tau_t = \mu_f P$. For AFSD, $P = F_T$ which is a reactionary force at the tool-deposit interface rather than an applied force. Since there is only one in-plane mechanical constraint on the trailing edge, the value of F_T is expected to be relatively constant as material should flow preferentially outward towards the longitudinal or transverse directions. For Al-Mg-Si, the sticking fraction $(1-\delta)$ should be inversely proportional the tool rotation rate Ω and τ should vary based on the flow stress at the given temperature. This is consistent with the observed trends for the torque at different temperatures in Fig. 4.7.

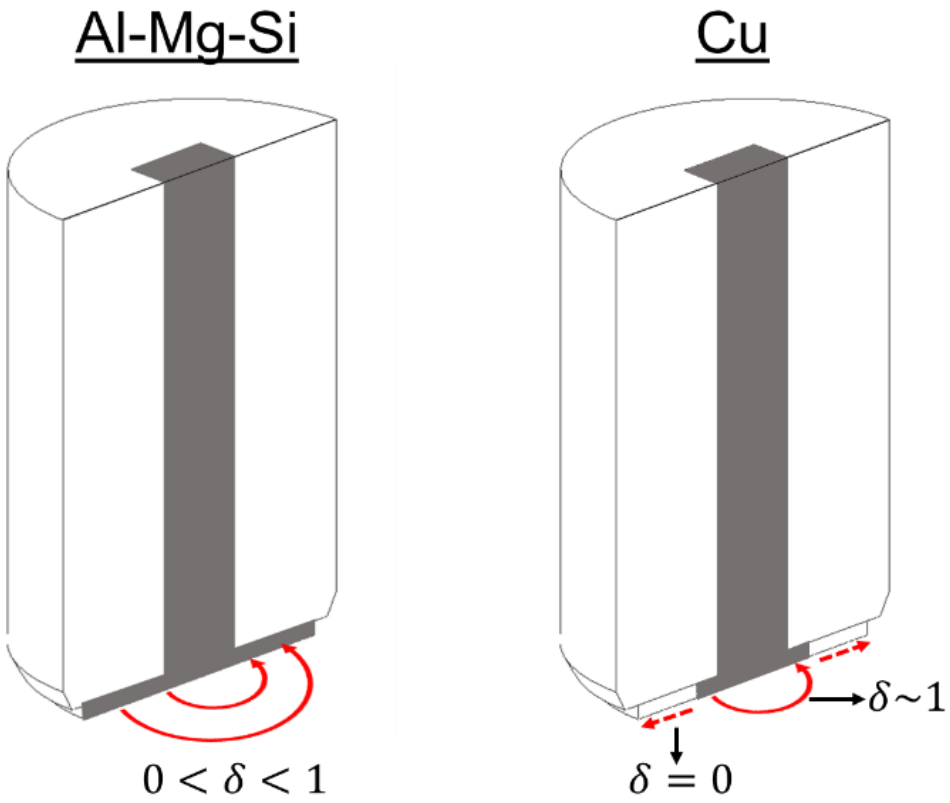

Figure 4.8. A cross-section schematic of the tool shoulder showing the contact state in the deposition zone for Al-Mg-Si and Cu. For Al-Mg-Si there is a partial sticking-slipping condition in the bulk of the deposition zone. For Cu, there is a slipping condition in the bulk of the deposition zone and full sticking in the region near the transition zone.

4.4.2. Sub-grain Size Characterization and Flow Stress Trends in Al-Mg-Si

Since AFSD is a non-equilibrium process it becomes challenging to directly relate the microstructure to the processing conditions. Here, a combined approach that uses the collected process monitoring data and post-process characterization enables additional characterization of the process-structure relationship. The sub-grain size (D) can be directly related to the flow stress (σ) during processing via the Derby relationship $\frac{\sigma}{G}\frac{D}{b} = K$ where G is the shear modulus, b is the magnitude of the Burgers vector and K is a constant with

magnitude 10 for FCC metals [27]. The sub-grain size is characterized by looking at the KAM obtained during EBSD imaging and quantified in accordance with ASTM E112 using the Hilliard single-circle intercept procedure [28]. This procedure was repeated with two different circumference circles and an example is shown in Fig 3.9(a). A temperature dependent shear modulus was calculated based on $G = \frac{E}{2(1+\nu)}$ where the temperature dependent modulus was defined as in Fig. 4.9(b). The temperature dependence of the Burgers vector and Poisson's ratio is ignored for these calculations as the variation is small relative to the shear modulus and sub-grain size variations.

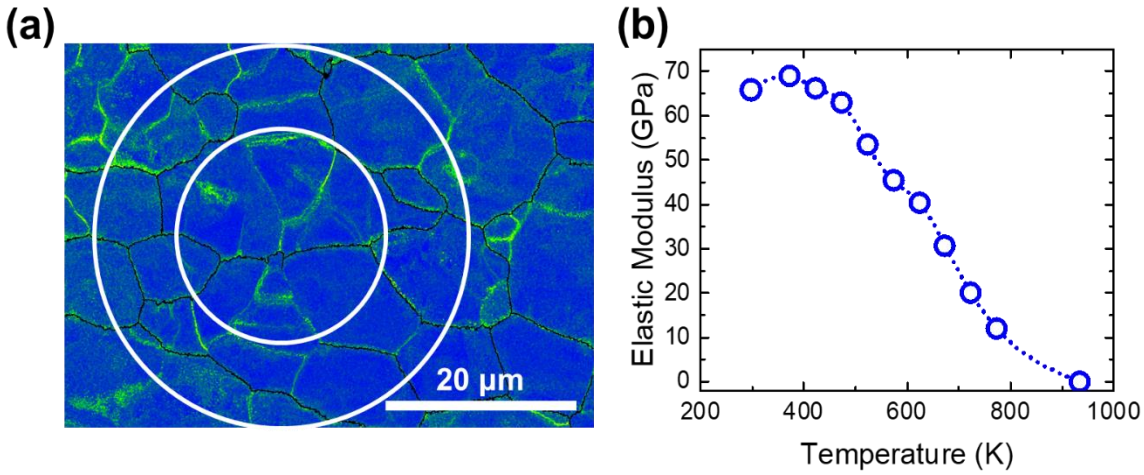

Figure 4.9. (a) A demonstration of the Hilliard single-circle intercept procedure for characterization of sub-grain size and (b) a plot of the elastic modulus vs temperature used to calculate the temperature dependent shear modulus [29].

From the sub-grain size measurements and the temperature dependent modulus, the flow stress during deposition is obtained and plotted amongst the various processing conditions (Fig 4.10a). The flow stress is inversely correlated to conditions with higher peak processing temperatures, as higher temperatures lead to additional thermal softening. The average contact shear stress is calculated from the torque via $M_z = \int \overrightarrow{r_A} \times (\overrightarrow{\tau_t} dA)$ and plotted along the shear flow stress as shown in Fig. 4.10b. The contact shear stress is found to exhibit a linear relationship with the flow stress of the form $\tau_{\text{flow}} = 1.8\tau_{\text{t}} + 1.6$ with an R-squared value of 0.92. This form of the relationship is not consistent with the linear combination of the Tresca and Coulomb friction forces discussed in Section 4.4.1 and would suggest a constant sticking coefficient greater than one and a constant normal force. The physical meaning behind this relationship is being explored through additional modeling efforts. The direct relationship between contact shear stress and flow shear stress further suggests that the tool contact state is in a partial-sticking slipping condition. The high agreement in trend between the torque and flow stress suggests that the shear force at the tool-material interface has a significant contribution to both the flow-stress during processing and the final microstructure post-processing. Additionally, the sub-grain size relationship to the flow-stress also suggests that continuous dynamic recrystallization is the primary restoration mechanism for Al-Mg-Si systems, although it is unclear if an equilibrium grain size is attainable within this process window.

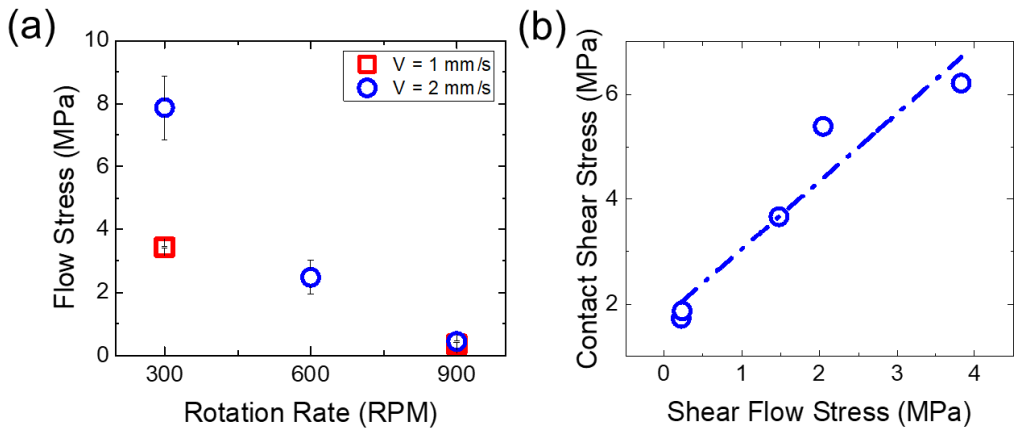

Figure 4.10. A plot of (a) the flow stress at various processing conditions and (b) the contact shear stress vs the flow stress for Al-Mg-Si. There is a strong correlation between the contact shear stress and shear flow stress suggesting that the flow stress is driven by the partial sticking condition at the tool-material interface. Error bars for flow stress are propagated from the standard deviation of sub-grain size measurement.

4.4.3 Force Evolution of AFSD compared to FSW

A schematic plot of the typical normal force observed in AFSD and FSW is shown in Fig. 4.11 [24]. While the shape of the curves for AFSD of Al-Mg-Si follows a similar trend to that of FSW, the exact mechanisms are not identical. In the case of F_z for FSW, the force corresponds to the normal force applied by the tool to the substrates and the is an initial peak in force corresponds to the tool plunge phase. For AFSD, F_z describes the force applied directly to the feed-rod material and the tool-plunge phase has almost no influence on F_z. This is a result of the small size of the surface protrusions and the shallow penetration into the substrate. However, the material plunge phase has a similar spike to the tool plunge for FSW, as the material undergoes uniaxial compression with gradual heating until yielding.

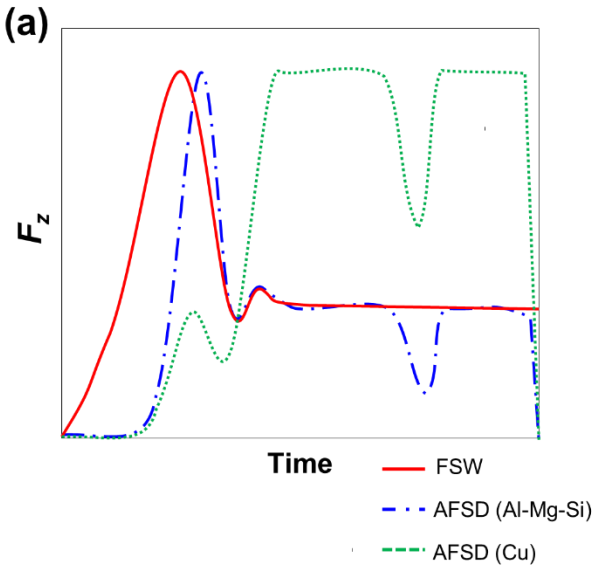

Figure 4.11. A schematic of the force evolution for FSW compared to AFSD of Al-Mg-Si and Cu.

4.5. Conclusions

This work characterized the force evolution for Cu and Al-Mg-Si during the additive friction stir deposition process through *in situ* measurement of the normal force applied to the feed-rod and the torque measured at the tool-material interface. Quantitative relationships between the equipment processing parameters and the stresses were established with key differences in the torque relationships being explained by the contact state at the tool-material interface. The most prominent conclusions of this work are bulleted below:

- The initial spike in normal force in AFSD corresponds to the initial heating and macroscopic shape change of the feed-rod as opposed to a tool plunge phase in FSW. For Al-Mg-Si the normal force during this macroscopic shape change

corresponds to the peak force during deposition. For Cu, the peak force during deposition occurs during the steady-state deposition regime.

- F_z exhibits a positive correlation with V and is inversely correlated to Ω for both Cu and Al-Mg-Si. For Cu, the power associated with each variable is comparable in magnitude whereas for Al-Mg-Si the Ω has power value several times larger than V.
- M_z exhibits a positive correlation with V and is inversely correlated to Ω only in the case of Al-Mg-Si. In Cu, the torque is independent of the processing parameters. This is related to the contact state at the tool-material interface whereby the Cu is in a full slipping condition and the torque equation simplifies to two constants: the dynamic friction coefficient μ_f and the normal force applied by the tool F_T.
- Sub-grain size characterization of the Al-Mg-Si samples enables estimation of the flow stress during processing. The flow stress is found to be proportional to the torque measured at the tool which further suggests a partial-sticking condition since the shear force induced by the tool has a strong correlation with the deformation state during processing.

References

[1] Yu, H.Z., Jones, M.E., Brady, G.W., Griffiths, R.J., Garcia, D., Rauch, H.A., Cox, C.D., Hardwick, N., Non-beam-based metal additive manufacturing enabled by additive friction stir deposition, Scripta Materialia 153 (2018) 122-130.

[2] Griffiths, R.J., Petersen, D.T., Garcia, D., Yu, H.Z., Additive Friction Stir-Enabled Solid-State Additive Manufacturing for the Repair of 7075 Aluminum Alloy, Applied Sciences 9 (2019) 3486.

[3] Garcia, D., Hartley, W.D., Rauch, H.A., Griffiths, R.J., Wang, R., Kong, Z.J., Zhu, Y., Yu, H.Z., In situ investigation into temperature evolution and heat generation during additive friction stir deposition: A comparative study of Cu and Al-Mg-Si, Additive Manufacturing 34 (2020) 101386.

[4] Rivera, O.G., Allison, P.G., Brewer, L.N., Rodriguez, O.L., Jordon, J.B., Liu, T., Whittington, W.R., Martens, R.L., McClelland, Z., Mason, C.J.T., Garcia, L., Su, J.Q., Hardwick, N., Influence of texture and grain refinement on the mechanical behavior of AA2219 fabricated by high shear solid state material deposition, Materials Science and Engineering: A 724 (2018) 547-558.

[5] Rutherford, B.A., Avery, D.Z., Phillips, B.J., Rao, H.M., Doherty, K.J., Allison, P.G., Brewer, L.N., Jordon, J.B., Effect of Thermomechanical Processing on Fatigue Behavior in Solid-State Additive Manufacturing of Al-Mg-Si Alloy, Metals 10(7) (2020) 947.

[6] Griffiths, R.J., Perry, M., Sietins, J., Zhu, Y., Hardwick, N., Cox, C.D., Rauch, H.A., Yu, H.Z., A Perspective on Solid-State Additive Manufacturing of Aluminum Matrix Composites Using MELD, Journal of Materials Engineering and Performance (2018).

[7] Mishra, R.S., Ma, Z.Y., Friction stir welding and processing, Materials Science and Engineering: R: Reports 50(1) (2005) 1-78.

[8] Threadgill, P.L., Leonard, A.J., Shercliff, H.R., Withers, P.J., Friction stir welding of aluminium alloys, International Materials Reviews 54(2) (2009) 49-93.

[9] Besharati-Givi, M.K., Asadi, P., Advances in Friction-Stir Welding and Processing, Elsevier Science2014.

[10] Padhy, G.K., Wu, C.S., Gao, S., Friction stir based welding and processing technologies - processes, parameters, microstructures and applications: A review, Journal of Materials Science & Technology 34(1) (2018) 1-38.

[11] Palanivel, S., Sidhar, H., Mishra, R.S., Friction Stir Additive Manufacturing: Route to High Structural Performance, JOM 67(3) (2015) 616-621.

[12] Schmidt, H., Hattel, J., Wert, J., An analytical model for the heat generation in friction stir welding, Modelling and Simulation in Materials Science and Engineering 12(1) (2003) 143-157.

[13] Gerlich, A., Avramovic-Cingara, G., North, T.H., Stir zone microstructure and strain rate during Al 7075-T6 friction stir spot welding, Metallurgical and Materials Transactions A 37(9) (2006) 2773-2786.

[14] Perry, M.E.J., Griffiths, R.J., Garcia, D., Sietins, J.M., Zhu, Y., Yu, H.Z., Morphological and microstructural investigation of the non-planar interface formed in solid-state metal additive manufacturing by additive friction stir deposition, Additive Manufacturing 35 (2020) 101293.

[15] Xu, N., Ueji, R., Fujii, H., Dynamic and static change of grain size and texture of copper during friction stir welding, Journal of Materials Processing Technology 232 (2016) 90-99.

[16] Yoder, J.K., Griffiths, R.J., Yu, H.Z., Deformation-based additive manufacturing of 7075 aluminum with wrought-like mechanical properties, Materials & Design (2020) 109288.

[17] Du, Y., Mukherjee, T., DebRoy, T., Conditions for void formation in friction stir welding from machine learning, npj Computational Materials 5(1) (2019) 68.

[18] Long, T., Tang, W., Reynolds, A.P., Process response parameter relationships in aluminium alloy friction stir welds, Science and Technology of Welding and Joining 12(4) (2007) 311-317.

[19] Crawford, R., Cook, G.E., Strauss, A.M., Hartman, D.A., Stremler, M.A., Experimental defect analysis and force prediction simulation of high weld pitch friction stir welding, Science and Technology of Welding and Joining 11(6) (2006) 657-665.

[20] Buchibabu, V., Reddy, G.M., De, A., Probing torque, traverse force and tool durability in friction stir welding of aluminum alloys, Journal of Materials Processing Technology 241 (2017) 86-92.

[21] Arora, K.S., Pandey, S., Schaper, M., Kumar, R., Effect of process parameters on friction stir welding of aluminum alloy 2219-T87, The International Journal of Advanced Manufacturing Technology 50(9) (2010) 941-952.

[22] Schick, D., Babu, S.S., Foster, D.R., Dapino, M., Short, M., Lippold, J.C., Transient thermal response in ultrasonic additive manufacturing of aluminum 3003, Rapid Prototyping Journal 17(5) (2011) 369-379.

[23] Rumble, J.R., CRC Handbook of Chemistry and Physics, 100 ed., CRC Press/Taylor & Francis, Boca Raton, FL, 2019.

[24] Mishra, R.S., De, P.S., Kumar, N., Friction Stir Welding and Processing: Science and Engineering, Springer International Publishing2014.

[25] Phillips, B.J., Avery, D.Z., Liu, T., Rodriguez, O.L., Mason, C.J.T., Jordon, J.B., Brewer, L.N., Allison, P.G., Microstructure-deformation relationship of additive friction stir-deposition Al–Mg–Si, Materialia 7 (2019) 100387.

[26] Arora, A., Nandan, R., Reynolds, A.P., DebRoy, T., Torque, power requirement and stir zone geometry in friction stir welding through modeling and experiments, Scripta Materialia 60(1) (2009) 13-16.

[27] Humphreys, F.J., Hatherly, M., Recrystallization and Related Annealing Phenomena, Elsevier Science2012.

[28] International, A., E112-13 Standard Test Methods for Determining Average Grain Size, ASTM International, West Conshohocken, PA, 2013.

[29] Summers, P.T., Chen, Y., Rippe, C.M., Allen, B., Mouritz, A.P., Case, S.W., Lattimer, B.Y., Overview of aluminum alloy mechanical properties during and after fires, Fire Science Reviews 4(1) (2015) 3.

Chapter 5

Investigation of the Stick-Slip Contact State during Additive Friction Stir Deposition for Cu and Al-Mg-Si

5.0. Abstract

Additive friction stir deposition (AFSD) is a metal additive manufacturing technology that uses frictional heating and deformation bonding to fabricate three-dimension components. As a friction stir process, the thermal and mechanical processing conditions are intrinsically coupled. The contact state at the tool-material interface is critical in determining the coupling of the thermomechanical processing history. AFSD provides a unique opportunity to directly monitor the contact state and quantify the stick-slip phenomenon at the material interface. This work investigates the sticking coefficient $(1 - \delta)$ at various AFSD equipment processing conditions using surface paint speckle tracking through optical video monitoring in Cu and Al-Mg-Si. For both material systems, increasing the tool rotation rate Ω decreases the sticking coefficient $(1 - \delta)$. A key difference in the two material systems is observed in how the layer height h affects the sticking coefficient. In Cu, increasing h increases $(1 - \delta)$, whereas in Al-Mg-Si increasing

h decreases (1 – δ). This difference is attributed to the dynamic friction coefficient which determines the dominant deformation mechanism during the AFSD process. A preliminary comparison of the forces during AFSD using two different tool geometries is also presented in this work.

5.1. Introduction

Additive friction stir deposition is a novel additive manufacturing technique that uses the fundamental physical principles from friction stir to enable frictional heating and continuous deformation to fabricate metal components [1]. In friction stir techniques, the heat generation and material deformation are intrinsically linked [2]. An increase in the frictional heat will affect the materials properties for deformation while an increase in the material deformation will contribute to heat generation through plastic energy dissipation. Critically, the contact state that the tool-material interface determines the transfer of deformation from the tool to the material underneath by the slipping coefficient δ and the sticking coefficient (1 – δ). While the stick-slip phenomena plays a critical role in understanding the thermomechanical history of the processed material, characterization of the contact state remains elusive, and modeling efforts attempting to quantify the contact state have yielded many conditions for δ. Colegrove and Shercliff (2004) used computational fluid dynamics (CFD) to estimate the contact state from the local shear stress at the interface [3]. Hamilton *et. al* (2008) applied an energy-based slip coefficient δ to estimate the peak temperatures during friction stir welding of aluminum alloys with high accuracy but did not consider heat generated from plastic deformation [4]. Wang *et. al* (2013) compared several slip contact state conditions for modeling of friction stir welding

of aluminum alloy 7449 [5]. They found that the most successful approach for temperature estimation used the contact shoulder radius ratio method that a fraction of the tool radius is under full sticking condition and the remainder of the tool is in a full slipping condition. From these studies it is evident that characterization of the contact state is essential in understanding the thermomechanical processing history during friction stir.

AFSD provides the unique opportunity to directly observe the contact state at the tool-material interface. Compared to other friction stir processes where direct observation of the stir zone is obscured by the tool, in AFSD the interface can be monitored from the leading edge, the advancing edge, or the retreating edge of the deposit. Here, a systematic variation of the equipment process variables is performed for Cu and Al-Mg-Si while monitoring the deposition zone with optical video. The aim is to observe the evolution of the contact state at different processing conditions and ascertain if it is possible to transition between different regimes of slipping coefficient δ. Direct observation of the stick-slip phenomena will provide insight onto the boundary conditions at the tool material interface. This quantification may prove invaluable in modelling of the heat generation mechanisms [6] and can lead to improved prediction of total heat input with experimental validation for FSW and AFSD [7]. Additionally, the characterization of the contact state will also improve the prediction capabilities of the strain and strain-rates during friction stir processes.

5.2. Experimental Procedure

5.2.1. Material Deposition

A MELD – R2 system (MELD Manufacturing Corporation, Christiansburg VA, USA) was used for all deposits in this work. The system was equipped with a flat surface 38 mm wide tool steel head with no surface features except for the feed-rod exit hole. Each experiment involved a single layer of deposition with ~70 mm of in-plane traverse. The key processing conditions of tool rotation rate, in-plane velocity, and layer height were systematically varied to observe the evolution of the contact state at different processing conditions. While the material feed rate is also an important processing parameter, the ratio between the material feed rate and the tool in-plane velocity has significant effects on the final part quality. As a result, it was kept constant at a value of 2:3 material feed rate to tool in-plane velocity which consistently produces high-quality deposits using the flat tool head geometry. Tool rotation rates were distributed across the viable processing range at 300, 400, 500, and 600 RPM, the selected in-plane tool velocities include 1.27 mm/s and 2.54 mm/s, and the layer height which is set by the spacing between the tool and substrate was set at 1 mm and 2 mm.

Two material systems were studied in this experiment: 1) Cu-110 (commercially pure) and 2) a commercially available Al-Mg-Si alloy (AA 6061). The feed-rod material was square rod with a side length of 9.5 mm. Substrates measured 152.4 x 203.2 x 6.35 mm. Three parallel tracks were deposited onto each substrate along the 152.4 mm direction with 50.8 mm spacing between the center of each track. 15 minutes of cooling with continuous air flow were allotted between deposition of each track to prevent any influence

of residual heat in the tool or substrate. The substrate and the deposited material had the same composition for each respective material system.

5.2.2. Material Flow Monitoring

A Dino-Lite Edge AM4115ZT Microscope was placed on the leading edge of the tool to record optical images of the deposit surface. The camera had a spatial resolution of 640 x 480 pixels at a working distance of 125 mm and a capture rate of 30 Hz. Black paint was speckled onto the leading edge of the deposit during processing in order to track the velocity of the material relative to the tool head. The stick-slip boundary condition can be characterized by this direct comparison of the speckle velocity and the tool head rotation velocity. Fig. 5.1 schematically shows how the experimental setup for the optical video recording was incorporated into the AFSD system.

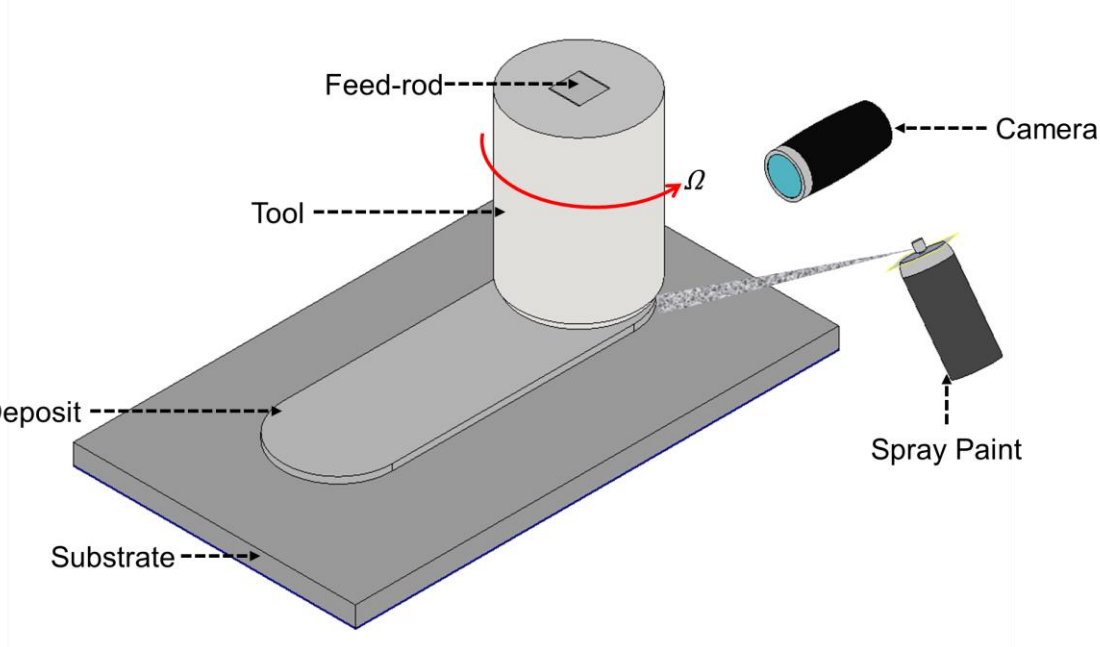

Figure 5.1. A schematic of the experimental set-up for optical monitoring of the contact state at the tool-material interface.

5.3. Results

5.3.1. Calculating the Sticking Fraction

Paint speckling on the surface of the deposit is used to track the rotation rate of the deposit relative to the velocity of the tool. Snapshots taken from the videos can be seen in Figure 5.2 (a) for Al-Mg-Si and (b) for Cu. The outer diameter of the deposit is used as the distance for the effective linear velocity of the tool rotation. The tool velocity at the specified radius is then calculated via $v_{tool}(r) = \Omega \cdot 2\pi r_{deposit}$ where v_{tool} is the linear velocity of the tool at the radius of the deposit, Ω is the tool rotation rate, and $r_{deposit}$ is the measured radius of the deposit. The distance traveled by the paint speckles serves as a linear projection for the fraction of the circumference rotated by the deposit. The number of frames divided by the framerate of the camera provides the time elapsed for the allotted travel of the paint speckles from which the deposit linear velocity $v_{deposit}$ can be calculated. The sticking coefficient (1 – δ) is then calculated by $(1 - \delta) = {}^{v_{deposit}}/_{v_{tool}}$.

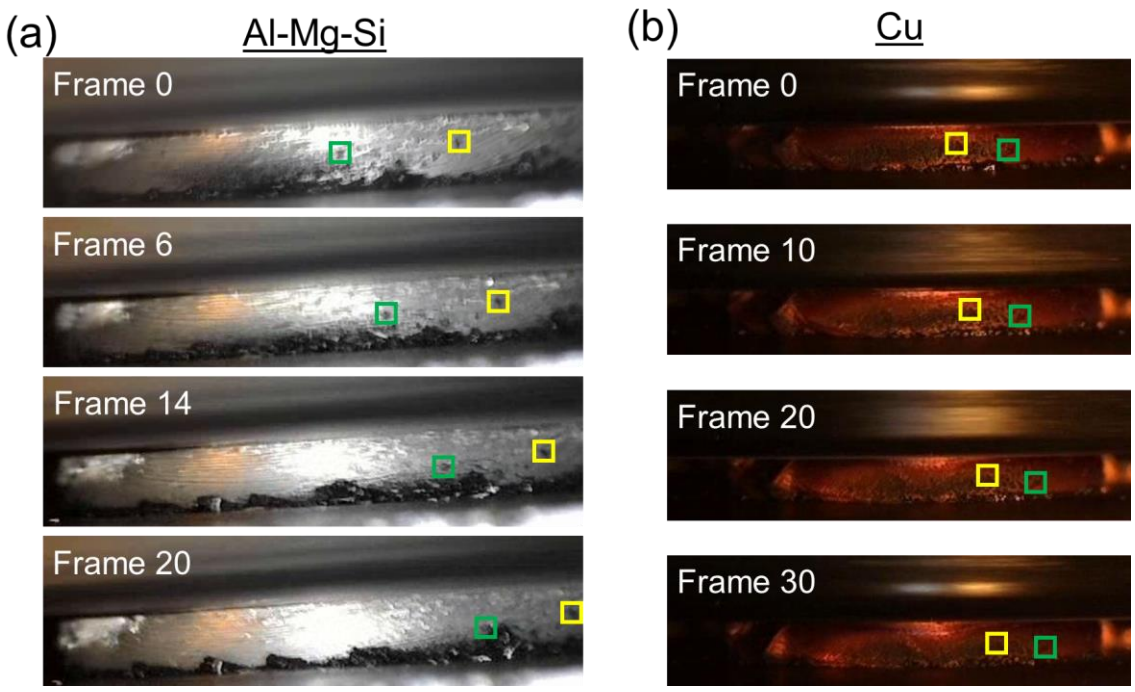

Figure 5.2. Snapshots taken from the optical video recording for (a) Al-Mg-Si and (b) Cu that show rotation of the material in the same direction as the tool motion.

5.3.2. Sticking Coefficient Trends in Al-Mg-Si

Fig 5.3. shows a preliminary investigation into how the contact state at the interface evolves at various equipment processing conditions including the tool rotation rate Ω and tool velocity V for Al-Mg-Si. All processing conditions for Al-Mg-Si are shown to be in a partial stick condition. From the figure, it is observed that a decrease of tool rotation rate Ω or an increase of the tool velocity V results in an increase of the sticking coefficient (1 – δ). The tool rotation rate has a negative correlation which matches the expected trends from literature. For any two materials with interface friction, there is a critical velocity $v_{critical}$ above which no sticking can occur [8]. As this critical velocity is approached, the sticking coefficient decreases. While the tool velocity may have been expected to follow a similar trend as Ω since it increases the local velocity of the tool, changing the tool velocity can

also lead to different mechanical constraints and velocity fields. At low *V*, the material can slowly expand radially due to the continuous feeding of new material, regardless of the tool velocity. Increasing *V*, leads to a direct shift in the magnitude of the velocity of the tool and deposit, but only in the longitudinal direction. This creates preferential motion along the longitudinal direction and limits material extrusion along the transverse direction. As a result, the radial position *r* for measurement may decrease and lead to a subsequent decrease in the velocity of the tool [7]. In turn, this can lead to a higher apparent sticking fraction.

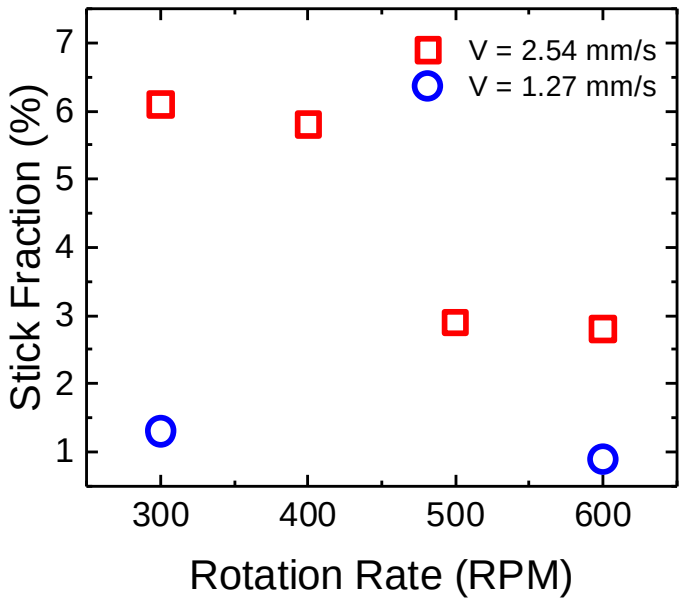

Figure 5.3. A plot showing the sticking coefficient (1 – δ) for Al-Mg-Si at several different tool rotation rates Ω and two different in-plane velocities *V*. In general, the sticking fraction is observed to decrease with increasing Ω or decreasing *V*.

5.3.3. Sticking Coefficient Cu

For Cu, only the effect of the tool rotation Ω rate was investigated as shown in Fig. 5.4. The general trend is similar to that in Al-Mg-Si. Higher linear velocities favor slipping over sticking, so an increase in the tool rotation rate Ω leads to a decrease in the sticking coefficient $(1 - \delta)$. For all of experiments in this work Cu shows a partial-stick condition which contrasts with previous measurements of the stick-slip ratio for AFSD of Cu systems.

Previous work showed a full slipping condition ($\delta = 1$) in the bulk of the deposition zone and a near full sticking condition near the feed-rod initial radius [9]. Note that the tool geometry in each set of experiments was substantially different in these sets of experiments. This work used a flat tool with no surface features while the previous work used a tool with two surface protrusions immediately surrounding the feed-rod exit hole. Given the additional surface area at a lower radial position, the propensity for sticking is higher in the area immediately surrounding the protrusions. This may result in a "shear layer" [10] type effect in the area immediately surrounding the pins. Instead of a gradual decrease in velocity with radius as is the case for the flat tool, the protrusions induce a larger area with high sticking fraction, but once the material is sufficiently far away from the protrusions, the radial velocity of the tool may be too fast to accommodate any sticking of material exiting the shear layer/transition zone. This may explain rapid transition to slipping in the case of the tool with protrusions.

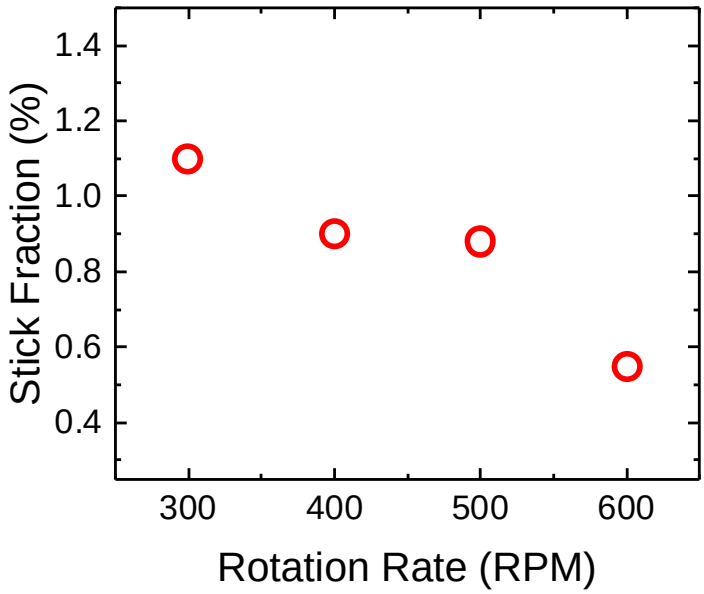

Figure 5.4. A plot showing the sticking coefficient (1 – δ) for Cu at several different tool rotation rates.

5.3.5. Layer Height Effects

Figs. 5.5 show the effect of the layer height on the sticking fraction for (a) Al-Mg-Si and (b) Cu. For Al-Mg-Si it is noted that increasing *h* leads to decreasing sticking coefficient (1 – δ). For Cu the opposite trend is observed where increasing *h* leads to increasing sticking coefficient (1 – δ). Increasing *h* directly increases the volume of free space beneath the tool, but since the volumetric feed rate is held constant the volume of material deposited remains constant. This has competing two effects on the tool-deposit interaction: 1) increasing the layer height for a constant volume of material will lead to a narrower track as material surges upward rather than outward and 2) the mechanical constraint applied by the tool is alleviated as the distance between the constraints of the substrate and the tool is increased.

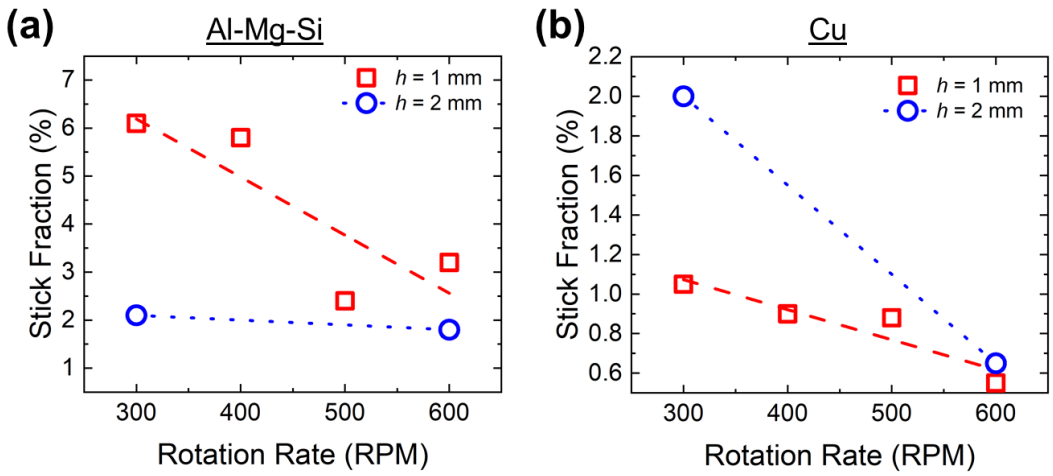

Figure 5.5. A plot of the stick fraction (1 – δ) for (a) Al-Mg-Si and (b) Cu at different layer heights.

The force evolution at different layer heights is also monitored for Al-Mg-Si and Cu as shown in Fig. 5.6. The normal stress F_z for Al-Mg-Si appears to slightly increase with increasing layer height h. Cu follows the opposite trend where increasing layer height h decreases the normal stress F_z. For the torque M_z both materials follow a similar trend where increasing layer height h leads to decreasing M_z. Furthermore, the torque variation at a layer height of 2 mm becomes near constant for different tool rotation rates Ω in the case of both material systems. This suggests that the reduced mechanical constraint imparted by the tool may have significant influences on the shear deformation experienced by the material.

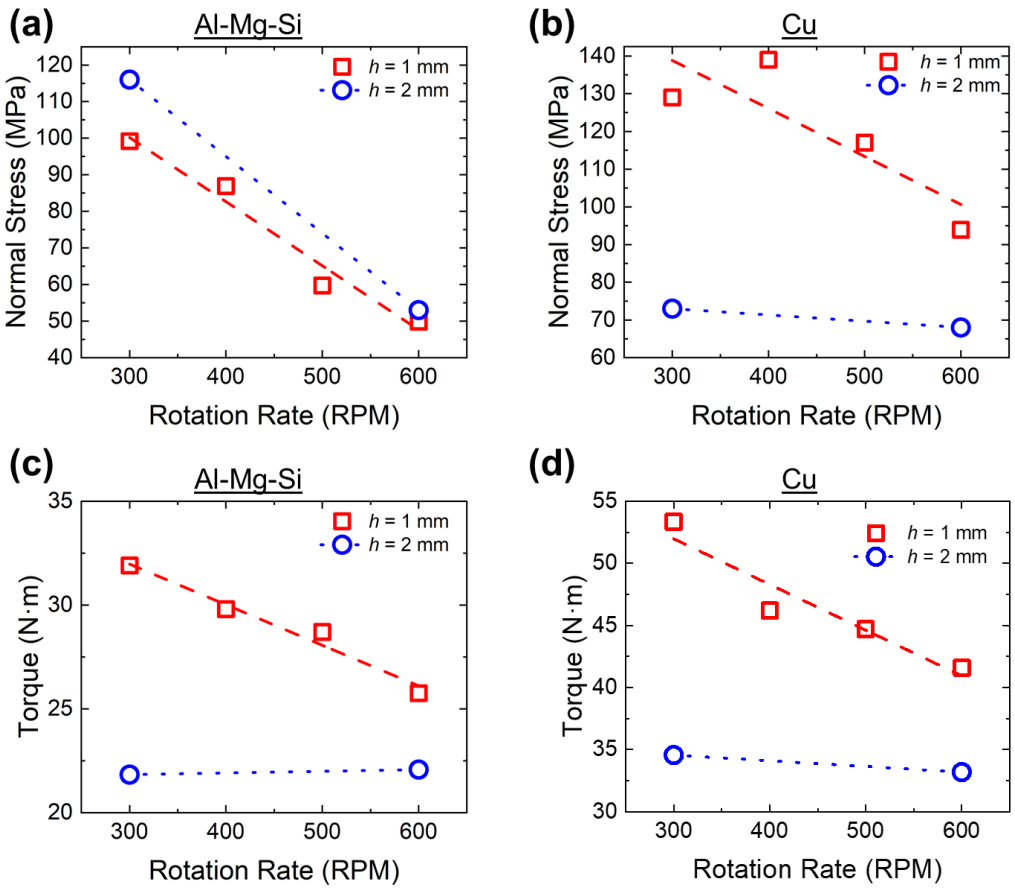

Figure 5.6. A plot of the (a) and (b) steady-state normal stress for Al-Mg-Si and Cu at different layer heights. (c) and (d) are plots of the steady-state torque for Al-Mg-Si and Cu at different layer heights.

5.4. Discussion

5.4.1. Comparison of Al-Mg-Si and Cu

While the trend for the sticking coefficient with respect to the rotation rate Ω is similar in both material systems, the magnitude of sticking is substantially lower in the case of Cu compared to Al-Mg-Si and sees a much smaller change (0.6% in Cu compared to ~5% in Al-Mg-Si). This corresponds with previous measurements where Cu appeared to be more dependent on the compressive force for deformation and Al-Mg-Si experienced significant shear imparted by the tool. The sticking coefficient and frequency is directly related to the dynamic friction coefficient. For Cu:Fe the dynamic friction coefficient is lower than that of Al:Fe which may contribute to the reduced sticking in the case of Cu [11, 12].

The force trends at different layer heights are also indictive of the contact state between the tool and material. For Al-Mg-Si, increasing layer height h leads to increasing normal force F_z and decreasing torque M_z. These trends may correspond to a transition from a shear dominated process to a process more dependent on the uniaxial compression for deformation. As the layer height is increased, the mechanical constraint out of plane is decreased thus the tool velocity F_z. The decrease in sticking coefficient $(1 - \delta)$ and the decrease in M_z suggest that the deformation imparted by the tool is reduced at increasing layer heights. This is likely a result of the reduced mechanical constraint imposed at greater layer heights. For Cu, the deformation was more compression dominated in all cases due to the relatively lower dynamic friction coefficient. Thus, increasing the layer height only serves to decrease the radial distance (and velocity) of the tool and increase the sticking fraction $(1 - \delta)$. These trends are shown in Fig. 5.7.

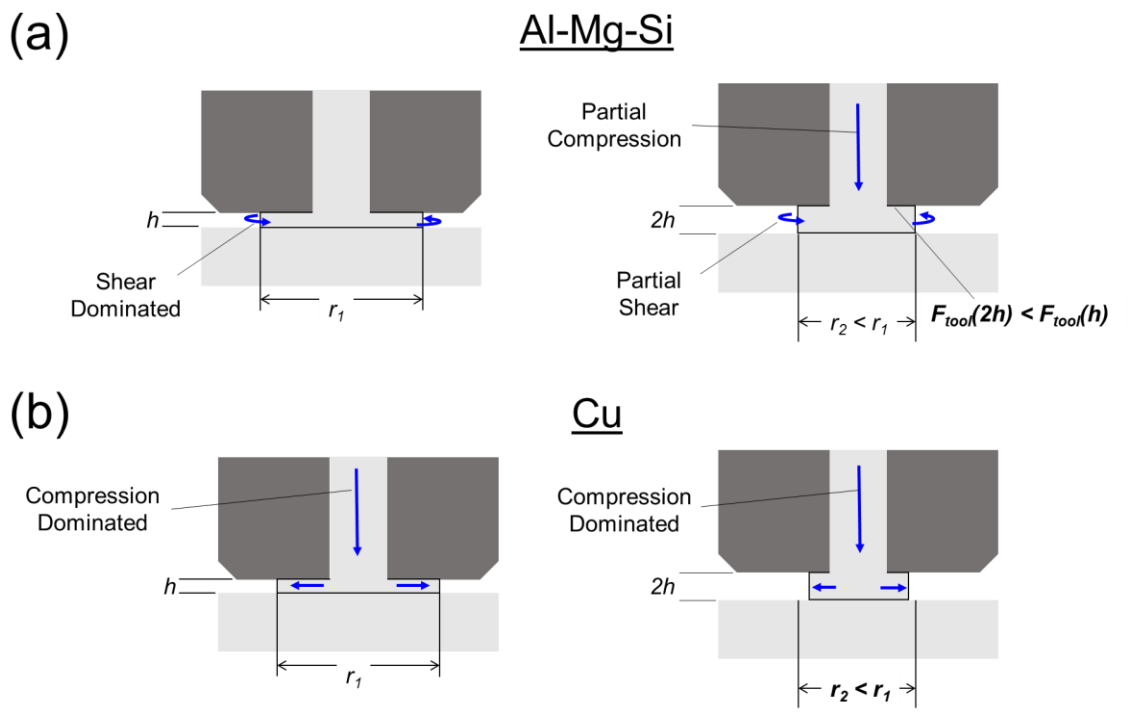

Figure 5.7. A schematic showing how the contact state changes with different layer heights for (a) Al-Mg-Si and (b) Cu. For Al-Mg-Si an increase of the layer height leads to a balance of the shear deformation and compression deformation. For Cu, the deformation is always compression dominated, so increasing the layer height only reduces the radius and local velocity of the tool so there is increased propensity for sticking.

5.4.1. Influence of Tool Geometry on Force and Torque in Cu and Al-Mg-Si

This section discusses the influence of tool geometry on the forces measured during deposition for a 1mm layer height deposit. Chapter 3.0 discussed how the normal stress followed an inverse trend with peak temperature for both Cu and Al-Mg-Si. Here, the pseudo heat index for temperature prediction is plotted along the normal stress for the two material systems (Fig. 5.8) using two different tool geometries. For Al-Mg-Si the normal stress F_z required for deformation is generally higher at low values of Ω^2/V for the flat tool compared to the tool with protrusions. Tool protrusions provide additional driving force for shear induced deformation and contribute additional heat generation via plastic

energy dissipation. In turn this leads to a baseline heat generation even at low values of Ω^2/V. For higher values of Ω^2/V the frictional heat at the interface is the only contributing factor, so the actual processing parameters are more influential thus there is an increased slope for the flat tool In Cu, a similar trend is observed, with a pseudo heat index of Ω/V. Since the deformation is more compression driven, the influence of the protrusions is small thus the trend is similar for the flat tool and protrusion tool.

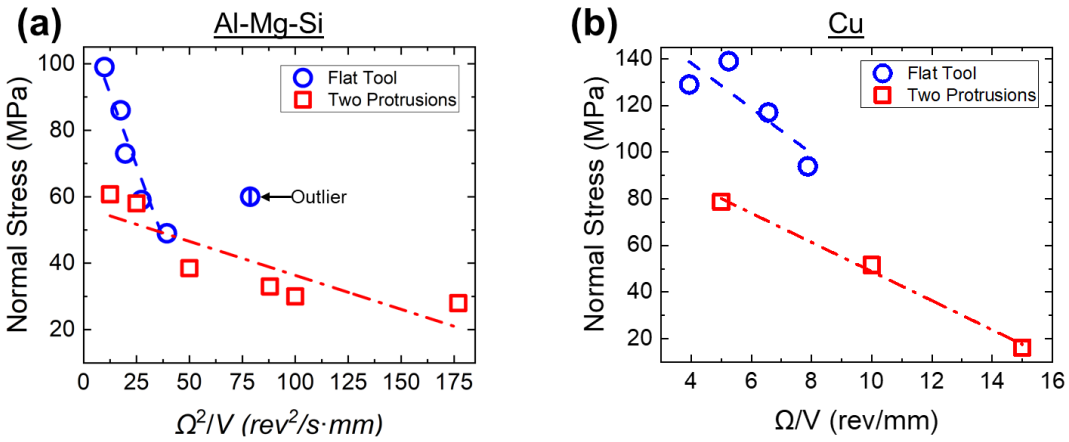

Figure 5.8. A plot of the steady state compressive stress with different tool geometries plotted (a) against a pseudo heat index of Ω^2/V for Al-Mg-Si and (b) against a pseudo heat index of Ω/V for Cu.

The torque at different processing conditions (Fig. 4.9) follows similar trends for the flat and two protrusion tools for Al-Mg-Si. Here the torque is dominated by the stick-slip interaction at the tool-material interface due to the comparably larger area of the tool compared to the protrusions. Although the trend is similar, the magnitude of the torque M_z is higher for the tool with two protrusions. The protrusions provide extra resistance to rotation, as they must mill through unheated substrate during tool in-plane motion and meet resistance when pushing mixing material within the processing zone. For Cu, the tool with protrusions shows no dependence of the torque on processing conditions as discussed in

Chapter 4. This is a result of the bulk of the deposit being in a full slipping condition. For the flat tool, there is a partial stick condition, so the dependence on the processing parameters becomes more evident. Higher values of the pseudo heat index Ω/V to reduced torque as the flow stress required to shear decreases.

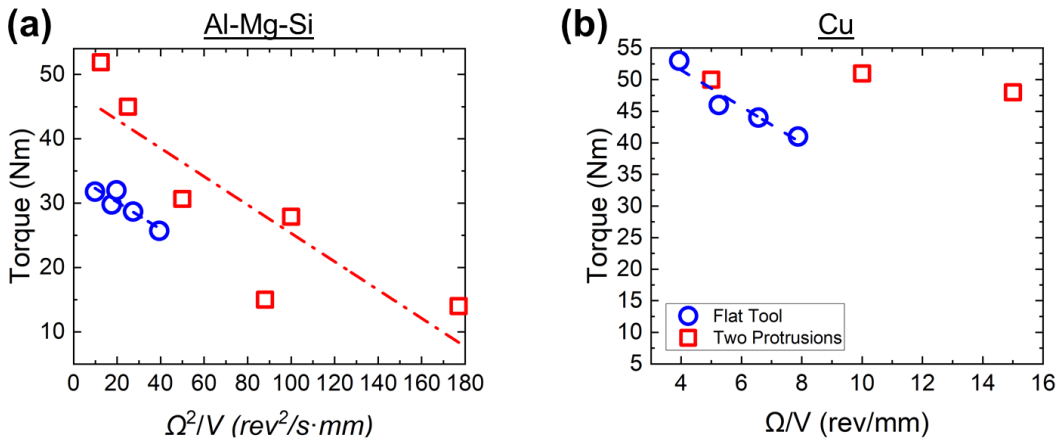

Figure 5.9. A plot of the steady state torque with different tool geometries plotted (a) against a pseudo heat index of Ω^2/V for Al-Mg-Si and (b) against a pseudo heat index of Ω/V for Cu.

5.5. Conclusions

This work investigated the contact state between the tool and material in the processing zone during AFSD of Cu and Al-Mg-Si at various equipment processing conditions. Optical video monitoring in combination with surface speckling of the deposition zone enabled direct quantification of sticking coefficient $(1 - \delta)$. A preliminary comparison of the forces during AFSD using two different tool geometries is also presented in this work. The most prominent conclusions are bulleted below:

- For AFSD of Cu and Al-Mg-Si using a flat tool, both materials exhibit a partial stick condition at the tool-material interface. The magnitude of sticking in Cu is substantially lower than that observed in Al-Mg-Si and this is attributed to the lower dynamic friction coefficient between Cu:Fe compared to Al:Fe.
- Increasing Ω decreases the sticking coefficient $(1 - \delta)$ for both Cu and Al-Mg-Si. This is a result of the increased tool velocity at a comparable normal force. For Al-Mg-Si an increase of V increases the sticking coefficient.
- For Cu increasing layer height h increases the sticking coefficient. Increasing h with a constant volume of material leads to a reduced radius for the outer surface of the deposit. The decreased velocity of the tool at this reduced radius increases the chances of sticking.
- For Al-Mg-Si, increasing h decreases the sticking coefficient. For Al-Mg-Si, there is a higher dynamic friction coefficient with the tool, thus higher propensity for sticking. Increasing h leads to a decrease in the mechanical constraint and a subsequent decrease in the normal force applied by the tool.

- For Al-Mg-Si, the normal stress F_z for a flat tool is much more dependent on the processing parameters than in the case for a tool with two protrusions. The two protrusions introduce additional heat generation via plastic deformation which provides additional softening at low values of Ω^2/V. For the torque M_z, The tool protrusions introduce additional surface area and resistance to rotation, so the torque for a tool with surface features is higher than the flat tool.
- For Cu, the normal stress F_z for a flat tool is generally higher than for a tool with surface features. The tool protrusions provide a shearing effect that reduces the compressive stress required to yield material. The torque for a flat tool follows a temperature dependent trend where higher values of Ω/V lead to decreased M_z. For the tool with protrusions, the torque is constant at all processing conditions, since the bulk of the processing zone is in a full-slipping condition.

References

[1] Yu, H.Z., Jones, M.E., Brady, G.W., Griffiths, R.J., Garcia, D., Rauch, H.A., Cox, C.D., Hardwick, N., Non-beam-based metal additive manufacturing enabled by additive friction stir deposition, Scripta Materialia 153 (2018) 122-130.

[2] Mishra, R.S., De, P.S., Kumar, N., Friction Stir Welding and Processing: Science and Engineering, Springer International Publishing2014.

[3] Colegrove, P.A., Shercliff, H.R., Two-dimensional CFD modelling of flow round profiled FSW tooling, Science and Technology of Welding and Joining 9(6) (2004) 483-492.

[4] Hamilton, C., Dymek, S., Sommers, A., A thermal model of friction stir welding in aluminum alloys, International Journal of Machine Tools and Manufacture 48(10) (2008) 1120-1130.

[5] Wang, H., Colegrove, P.A., dos Santos, J.F., Numerical investigation of the tool contact condition during friction stir welding of aerospace aluminium alloy, Computational Materials Science 71 (2013) 101-108.

[6] Schmidt, H., Hattel, J., Modelling heat flow around tool probe in friction stir welding, Science and Technology of Welding and Joining 10(2) (2005) 176-186.

[7] Nandan, R., Roy, G.G., Lienert, T.J., Debroy, T., Three-dimensional heat and material flow during friction stir welding of mild steel, Acta Materialia 55(3) (2007) 883-895.

[8] Banerjee, A.K., Influence of kinetic friction on the critical velocity of stick-slip motion, Wear 12(2) (1968) 107-116.

[9] Garcia, D., Hartley, W.D., Rauch, H.A., Griffiths, R.J., Wang, R., Kong, Z.J., Zhu, Y., Yu, H.Z., In situ investigation into temperature evolution and heat generation during

additive friction stir deposition: A comparative study of Cu and Al-Mg-Si, Additive Manufacturing 34 (2020) 101386.

[10] Mendez, P.F., Tello, K.E., Lienert, T.J., Scaling of coupled heat transfer and plastic deformation around the pin in friction stir welding, Acta Materialia 58(18) (2010) 6012-6026.

[11] Nuruzzaman, D.M., Chowdhury, M.A., Friction Coefficient and Wear Rate of Copper and Aluminum Sliding against Mild Steel International Transaction Journal of Engineering, Management, & Applied Sciences & Technologies 4(1) (2012) 29-40.

[12] Rumble, J.R., CRC Handbook of Chemistry and Physics, 100 ed., CRC Press/Taylor & Francis, Boca Raton, FL, 2019.

Chapter 6

Conclusions and Future Work

6.1. Conclusions

This work characterized the thermomechanical processing history of the Additive Friction Stir Deposition (AFSD) process through *in situ* measurement of the thermal history, the applied forces, and the tool-material contact state for two material systems, Cu-110 and AA-6061. The intrinsic coupling of these thermomechanical conditions was explored in depth and quantitative relationships were established for several of these trends. The coupling of the applied forces and heat generation mechanisms were found to be critically dependent on the tool contact state described by the sticking coefficient $(1 - \delta)$. The evolution of this contact state at various processing conditions and with different tool geometries was also investigated and showed that Cu can transition from full slipping condition ($\delta = 1$) to a partial sticking condition with different tool geometries. These trends may serve to improve future modeling efforts of friction stir welding and AFSD and lead to improved quality control of friction stir manufactured parts. The most notable conclusions from each chapter are detailed below:

Thermal History Monitoring

Quantitative trends for the peak temperature with respect to the processing conditions were established, however different forms of the relationship were obtained for each material system: T_{Peak} exhibits a power law relationship with Ω/V in Cu but with Ω^2/V in Al-Mg-Si. This is attributed to the contact state during processing of each material system. During AFSD of Cu, material rotation only occurs in the area immediately surrounding the rotating feed-rod. The interface between the tool head and deposited material in the bulk of the processing zone is under a full slipping condition, and interfacial friction is the dominant heat generation mechanism in the deposition zone. During AFSD of Al-Mg-Si, the tool rotation causes the material in the deposition zone to rotate. The interfacial contact is under a partial slipping/sticking condition. Both interfacial friction and volumetric energy dissipation contribute to the heat generation in the deposition zone.

Force Evolution Monitoring

The normal force in AFSD has an initial peak during the frictional heating and macroscopic shape change of the feed-rod compared to the peak observed in FSW which corresponds to the tool plunge phase. For both material systems, F_z increases with increasing V and decreases with increasing Ω. For Cu, the contribution associated with each variable is comparable in magnitude whereas for Al-Mg-Si the Ω has significantly higher contribution than V. The torque M_z for Al-Mg-Si increases with increasing V and decreases with increasing Ω. For Cu, the torque is effectively constant. This is again related to the contact state at the tool-material interface whereby the Cu is in a full slipping condition and the torque equation simplifies to two constants: the dynamic friction coefficient μ_f and the normal force applied by the tool F_T. Finally, microstructure characterization of Al-Mg-Si provided estimates of the flow stress during processing which is found to be strongly correlated to the torque.

Contact State Monitoring and Tool Geometry Effects

For AFSD of Cu and Al-Mg-Si, both materials exhibit a partial stick condition at the tool-material interface when using a flat, featureless tool. The magnitude of sticking coefficient $(1 - \delta)$ in Al-Mg-Si is higher compared to the sticking coefficient in Cu at all processing conditions. This is related to the lower dynamic friction coefficient between Cu:Fe compared to Al:Fe which is an indicator of the sticking frequency. The two material systems exhibit different trends in contact state for increasing layer height h: For Cu increasing layer height h increases the sticking coefficient, whereas for Al-Mg-Si increasing h decreases $(1 - \delta)$. Increasing h with a constant volume of material leads to a reduced radius for the outer surface of the deposit. The decreased velocity of the tool at this reduced radius increases the chances of sticking in Cu. For Al-Mg-Si Increasing h leads to a decrease in the mechanical constraint and a subsequent decrease in the normal force applied by the tool. In general, the sensitivity of the normal stress F_z to the processing conditions Ω and V increases for a flat tool. The torque trends remain largely similar for Al-Mg-Si. For Cu, the key difference in torque is a result of the partial sticking condition for the flat tool and the full slipping condition for the tool with protrusions.

6.2. Future Work

While this work establishes a baseline for understanding of the thermomechanical processing history during AFSD, there are still opportunities to apply this work towards improved manufacturing and answering additional unexplored questions.

6.2.1 Process Monitoring

This work established several methods for monitoring the thermal and thermomechanical processing history during the additive friction stir deposition process, however there were many limitations due to equipment, time, and cost that prevented exploration of some fundamental questions. These limitations primarily relate to the measurement of local scale gradients and forces. The temperature measurements and thermal characteristics in this work were analyzed in the context of the bulk part. Peak temperatures, heating rates, cooling rates, exposure times, and cooling mechanism were generally characterized and approximate ranges where established, however there was no in-depth investigation into the local variation of these thermal history characteristics within the processing zone. The heat generation and contact state are expected to change with respect to the position along the tool radius [1]. This is expected to produce thermal gradients, and local scale variations of the strain and strain rates experienced by the material during processing [2]. Furthermore, direct measurement of the normal force at the tool-material interface is of particular interest for process modeling and determining the evolution of the contact state [3].

6.2.2 Process modeling

This work established many generic trends for heat generation, macroscopic force evolution, and the tool-material contact state however, it is by no means a comprehensive study that is universally applicable to all processing conditions and materials. This experimental work can serve as a foundation for process modeling and provide substantial data for validation of such models. Conversely, process modeling can serve to supplement the experimental data collected in this work and extend the applicability to different processing parameters and material systems. This is of particular interest when trying to optimize the properties of as-manufactured components [4]. Furthermore, local-scale modeling may provide additional insights into the local scale thermal and deformation gradients that were not investigated in this work.

6.2.3 Towards closed-loop control

Beyond the scope of understanding the process-structure-property relationship lies the application of this knowledge for the the control of the processing history and the design of the structure and properties. The information collected in this work can serve as a starting point for the local control of the processing history to produce homogeneous parts at the bulk scale or intended variations in microstructure to meet anisotropic performance metrics. This could be accomplished by local control of the forces and contact state, to vary the strain and strain rates during processing and enable microstructure control. Furthermore, control of the peak temperatures, cooling rates, and heating rates is of particular interest for multi-phase material systems or precipitate strengthened material systems [5]. Additionally, integration of the online sensing techniques used in this work with an advanced image processing and data analytics algorithm can enable detection of processing anomalies and automatically vary the equipment

processing parameters to prevent defect formations [6]. This type of advancement in the AFSD technology is necessary to see the salient advantages of additive manufacturing come to fruition.

References

[1] Nandan, R., Roy, G.G., Lienert, T.J., Debroy, T., Three-dimensional heat and material flow during friction stir welding of mild steel, Acta Materialia 55(3) (2007) 883-895.

[2] Schmidt, H., Hattel, J., A local model for the thermomechanical conditions in friction stir welding, Modelling and Simulation in Materials Science and Engineering 13 (2004) 77-93.

[3] Liechty, B.C., Webb, B.W., Modeling the frictional boundary condition in friction stir welding, International Journal of Machine Tools and Manufacture 48(12) (2008) 1474-1485.

[4] Rajamanickam, N., Balusamy, V., Madhusudhanna Reddy, G., Natarajan, K., Effect of process parameters on thermal history and mechanical properties of friction stir welds, Materials & Design 30(7) (2009) 2726-2731.

[5] Sato, Y.S., Urata, M., Kokawa, H., Friction-Stir Welding of Precipitation-Hardenable Aluminum Alloy 6063, METALLURGICAL AND MATERIALS TRANSACTIONS A 33A (2002) 625.

[6] Rao, P.K., Liu, J., Roberson, D., Kong, Z.J., Williams, C., Online Real-Time Quality Monitoring in Additive Manufacturing Processes Using Heterogeneous Sensors, Journal of Manufacturing Science and Engineering 137(6) (2015).